Development of ion-conducting ceramics for reversible Solid Oxide Cells

Natasha Di Benedetto Sviridenko

Graduate Program in Chemistry
Facultad de Química
Universidad de la República

Programa de Desarrollo de las Ciencias Básicas

Montevideo – Uruguay
October 2022

Development of ion-conducting ceramics for reversible Solid Oxide Cells

Natasha Di Benedetto Sviridenko

Master's Thesis submitted to the Graduate Program in Chemistry, Facultad de Química of the Universidad de la República, as part of the requirements for obtaining the title of Master in Chemistry.

Director:
Dr. Leopoldo Suescun

Co-advisor:
Prof. Dr. Konrad Świerczek

Academic director:
Dr. Leopoldo Suescun

Montevideo – Uruguay
October 2022

MEMBERS OF THE THESIS DEFENSE COMMITTEE

_____

Dra. Elen Almeida

_____

Dra. María Fernanda Cerdá

_____

Dr. Ricardo González

Montevideo – Uruguay

October 2022

To the parents who nurtured us.

To the teachers who inspired us.

Acknowledgements

Los casi dos años (y una pandemia) de trabajo, resumidos en esta tesis, no hubieran sido posibles sin el apoyo de diferentes personas e instituciones que acompañaron en los momentos felices y suavizaron los no tanto.

En primer lugar, a mis tutores, Leopoldo y Konrad, por creer en mi desde el principio, y orientarme y apoyarme durante estos años intensos. En especial a Leo, por dedicarse completa y desinteresadamente en mi formación, tanto profesional como personal, y por contagiarme todo su amor y pasión por la Cristalografía, las perovskitas y las celdas de combustible, que fue lo que me trajo hasta acá.

Gracias a mis compañeros del Cryssmat-Lab, Joaco, Guz, Julio y Noelia, por tantos momentos compartidos y estar siempre ahí para mi cuando lo necesité, dentro y fuera del trabajo. Gracias a Joaquín, por ser el mejor compañero de trabajo (aunque a veces también el único) y guiarme y apoyarme durante este proceso. Gracias a Caro, ex-profesora, colega y casi-mamá, por confiar en mi, por iluminarme cuando estaba más perdida, tanto en cuestiones académicas como personales.

Me gustaría agradecer también el apoyo financiero recibido por parte de la Comisión Académica de Posgrado y PEDECIBA Química para la realización de esta maestría.

Por otro lado, quiero darle las gracias a Albert, Marc, y todos mis compañeros de IREC, por hacer estos meses de pasantía realmente memorables, por apoyarme y hacerme sentir parte desde el día uno. Y por todo lo que vendrá.

Gracias a mis amigos, los de siempre y los que, aunque recientes, parecen de toda la vida. Cami, Andre, Anto, Flo, Mica, Pao, Sofi y Xime, gracias por bancarse meses de ausencia social, escuchar interminables quejas e intentar entender 'lo de los cristales', aunque… a quién queremos engañar? Ni yo sé a veces que es eso. A mis amigas de la facu, Clau, Vale, Agus y Vale B., por interminables tardes de estudio e inolvidables momentos juntas, por apoyarme, guiarme y bancarme la cabeza. A Dolo y Jhoan, por estar cerca a pesar de estar lejos. Gracias de verdad.

Por último, agradezco especialmente a mi familia. Porque estuvo y siempre va a estar ahí para mi. A la Titi y a Bibi. A Massi, mi hermano y primer amigo. Y en especial a mamá y papá, por apoyarme incodicionalmente en cada una de las etapas de mi vida. Gracias. Nada de esto sería posible sin ustedes, y *yo* no sería quien soy de no ser por ustedes.

Simplemente gracias.

Crystals are like people, it is the defects in them which tend to make them interesting.

Colin Humphreys

Abstract

The development of new alternative energy sources has become an imperative task due to the excessive consumption of fossil fuel reserves and the serious consequences that global warming has and keeps causing, which is now recognised as a fact. Uruguay has not fallen behind in the subject, responding to global efforts with the implementation of a Policy that revolutionised the country's energy matrix through the use of traditional renewable energy sources and the search for other not-conventional technologies.

Hydrogen emerged then as the energy source of the future, and with it, new energy generation and storage technologies. In this light, Solid Oxide Cells (SOC), both as fuel cells and their reverse mode, electrolyser cells, have generated a lot of interest in recent decades owing to their high efficiency and flexibility. One of the great challenges these devices exhibit is the development of brand-new materials that allow operation temperatures to be between 600-800 °C, for which it is essential to find electrodes that have high electrocatalytic activity and that do not suffer degradation in the operating conditions.

The present thesis is dedicated to designing, synthesising and characterising new micro and nanostructured ceramic materials for their use as oxygen electrodes in reversible solid oxide devices. For this purpose, an auto-combustion synthetic route was proposed for the obtention of composites that could enhance the electrochemical performance of traditional electrodes, and these materials, combined with state-of-the-art electrolyte and fuel electrode, were used in the assembly of a complete solid oxide cell.

Keywords: hydrogen, fuel cell, SOFC, SOEC, reversible solid oxide cells, electrochemistry

Resumen

El consumo excesivo de las reservas de combustible fósil y las graves consecuencias que el calentamiento global ha causado y sigue causando han hecho que el desarrollo de nuevas fuentes de energía alternativas se haya vuelto una tarea imperativa. Uruguay no se ha quedado atrás, implementando nuevas Políticas estatales que revolucionaron la matriz energética nacional a través del uso de fuentes de energía renovables tradicionales y la búsqueda de otras modernas.

El surgimiento del hidrógeno como fuente de energía del futuro, ha provocado la necesidad de nuevas tecnologías de generación y almacenamiento del mismo (y otros combustibles en general). Las Celdas de Óxido Sólido, funcionando tanto en modo celda de combustible como en modo electrolizador (operación reversa), han atraído mucho interés en las últimas décadas gracias a su alta eficiencia y flexibilidad. Uno de los grandes desafíos que presentan estos dispositivos, es el desarrollo de nuevos materiales que permitan bajar la temperatura de funcionamiento hasta el rango de 600-800 ºC, lo que implica la búsqueda de electrodos que presenten alta actividad electrocatalítica pero no se degraden en las condiciones de operación.

La presente tesis se encuentra dedicada al diseño, preparación y caracterización de nuevos materiales cerámicos micro y nanoestructurados para su uso como electrodo de oxígeno en celdas de óxido sólido reversibles. Para esto, se propuso el uso del método de auto-combustión de gel para la obtención de compositos que pudieran exhibir mejor performance electroquímica que los electrodos tradicionales, y luego, junto al uso de electrolitos y electrodos de combustible convencionales, el armado de una celda de óxido sólido completa.

La metodología aplicada permitió la obtención, caracterización y testeo de tres materiales (un cerámico ya reportado y dos compositos del mismo con CeO_2) con potencial aplicación como electrodos de oxígeno en celdas de óxido sólido reversibles. Los mismos exhibieron valores de potencia similares a los reportados en literatura al testearse en celdas completas usando YSZ como

electrolito y Ni-YSZ como electrodo de combustible. Estas medidas representan los primeros resultados de caracterización de dispositivos de óxido sólido reversibles obtenidos por el grupo.

Palabras claves: hidrógeno, celdas de combustible, SOFC, SOEC, celdas de óxido sólido reversibles, electroquímica

Table of Contents

Acronyms and abbreviations

AC	Alternating Current
ASR	Area Specific Resistance
BL	Barrier Layer
BSE	Backscattered Electron
CPE	Constant Phase Element
EC	Equivalent Circuit
EDTA	Ethylenediaminetetraacetic acid
EDX	Energy Dispersive X-ray
EIS	Electrochemical Impedance Spectroscopy
GDC	Gadolinia Doped Ceria, $Ce_{0.9}Gd_{0.1}O_{1.95}$
HER	Hydrogen Evolution Reaction
HOR	Hydrogen Oxidation Reaction
I-V	Galvanostatic polarisation current-voltage curve
IT	Intermediate Temperature
LSCF	$La_{0.6}Sr_{0.4}Co_{0.2}Fe_{0.8}O_{3-\delta}$
LSFCu	$La_{0.6}Sr_{0.4}Cu_{0.2}Fe_{0.8}O_{3-\delta}$
MIEC	Mixed Ionic-Electronic Conductor
OCV	Open Circuit Voltage
OER	Oxygen Evolution Reaction
ORR	Oxygen Reduction Reaction
Q_{rev}	Reversible heat
PB	Phase Boundary
PLD	Pulsed Layer Deposition
PVA	Poly Vinyl Alcohol
PVP	Poly Vinyl Pyrrolidone
RL	Roughness Layer
R_s	Serial resistance (ohmic resistance)
R_{pol}	Polarisation resistance

SE	Secondary Electron
SEM	Scanning Electron Microscopy
SOC	Solid Oxide Cell
SOEC	Solid Oxide Electrolyser Cell
SOFC	Solid Oxide Fuel Cell
TEC	Thermal Expansion Coefficient
TPB	Triple Phase Boundary
V_{TN}	Thermoneutral Voltage
W_{rev}	Reversible work
XRD	X-Ray Diffraction
YSZ	Yttria-Stabilised Zirconia, $Zr_{0.84}Y_{0.16}O_{1.92}$

Chapter 1

-INTRODUCTION-

1. INTRODUCTION

1.1.Alternative energies and hydrogen

The growing concern around global warming and other environmental problems linked to the indiscriminate consumption of fossil fuels makes it extremely necessary to find new alternative means of generating and storing energy that does not produce waste products. [1–7]

In the last few years, and thanks to the creation of a short, medium, and long-term Energy Policy (2005-2030), the Uruguayan energy matrix has undergone major transformations in search of a path towards environmental sustainability. Uruguay has opted for a greater presence of renewable energy sources, and efficient and rational use of them. This has not only allowed the country to meet its increasing energy demand (even managing to export the surplus of energy to neighbouring countries) but also, to go hand in hand with the efforts that have been set in motion worldwide to reduce CO_2 emissions and mitigate climate change.

The main actions carried out in this first stage to pursue this end, involved the promotion of renewable energy sources such as hydroelectric, wind, biomass and photovoltaic (solar). At present, Uruguay has practically achieved the decarbonisation of electricity generation (97 % of renewables in the 2017-2020 period: 44 % hydroelectric, 32 % wind, 18 % biomass and 3 % solar). [8,9]

Figure 1.1 shows the energy production proceeding from renewable sources (by source) for the whole World in the last 50 years (**a**) and for Uruguay in the 2017-2020 period (**b**).

a)

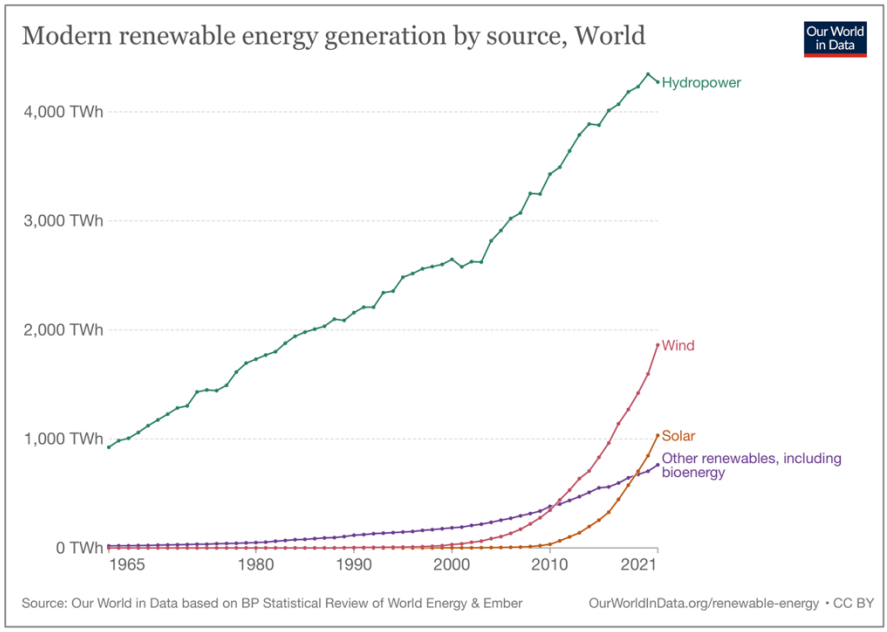

b)

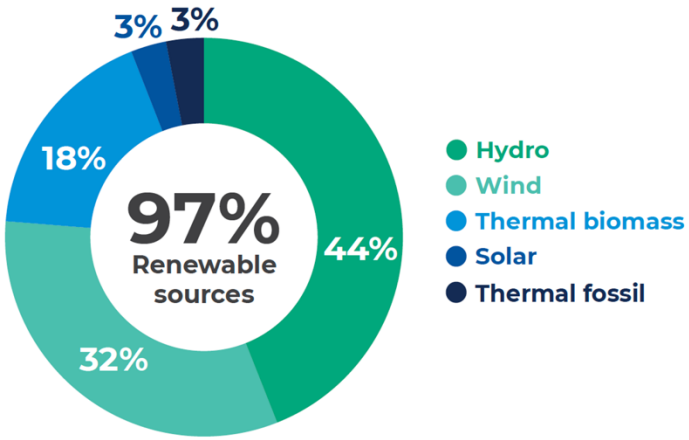

Figure 1.1. Renewable energy production at the worldwide level (**a**) and for Uruguay (**b**). Extracted from [9–11]

Although the advantages of implementing these renewable energies are many, it presents some drawbacks too, such as being naturally intermittent and not manageable (energy must be consumed when it is generated or otherwise is lost). This means that the supply and demand of the moment do not always match, reducing the reliability and security of the energy supply system. To manage this intermittency, the challenge relies on the development

of other non-traditional alternative energy sources and high-capacity energy storage devices. [8,12–14]

Despite that, Uruguay is very well positioned in the use of these energies and ready to take the next step in the energy transition path using hydrogen technologies, as the Belgian biochemist and CEO of Hydrogenics, Filip Smeets, stated in late 2018 [15]. This second stage includes the decarbonisation of the industrial and transport sectors, the development of a hydrogen economy, and the ability to maintain the previously-achieved advances. [9]

Hydrogen gas and especially green hydrogen (obtained from water electrolysis using renewable energy sources), emerges then as one of the most promising energy carriers for both small and large-scale energy applications (industry, transport, drones and other small appliances, heating, etc.). Its high abundance (although not available as pure H_2), versatility, high energy storage capacity (requiring special conditions, though) and the cleanest energy source known (does not produce CO_2 or other polluting gases) make it a good candidate for a wide variety of applications. Some of the hydrogen's uses in different sectors both as a source of energy or raw material are shown in Figure 1.2. [1,3,9,16–19]

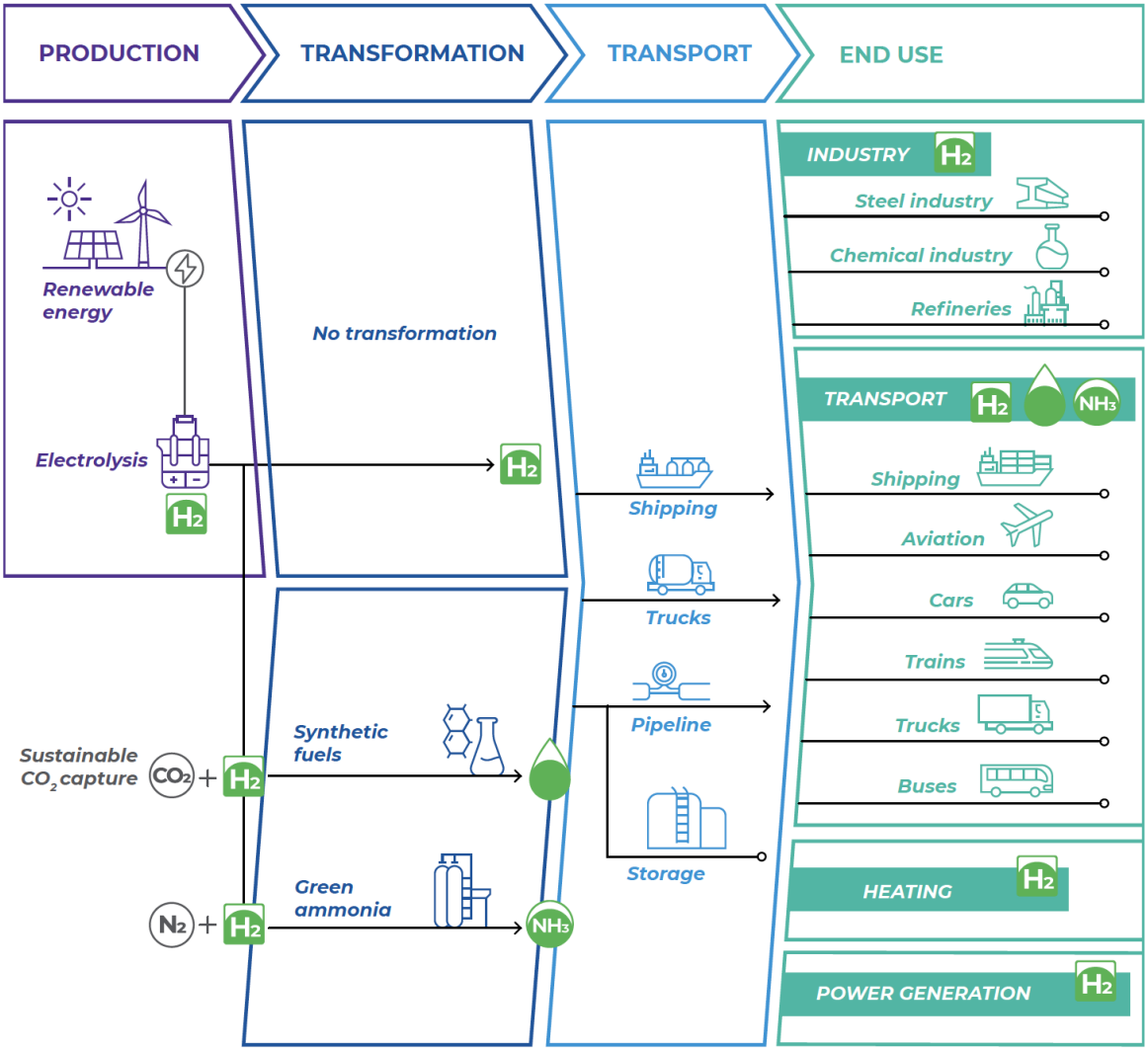

Figure 1.2. Diagram of the role of hydrogen in different sectors. Extracted from [9].

In this light, hydrogen itself, its transportation and the development of all its related regulations and norms have become a hot topic both for academia and the industrial sector. Being a key energy carrier connecting major renewable energies, hydrogen is crucial to move forward towards an environmentally sustainable society and this has not gone unnoticed. The greatest opportunity for a global reach of hydrogen-based technologies lies in fuel cell devices, especially Solid Oxide Fuel Cells (SOFCs) and the reversely operated Solid Oxide

Electrolyser Cells (SOECs), or altogether, Solid Oxide Cells (SOCs) [16,18]. Figure 1.3 shows a diagram of the role of hydrogen in the current energy scenario and how it relates to these energy devices.

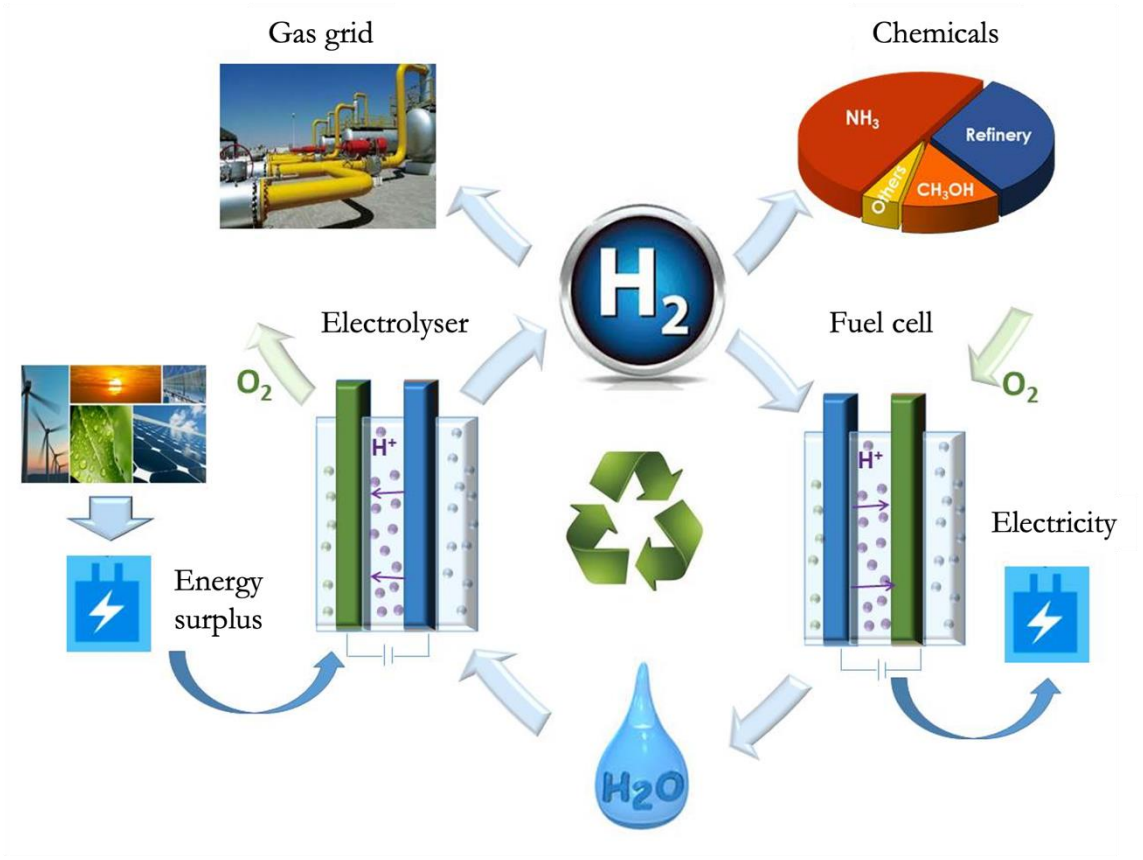

Figure 1.3. Diagram of the role and importance of hydrogen in the present and near-future energy applications. Extracted from [20].

1.2.Solid Oxide Cells (SOCs)

SOCs are intrinsically reversible electrochemical devices (rSOC), that unlike most types of electrochemical cells, use a solid electrolyte. Depending on the polarity of the reversible cell, they can operate as Solid Oxide Fuel Cells (SOFCs), oxidising combustible species to

generate electricity; or as Solid Oxide Electrolyser Cells (SOEC), consuming electrical energy to reduce water molecules and thereby obtain hydrogen gas; as shown in Figure 1.4. Therefore, when the electrical demand is high the rSOC can be used in SOFC mode to produce electricity and when there is a surplus of electrical generation, it can work in SOEC mode producing hydrogen gas (storing energy in the form of chemical bonds for later use). [21–23]

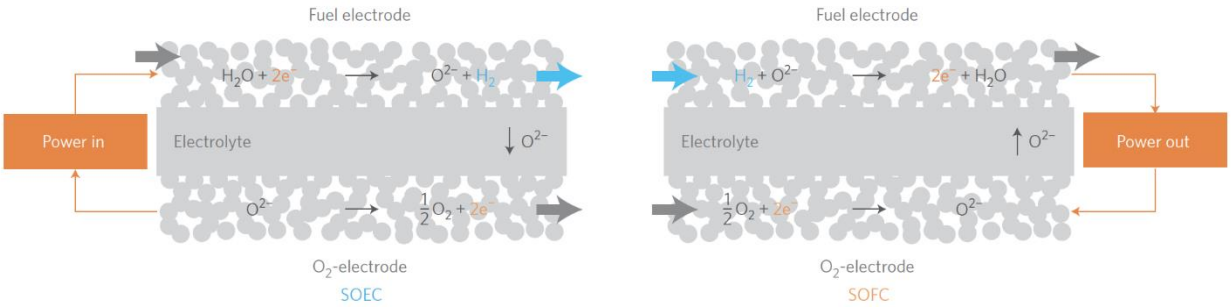

Figure 1.4. Diagram of the operation principles and reactions of the SOC devices in both SOEC mode (**left**) and SOFC mode (**right**). Extracted from [24].

The fact that the same unit can be used both to generate energy and to produce fuels, the flexibility to use different fuels (in SOFC mode), the possibility of being integrated with other renewable energy sources and its high theoretical energy efficiency (~60% in SOFC mode and ~80% in SOEC mode not including co-generation processes), in addition to operating quietly and being friendly to the environment, are some of the advantages of implementing this kind of systems. [12,16,21]

One of the main goals of the development of future SOCs is to decrease the operating temperature of the cell, at least, to an intermediate temperature range (600-800°C). Higher temperatures imply a rapid deterioration of the materials and a worsening in their transport properties and catalytic activity, which translates into a loss of efficiency, higher material

costs and a shorter lifetime, among others. Moreover, lower temperatures would allow the use of steel-based elements for cell-stack construction, which is very beneficial since it avoids the use of special and costly alloys like Crofer22APU and Inconel [25–27]. The design of new materials that meet all the aforementioned requirements and dodge the problems that may arise when they are put into operation, has become a fundamental task in the investigation of these technologies. [6,16,21,28–31]

1.2.1. SOC operation principles

SOC devices consist of two porous electrodes (fuel or hydrogen electrode and air or oxygen electrode) separated by a solid electrolyte. When operating in SOFC mode, hydrogen and oxygen gas react electrochemically to produce water gas. The fact that these two semi-reactions are spatially isolated, forces the electrons transferred from the fuel to flow through an external circuit before completing the reaction, doing useful work. The crucial task of (electronic) spatial isolation is accomplished by the use of a dense electrolyte.

The reactions that take place in each electrode, when fuelled by hydrogen and using an oxide ion conducting electrolyte, are the following:

Fuel electrode: $$H_{2_{(g)}} + O^{2-}(electrolyte) \rightarrow H_2O_{(g)} + 2e^- \quad (1.1)$$

Oxygen electrode: $$\frac{1}{2}O_{2_{(g)}} + 2e^- \rightarrow O^{2-}(electrolyte) \quad (1.2)$$

Total reaction: $$H_{2_{(g)}} + \frac{1}{2}O_{2_{(g)}} \rightarrow H_2O_{(g)} \quad (1.3)$$

Equations 1.1 and 1.2 are known as Hydrogen Oxidation Reaction (HOR) and Oxygen Reduction Reaction (ORR), respectively. [32,33]

SOEC mode is essentially generated by an inversion of the components and the reactions hereby occurring, which are portrayed below:

Fuel electrode: $$H_2O_{(g)} + 2e^- \rightarrow H_{2_{(g)}} + O^{2-}(electrolyte) \quad (1.4)$$

Oxygen electrode: $$O^{2-}(electrolyte) \rightarrow \frac{1}{2}O_{2_{(g)}} + 2e^- \quad (1.5)$$

Total reaction: $$H_2O_{(g)} \rightarrow H_{2_{(g)}} + \frac{1}{2}O_{2_{(g)}} \quad (1.6)$$

The equations 1.4 and 1.5 are known as Hydrogen Evolution Reaction (HER) and Oxygen Evolution Reaction (OER), respectively. The reversibility between these reactions and the ones presented for SOFC mode hint at the possibility of using the same unit as a rSOC.

Every electrochemical reaction presented carries an energy variation that can be described using the Laws of Thermodynamics. The maximum electric work that can be obtained from an operating SOFC can be calculated using Gibbs free energy equation for the reaction in 1.3 (isothermal process). Some assumptions need to be made to apply it: the reactants' total enthalpy $\sum_1^n n_i H_i$ is transformed entirely in the enthalpy of the products that abandon the system $\sum_1^n n_j H_j$, doing a reversible work w_{rev} and exchanging a certain quantity of reversible heat Q_{rev} with the environment, and there is no entropy change (e.g. mixing or de-mixing of reactants gases, otherwise it would not be reversible).

The reaction shown in 1.3 is spontaneous and thermodynamically favourable because the energy of the products is lower than that of the reactants. This change can be defined in the following equation:

$$\Delta G = \Delta H - T\Delta S = -nFE_{rev} \quad (1.7)$$

where ΔH is the enthalpy change, T is the temperature, ΔS is the change of entropy, n is the total number of exchanged electrons, E_{rev} is the reversible potential and F is Faraday's constant.

On the contrary, reaction 1.6 is endothermic and in consequence, the Gibbs free energy change of the process in a SOEC is positive, making it necessary to supply electrical energy and heat to ensure the operation of the cell. The thermodynamic parameters ΔG, ΔH and ΔS are a function of the operation temperature and are presented in Figure 1.5 for the reaction occurring in a SOEC. [32,34]

The reversible potential of an electrochemical cell varies as a function of species concentration, gas pressure and temperature, and can be determined employing the Nernst equation (shown here for eq. 1.3, the ideal gas assumption was used):

$$E = E^0 - \frac{RT}{nF} ln \frac{p_{H_2O}}{p_{H_2} \cdot p_{O_2}^{1/2}} \quad (1.8)$$

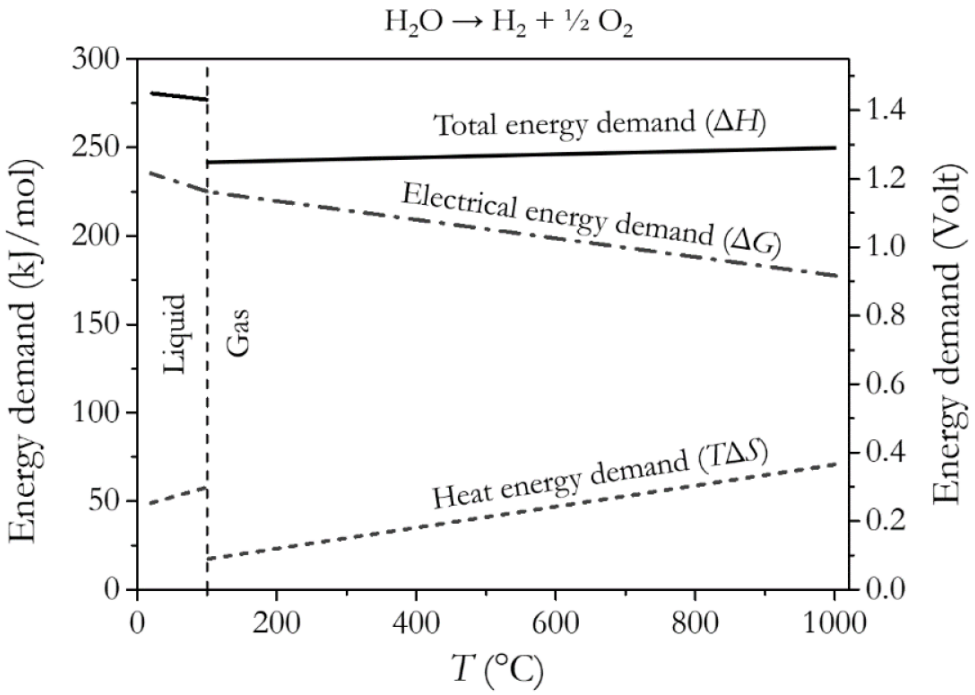

Figure 1.5. Reversible thermodynamics for H_2O electrolysis at atmospheric pressure. If the reaction at the top of the figure is reversed, and 'demand' is changed for 'supply' (or 'content'), then the same figure describes the thermodynamics for the pure H_2 fuel cell. The right Y-axis expresses the energy as the voltage needed to operate. Extracted from [23,35].

As depicted in Figure 1.5, the total energy demand of a SOEC increases with the increase in temperature despite the decrease in the electrical energy demand, where the ΔH energy demand can be compensated by means of heat. At certain operation conditions, the heat released from the reactions compensates for the thermal energy requirements on the so-called Thermoneutral voltage ($V_{TN} = \Delta H/nF$). Therefore, the SOEC can operate under endothermic conditions when $V_{operation}<V_{TN}$ or exothermic conditions when $V_{operation}>V_{TN}$.

From this perspective, we could be tempted to think that lower operation temperatures are more advantageous for these devices. Nonetheless, SOC internal resistance decreases with increasing temperatures due to an enhancement of the kinetic processes that result in

higher ionic conductivity and lower polarisation losses, and higher conversion rates stemming from the fact that the reactions occurring in the electrodes are thermally activated.

1.2.1. SOC electrochemical characterisation techniques

1.2.1.1.Electrochemical Impedance Spectroscopy (EIS)

Impedance spectroscopy is a powerful technique used in the characterisation of electrochemical systems. At an interface, the physical properties of a certain material change enormously and the charge distribution becomes heterogeneous (polarisation), diminishing the overall electrical conductivity of the cell. Each interface will polarise in its unique way when the system is subjected to an applied voltage.

This causes a shift in the focus of electrochemical measurements toward frequency-related phenomena, a feature that is taken advantage of in EIS. Here, a small electromagnetic perturbation reveals both relaxation times and relaxation amplitudes of the different processes occurring in a dynamic system over a wide range of frequencies, allowing the separation of them in the space of time/frequency.

This small perturbation enables the study of processes happening at different rates and with several simultaneous steps, as such a thing would be impossible to detect in a steady-state polarisation curve. For this purpose, a sinusoidal electrical current (or voltage) of small amplitude is applied and the consequent sinusoidal voltage (or current) response is measured (Figure 1.6). The ratio between these complex variables is known as impedance and can be calculated as follows:

$$\tilde{Z}(\omega) = \frac{\Delta V}{\Delta I} = \frac{|V|}{|I|}\frac{e^{i\omega t}}{e^{i(\omega t+\phi)}} = |Z|e^{-i\phi} \qquad (1.9)$$

where ΔV is the applied periodic potential perturbation, ω is the angular velocity, and ϕ is the phase shift generated in the current response. [33,36–38]

The use of this expression demands a linear dependence between the current and the voltage, this is why small perturbations are used. EIS measurements are usually performed in a defined frequency range and the values are registered in terms of Z' and Z'', which are the real and imaginary parts of the impedance, respectively:

$$Z(j\omega) = Z' + iZ'' \qquad (1.10)$$

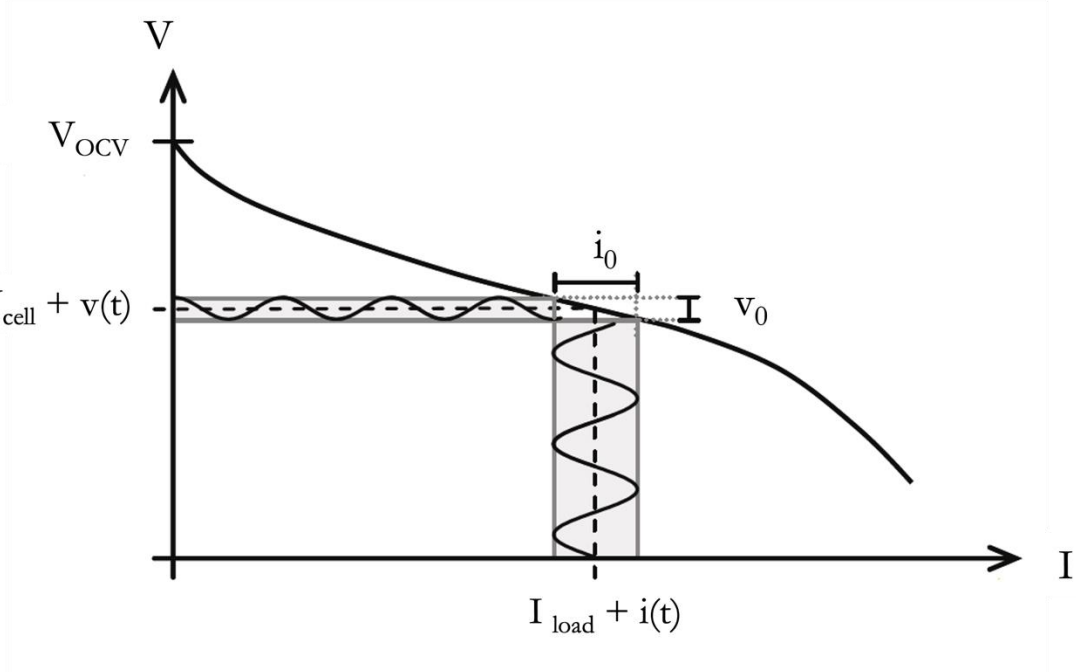

Figure 1.6. I-V curve exhibiting the perturbation used for EIS measurements in the form of a sinusoidal current of small amplitude i(t) which is superposed to a defined bias current I_{load}, and the measured voltage response u(t). Modified from [38].

These magnitudes are plotted in the complex plane in what is commonly known as a Nyquist plot. Another frequent representation is the Bode plot, where the phase shift (ϕ) versus frequency is depicted. Both types of diagrams are shown in Figure 1.7a.

Figure 1.7b shows an example of the Nyquist plot of a real SOFC single cell. In this graph, different processes are represented by different arcs (often superimposed). The high-frequency intercept ($\omega \to \infty$) with the x-axis is called serial resistance (R_0 or R_s) and corresponds to the pure ohmic resistance of the cell, while the low-frequency intercept is the differential resistance ($\omega \to 0$). The difference between these two magnitudes is called polarisation resistance (R_{pol}) and can be obtained as the sum of the polarisation resistance of each process that is taking place in the electrodes. Note that an individual arc does not always correspond to an individual process. [33,36–39]

The Equivalent Circuit model (EC model) is extensively used to evaluate the impedance data. This method consists in fitting the spectra obtained with electric circuit elements (typical and more complex ones) combined in series or parallel configurations, where each element represents an electrochemical process occurring at a characteristic frequency (and time). Nevertheless, one must keep in mind that identical impedance spectra can be fitted with different equivalent circuits and that do not necessarily possess a physical explanation. Therefore, the best fit will always be the one made with the simplest EC model where the elements and connections correlate with the physical and chemical processes taking place in the electrode during operation.

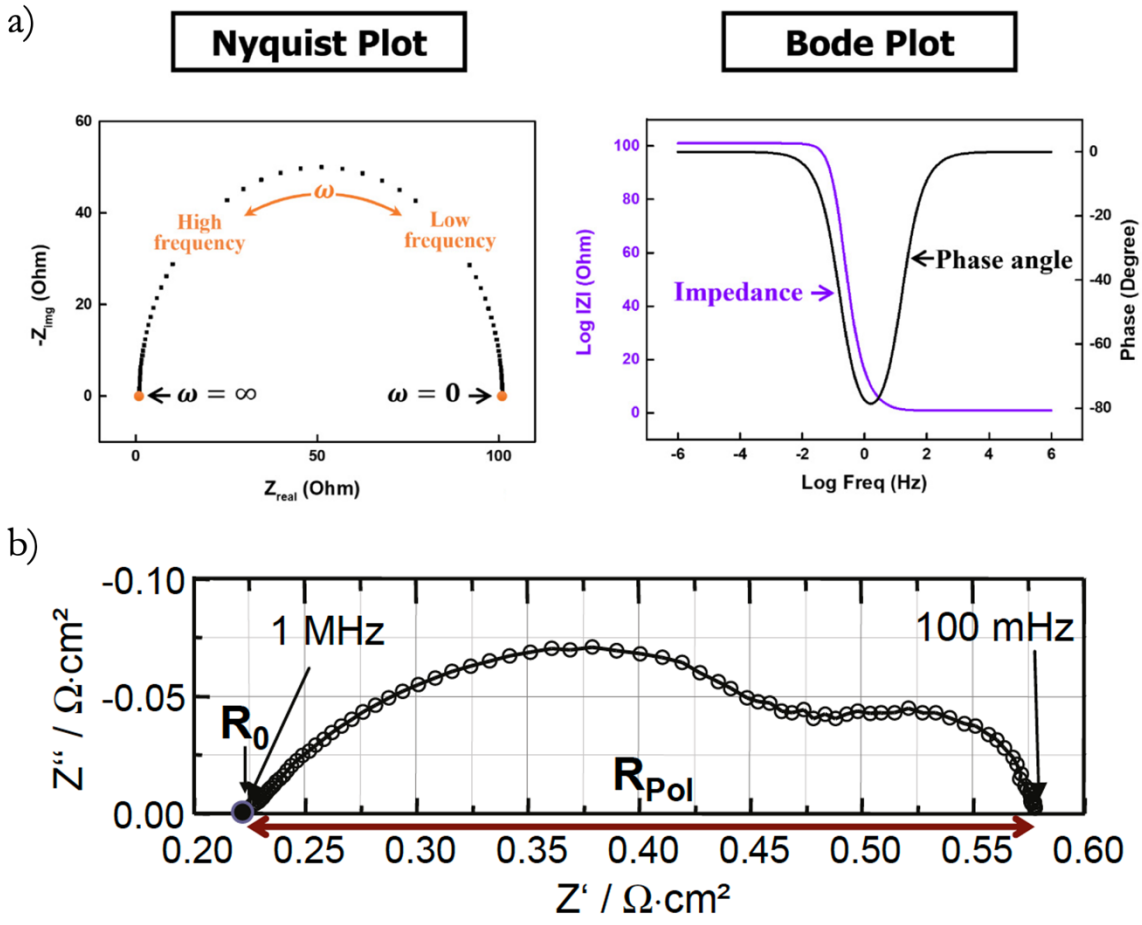

Figure 1.7. Nyquist and Bode representations of the electrochemical impedance spectra (a) and typical Nyquist plot obtained for a SOFC full cell (b). Extracted from [39] and [33].

Furthermore, real and dynamic systems like fuel cells and electrolysers are not ideal steady-state systems, hence the need for more complex circuit elements -like Constant Phase Elements (CPE or Q)- that take into account the distribution of relaxation times. This element is used to describe a non-ideal capacitance and includes an *n* value (obtained from the fitting) related to the depression of the semicircle, which varies between 0 (pure ohmic resistance) and 1 (pure capacitance).

1.2.1.2.Polarisation curves (I-V curves)

In operation conditions, the cell voltage drops with respect to the theoretical thermodynamic voltage (Nernst voltage) due to several irreversible internal loss mechanisms. The overall performance and the effect of different loss mechanisms of the cell are monitored through polarisation or I-V curves. These plots represent the variation of the potential (V) versus the supplied current density (j, A/cm^2) or current intensity (I, A). Figure 1.8 shows the typical I-V curve obtained when operating in SOFC mode.

These measurements can be carried out in both galvanostatic and potentiostatic modes. The former employs a potentiostat to control the current difference between the two electrodes and measure the resultant voltage, while the latter uses the potentiostat to control the voltage flowing between them and register the resulting current.

The Open Circuit Voltage (OCV or E_{eq}) of a cell is measured by applying a negligible current intensity between the electrodes and measuring the voltage generated between them, its theoretical value is determined by the Nernst equation for the corresponding reaction (equations 1.3 and 1.8 shown above) and is affected by the pO_2 difference at both sides of the cell. Therefore, the comparison of the theoretical and experimental OCV values indicates the quality of the sealing used to isolate the two electrodes of the cell.

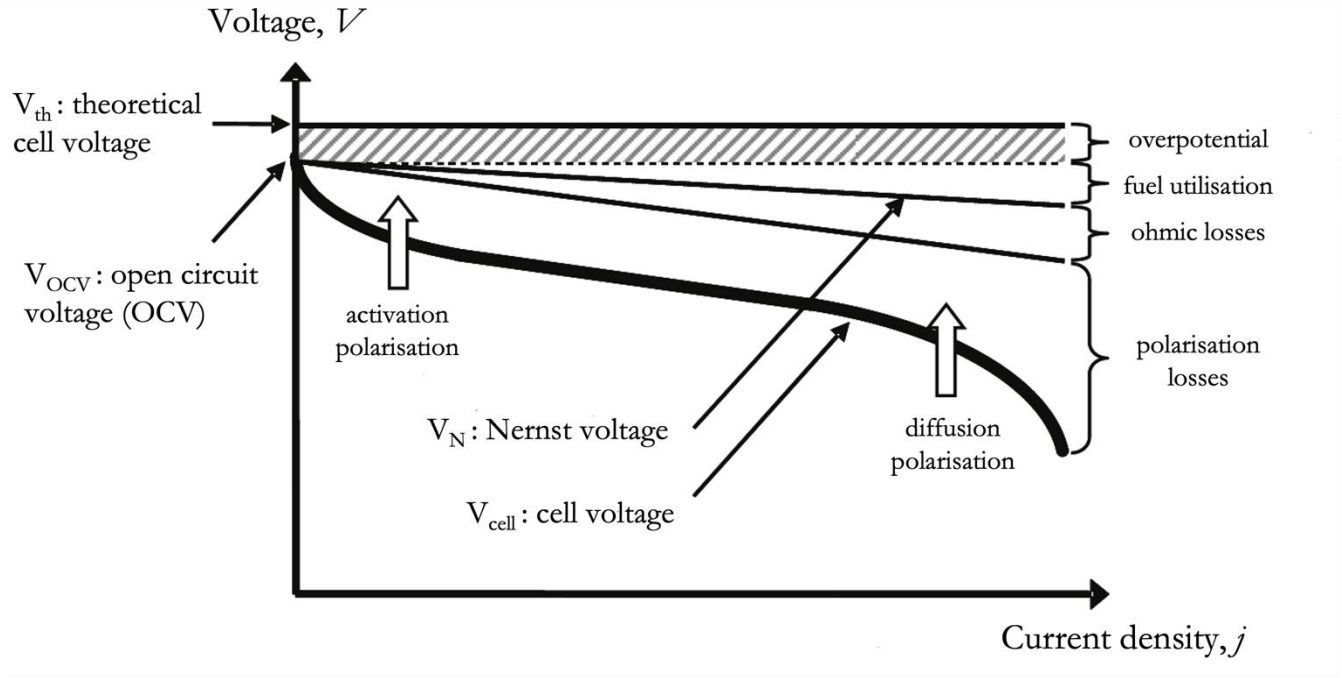

Figure 1.8. Diagram of a typical I-V curve of a SOFC showing the different polarisation types. Modified from [33].

When the cell operates in SOFC mode, the voltage decreases with the applied current density (with respect to the OCV value) due to the presence of different overpotentials that dominate the resistance of the cell (activation, ohmic and diffusion overpotentials). Lower overpotentials will derive in better cell performances. Conversely, in SOEC mode the applied current causes an increase in the voltage that needs to be supplied to the cell. [33,34,37,40]

The actual voltage output of a fuel cell can be expressed as:

$$V_{out} = E_{eq} - IR - \eta_c - \eta_a \qquad (1.11)$$

where IR represents the ohmic losses, η_c the cathodic losses (associated with factors that affect the ORR) and η_a the anodic ones (related to both the material's microstructure and diffusion processes). In the case of a SOEC, the overpotentials are added -instead of subtracted- to the Nernst potential to obtain the output voltage due to a change in the current direction.

Another typical representation used for SOFCs is the Power density versus current density curve (Figure 1.9), where the power delivered by the cell is given by the product of current and voltage at each point of the I-V curve. The current supplied by a fuel cell is directly proportional to the amount of fuel used (each mole of fuel provides n moles of electrons). As the fuel cell voltage decreases, the electric power produced also diminishes. In consequence, the cell voltage and therefore the electric power produced can be seen as a measure of the cell's efficiency. The determination of the operation conditions of the cell is commonly defined by this curve, and it is usual to select a current density equal to or below the power maximum (voltage efficiency improves but power density drops). At current densities larger than the power maximum, both the voltage efficiency and the power density fall. The important thing is to find a good efficiency, always before the power peak, with the highest fuel utilisation.

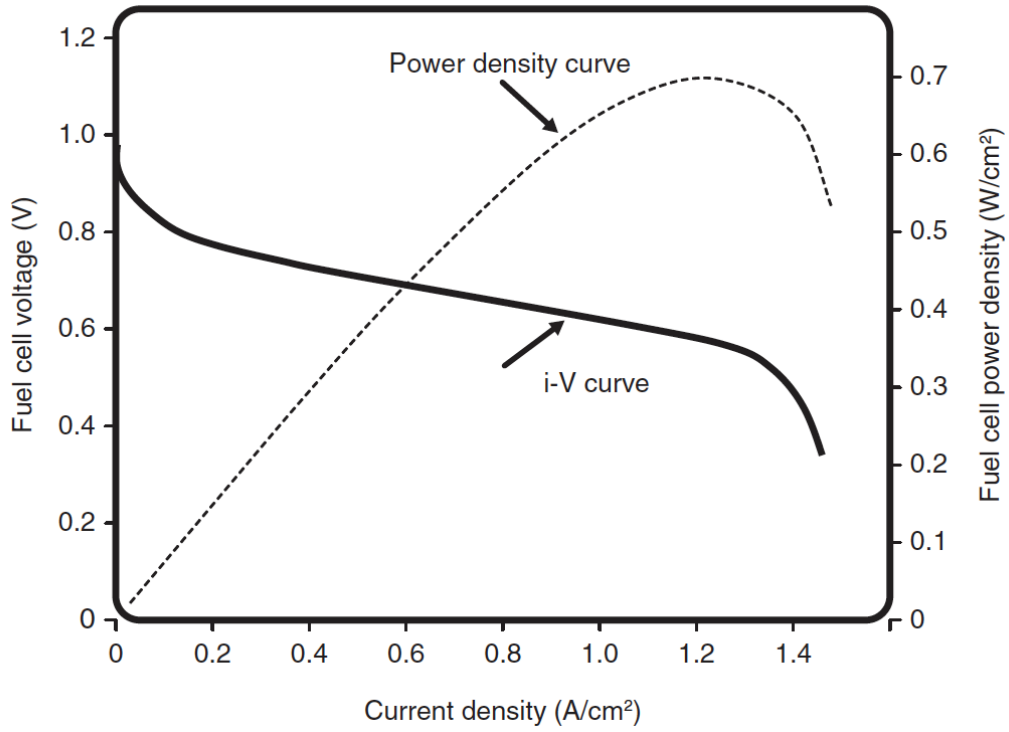

Figure 1.9. Representation of the typical I-V curve of a SOFC and the Power density curve obtained from it. Extracted from [32].

1.2.2. Materials for SOC

In the last 30 years, progressive and significant advances in the field of solid oxide cells have been reported. They entailed a lot of work by dedicated researchers from diverse areas of expertise. A comprehensive list of the materials classified according to their application (electrolytes, fuel electrodes and oxygen electrodes) is shown in Figure 1.10. Even though this list was extracted from a review published in 2005, it is still relevant and summarises the different groups of materials that have been tested for the different components of SOCs. New materials can be added to the same families, as will be discussed below.

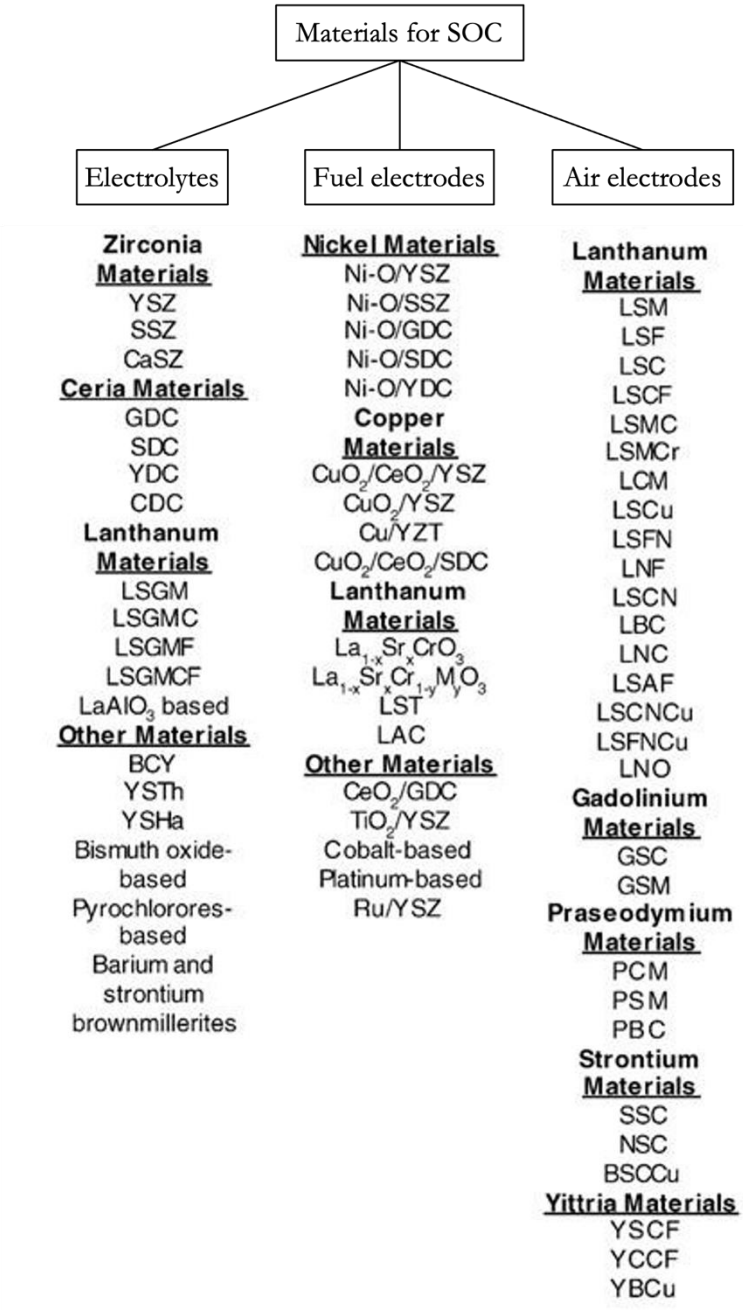

Figure 1.10. Diagram presenting the most common materials used in SOC applications. Modified from [41].

The acronyms for the majority of the materials shown in Figure 1.10 are explained in Figure 1.11 (the fuel electrodes are usually composed of NiO and an electrolyte, therefore, the acronyms are not repeated).

Acronym	Representative chemical formulas
Lanthanum cathodes	
LSM	$La_xSr_{(1-x)}MnO_3$ ($x \sim 0.8$)
LSF	$La_xSr_{(1-x)}FeO_3$ ($x \sim 0.8$)
LSC	$La_xSr_{(1-x)}CoO_3$ ($x \sim 0.6$–0.8)
LSCF	$La_{(1-x)}Sr_xFe_yCo_{(1-y)}O_3$ ($x \sim 0.4$, $y \sim 0.2$)
LSMC	$La_xSr_{(1-x)}Mn_yCo_{(1-y)}O_3$ ($x \sim 0.8$)
LSMCr	$(La_xSr_{1-x})_{.91}Mn_yCr_{(1-y)}O_3$ ($x \sim 0.7$, $y \sim 0.95$)
LCM	$La_xCa_{(1-x)}MnO_3$ ($x \sim 0.5$)
LSCu	$La_{(1-x)}Sr_xCuO_{2.5}$ ($x \sim 0.2$)
LSFN	$La_xSr_{(1-x)}Fe_yNi_{(1-y)}O_3$ ($x = 0.8$, $y = 0.8$)
LNF	$LaNi_{(1-x)}Fe_xO_3$ ($x \sim 0.4$)
LSCN	$La_xSr_{(1-x)}Co_yNi_{(1-y)}O_3$ ($x \sim 0.6$, $y \sim 0.98$)
LBC	$La_xBa_{(1-x)}CoO_3$ ($x \sim 0.4$)
LNC	$LaNi_{(1-x)}Co_xO_3$ ($x \sim 0.4$)
LSAF	$La_xSr_{(1-x)}Al_yFe_{(1-y)}O_3$ ($x \sim 0.8$, $y \sim 0.2$)
LSCNCu	$La_xSr_{(1-x)}Co_yNi_{(1-y-z)}Cu_zO_3$ ($x \sim 0.8$, $y \sim 0.8$, $z \sim 0.05$)
LSFNCu	$La_xSr_{(1-x)}Fe_yNi_{(1-y-z)}Cu_zO_3$ ($x \sim 0.8$, $y \sim 0.8$, $z \sim 0.05$)
LNO	$LaNiO_3$
Gadolinium cathodes	
GSC	$Gd_xSr_{(1-x)}CoO_3$ ($x \sim 0.8$)
GSM	$Gd_{(1-x)}Sr_xMnO_3$ ($x \sim 0.3$–0.6)
Yittria cathodes	
YSCF	$Y_{(1-x)}Sr_xCo_yFe_{(1-y)}O_3$ ($y = 0.7$, $x \sim 0.3$–0.8)
YCCF	$Y_{(1-x)}Ca_xCo_yFe_{(1-y)}O_3$ ($x = 0.2$, $y \sim 0.1$–0.7
YBCu	$YBa_2Cu_3O_7$
Strontium cathodes	
SSC	$Sm_xSr_{(1-x)}CoO_3$ ($x \sim 0.5$)
NSC	$Nd_xSr_{(1-x)}CoO_3$ ($x \sim 0.8$)
BSCCu	$Bi_2Sr_2CaCu_2O_8$
Praseodymium cathodes	
PSM	$Pr_xSr_{(1-x)}MnO_3$ ($x \sim 0.65$)
PCM	$Pr_xCa_{(1-x)}MnO_3$ ($x \sim 0.7$)
PBC	$PrxBa_{(1-x)}CoO_3$ ($x \sim 0.5$)

Acronym	Representative chemical formulas
Zirconia electrolytes	
YSZ	$(ZrO_2)_{1-x}(Y_2O_3)_x$ ($x \sim 0.08$–0.1)
SSZ	$(ZrO_2)_x(Sc_2O_3)_{1-x}$ ($x \sim 0.8$)
CaSZ	$Zr_{0.85}Ca_{0.15}O_{1.85}$
Ceria electrolytes	
GDC	$Ce_xGd_{1-x}O_y$ ($x \sim 0.8$, $y \sim 1.8$)
SDC	$Ce_xSm_{1-x}O_y$ ($x \sim 0.8$, $y \sim 1.9$)
YDC	$Ce_xY_{1-x}O_y$ ($x \sim 0.8$, $y \sim 1.96$)
CDC	$Ce_xCa_{(1-x)}O_y$ ($x \sim 0.9$, $y \sim 1.8$)
Lanthanum electrolytes	
LSGM	$La_xSr_{1-x}Ga_yMg_{1-y}O_3$ ($x \sim 0.9$, $y \sim 0.8$)
LSGMC	$La_xSr_{1-x}Ga_yMg_{1-y-z}Co_zO_3$ ($x \sim 0.8$, $y \sim 0.8$, $z \sim 0.085$)
LSGMF	$La_xSr_{1-x}Ga_yMg_{1-y-z}Fe_zO_3$ ($x \sim 0.8$, $y \sim 0.5$, $z \sim 0.4$)
LSGMCF	$La_{0.8}Sr_{0.2}Ga_{0.32}Mg_{0.08}Co_{0.2}Fe_{0.4}O_3$
$LaAlO_3$-based	$La_{1-x}Ca_xAlO_3$ ($x = 0.0027$–0.008), $La_{1-x}Ba_xAlO_3$ ($x = 0.1$)
Others	
BCY	$BaCe_xY_{1-xy}O_3$ ($x \sim 0.25$)
YSTh	$(ThO_2)_{1-x}(Y_2O_3)_x$ ($x \sim 0.08$–0.1)
YSHa	$(HfO_2)_{1-x}(Y_2O_3)_x$ ($x \sim 0.08$–0.1)
Bismuth oxide-based	$(Bi_2O_3)_x(Nb_2O_5)_{1-x}$ ($x \sim 0.25$)
Pyrochlorores-based	YZr_2O_7, $Gd_2Ti_2O_7$
Barium brownmillerites	$BaZrO_3$, $Ba_2In_2O_5$, $Ba_3In_xAO_y$ (A = Ti, Zr, Ce, Hf), $Ba_3Sc_2ZrO_8$
Strontium brownmillerites	$Sr_2ScAl_xA_yO_z$ (A = Mg, Zn), Sr_2ScAlO_5, $Sr_3In_2HfO_8$

Figure 1.11. Acronyms for the materials shown in Figure 1.10. Extracted from [41].

1.2.2.1.Electrolyte

The ideal electrolyte for these devices should be a good ionic conductor and an electronic insulator, to allow oxygen mobility and avoid short circuits between the electrodes. Moreover, it needs to be dense, gas-tight and chemically stable in both oxidising and reducing conditions (as well as in the half-reactions). It should also be chemically and thermally compatible with the adjacent cell components (non-reactive and matching thermal expansion

coefficients, TEC). All this plus its thickness will have a major impact on the overall performance of the cell. [5,25,28]

These characteristics are usually met when using ceramics with a fluorite-like structure, where the oxygen vacancies enhance the transport of oxygen ions (O^{2-}) within it. The state-of-the-art materials include YSZ (yttria-stabilised zirconia, 8% Y_2O_3 in a ZrO_2 matrix) and GDC (gadolinia-doped ceria, $Gd_{0.1}Ce_{0.9}O_{1.95}$) for high and intermediate temperatures (HT and IT), respectively. Furthermore, variations of the doping element have been studied to enhance the properties of the materials, for example, Yb or Sc instead of Y in YSZ and Sm and Tb in GDC. Despite achieving the highly-desired increase in performance, these components are much more expensive (and less abundant) and not so stable in long-term operation, and therefore, generally not used.

Figure 1.12 shows the electronic conductivity variation with temperature for several studied electrolytes. YSZ continues to be the more effective and most used electrolyte for SOFC applications notwithstanding its low conductivity at low and intermediate temperatures (it falls from 0.1 S cm^{-1} at 1000°C to 0.02 S cm^{-1} at 800°C), and chemical reactivity with Sr-containing state-of-the-art electrodes. [5,25,28,42]

Nowadays, GDC and ceria-based electrolytes are preferred for IT applications due to lower activation energy and good ionic conductivity (one order of magnitude larger than YSZ at this temperature range, shown in Figure 1.12). In addition, these electrolytes have higher TECs (12.5×10^{-6} K^{-1}, 20% larger than YSZ) that match better with the other components of the cell. Nonetheless, ceria-based electrolytes still present different drawbacks that restrict their commercialisation, in particular, the reduction of Ce^{4+} to Ce^{3+} in reducing conditions

which leads to a detriment in the cell voltage due to direct electronic conduction and short-circuit problems, and lattice expansion, causing microcracking and gas leakage. [28,42]

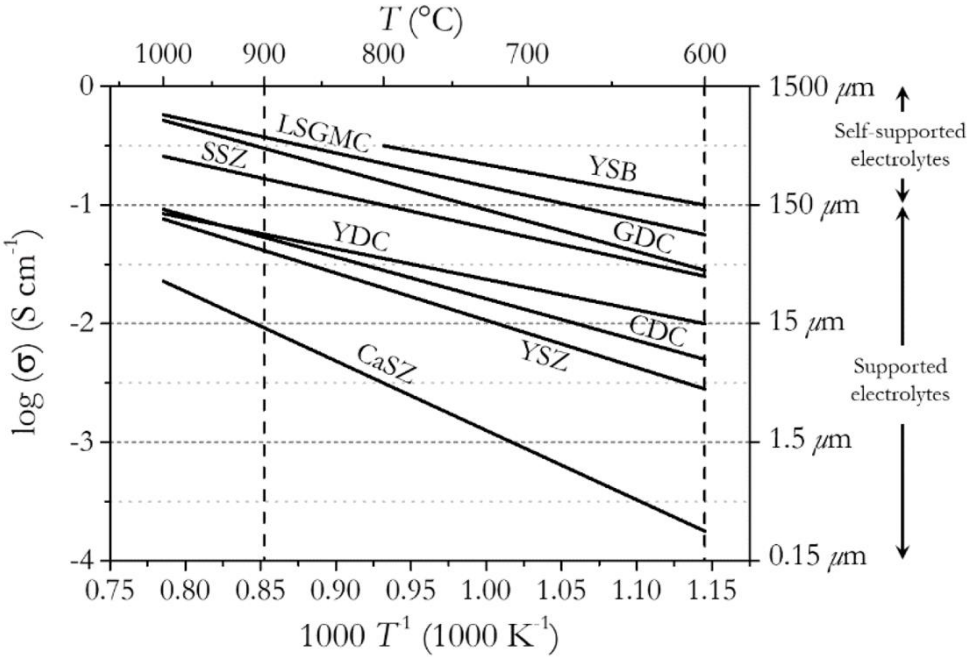

Figure 1.12. Ionic conductivities of the main electrolyte materials used in SOFC applications. The presented electrolytes are: YSB [$(Bi_2O_3)_{0.75}(Y_2O_3)_{0.25}$]; LSGMC ($La_xSr_{1-x}Ga_yMg_{1-y-z}Co_zO_3$; x≈0.8, y≈0.8, z ≈0.085); GDC ($Ce_{0.9}Gd_{0.1}O_{1.95}$); SSZ [$(ZrO_2)_{0.8}(Sc_2O_3)_{0.2}$]; YDC ($Ce_{0.8}Y_{0.2}O_{1.96}$);CDC ($Ce_{0.9}Ca_{0.1}O_{1.8}$);YSZ [$(ZrO_2)_{0.92}(Y_2O_3)_{0.08}$] and CaSZ ($Zr_{0.85}Ca_{0.15}O_{1.85}$). Extracted from [35].

1.2.2.2.Electrodes

As mentioned above, solid oxide cells in general are a relatively new technology. For this reason, the majority of the materials that are being investigated for their application on reversible SOC (electrodes, electrolytes, interconnectors, seals, etc.) are based on the ones that have exhibited better performance in SOFC mode, which was studied first. [5,43,44]

Although at first glance the requirements and characteristics of an rSOC may seem to be a combination of the requirements of both modes separately, it is not that simple. The change in operation between one mode and the other requires the inversion of the ion flow in the cell and the inversion of the electrodic reactions. These changes must simultaneously level or exceed the efficiency of the inverses to make a good electrolyser cell from the energy generation device. To cite an example, one of the main requirements for the oxygen electrode for SOECs is that it should not delaminate at high oxygen pressures resulting from the oxygen evolution reaction taking place. [16,45]

Both SOFCs and SOECs generally use ceramic oxides, ideally mixed ionic and electronic conductors (MIEC), for their main components: porous electrodes. Although there are differences in their compositions for SOFC/SOEC, they share some general requirements: high ionic conductivity, acceptable values of electronic conductivity to allow a homogeneous charge exchange, high electrochemical activity and high porosity to promote the diffusion of gaseous species. It is also desirable for them to be mechanically and chemically compatible with other components of the cell, stable at operating temperature, cheap and easy to prepare. [16,43,46–49]

Oxygen electrode

The oxygen (or air) electrode is where the oxygen evolution reaction (oxygen formation, SOEC mode) and the oxygen reduction reaction (oxygen reduction, SOFC mode) take place. Therefore, it must be stable in oxidising environments and have high porosity to enable the diffusion of gas species in and out of the interface. Moreover, it should present high electrocatalytic activity towards both ORR and OER, something not so simple to achieve.

Microstructure also plays a key role here, since the electrochemical reactions mentioned only take place in the active area of the electrode, where electrons, oxide ions and molecular oxygen coexist. For pure electronic conductors, this area is confined to the Triple Phase Boundary (TPB). When it comes to air electrodes, the approach used to increase this area is the use of mixed ionic-electronic conductors (MIECs); in these materials, all the surface area can potentially be active towards chemical reactions (two-phase boundary, 2-PB, solid/gas) because they provide both electrons and ions needing thus, only the gas phase. Figure 1.13 shows a schematic illustration of the pathways electrons and ions take in different types of materials. Most of the MIECs used in SOC applications are ceramic oxides with perovskite-type and related structures.

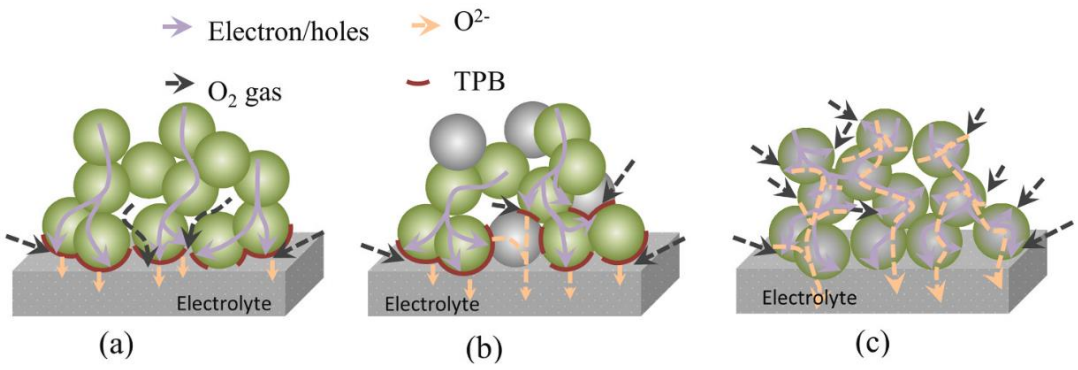

Figure 1.13. Schematic diagram of the oxygen reduction pathways in a pure electronic conductor (a), a composite ionic-electronic conductor (b) and a single-phase mixed ionic-electronic conductor (c). Extracted from [6].

The versatility of perovskites -which also exhibit other properties of technological interest (electrical, elastic, magnetic, multiferroic, catalyst)- lies in the virtually infinite number of compounds that can be obtained using different combinations of elements that they admit and the diversity of resulting physicochemical properties. Different perovskite-

type structures are organised in families, which include simple, double, triple, Ruddlesden-Popper types, etc. [50]

The ideal cubic perovskite structure (Figure 1.14) belongs to the $Pm\bar{3}m$ space group and has the general formula ABO_3 (oxide), where A is typically a lanthanide or alkaline-earth and B is a transition metal, and the oxygens are arranged in corner-sharing BO_6 octahedra. Both the A or B cations can be substituted by introducing other cations with the same or different valence. The size of the cations occupying the different sites will determine the symmetry of the arrangement (and the degree of distortion) and therefore the space group symmetry of the structure, which can diverge from cubic to trigonal $R\bar{3}c$, tetragonal $P\,4/m\,mm$ or orthorhombic $Pnma$ in the most frequently studied materials.

Their high electrochemical activity is owed to their good transport and catalytic properties, which are directly related to the properties of the metallic cations present. The formation of oxygen vacancies that occurs when doping the compound (mixed-valence cation substitution provokes oxygen loss to ensure electroneutrality) enables the movement of the oxide-ion within the lattice. The new structure is noted as $ABO_{3-\delta}$ with δ=oxygen loss. This oxygen non-stoichiometry varies with temperature, pO_2 pressure and concentration of the dopant, among others. Moreover, the electronic conduction is assured by the mixed valence capacity of 3d metals, while the presence of active sites on the surface of the materials derived from the 5-fold coordination of the transition metal cation (Co, for example), enhances their catalytic activity. [6,13,25,45,50,51]

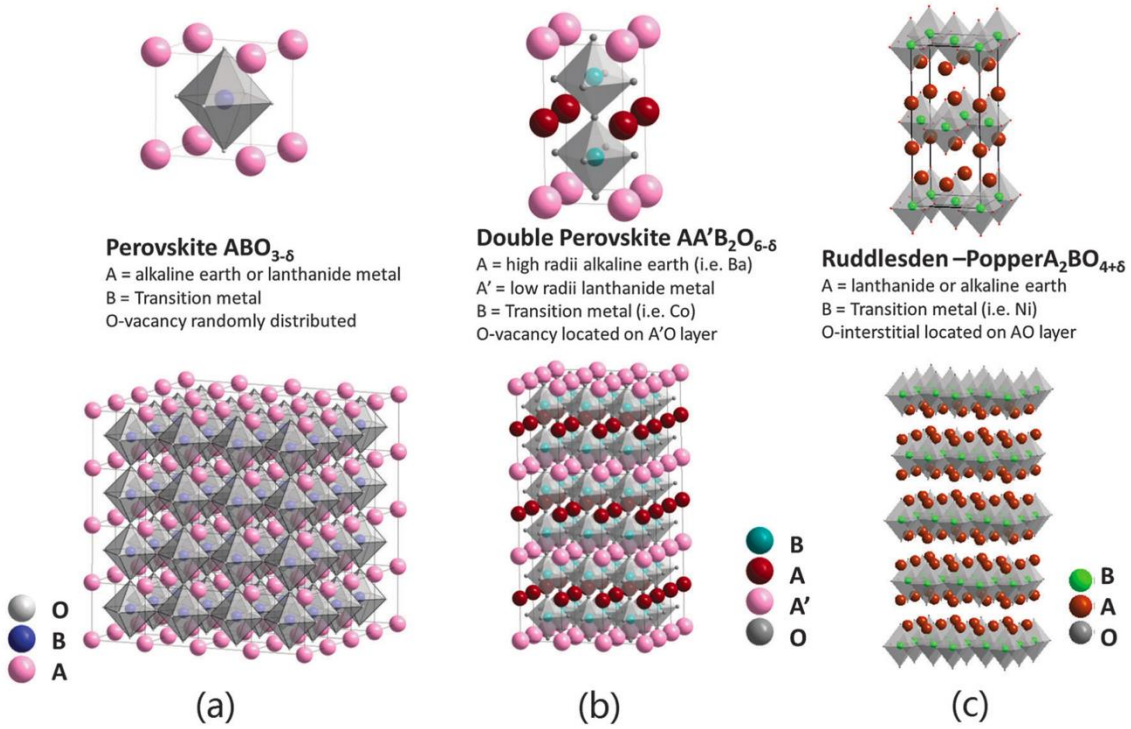

Figure 1.14. Crystal structures of the relevant MIEC cathode materials: simple perovskite (**a**) double perovskite (**b**) and Ruddlesden-Popper (**c**). Extracted from [52].

Among perovskites, $LaMnO_3$ (LM), $La_{0.8}Sr_{0.2}CoO_3$ (LSC) and $La_{0.8}Sr_{0.2}FeO_3$ (LSC) doped with alkaline earth metals in the A site and Ni, Mn and other transition metals in the B site, as well as other derived structures, have been widely studied through the years not only as SOFC cathodes but as general catalysts for other reactions [53]. State-of-the-art materials for air electrodes currently include lanthanum ferrites or cobaltites that exhibit MIEC behaviour, like LSCF ($La_{0.6}Sr_{0.4}Co_{0.2}Fe_{0.8}O_{3-\delta}$), BSCF ($Ba_{0.5}Sr_{0.5}Co_{0.8}Fe_{0.2}O_{3-\delta}$), $Sr_2Fe_{1.5}Mo_{0.5}O_{6-\delta}$ and LSC itself. [28,32,51,54,55]

Despite the great electrochemical performance of Co-based electrodes, new alternatives have been sought, due to cobalt's high toxicity and cost and a large TEC of the materials due to a very fast oxygen release of these oxides at high temperatures, also referred to as chemical

expansion. In the last years, its substitution for environmentally friendly and accessible copper appeared as an interesting alternative and has turned out to be quite beneficial [56–62]. $La_{0.6}Sr_{0.4}Fe_{0.8}Cu_{0.2}O_{3-\delta}$ perovskite was first reported by Zhou et al. [63] in 2009 and later resumed by Vázquez et al. [62], but never fully studied as an oxygen electrode in both SOFC and SOEC modes.

Composites

Composite electrodes, formed by a homogeneous mixture of a typical MIEC material and an electrolyte-like companion, arose as an interesting approach to reduce the TEC and improve the electrochemical performance of the electrode. One of the most used strategies is introducing an ionic conducting electrolyte material, such as GDC, or a simple transition metal or lanthanide oxide (like CeO_2). The introduction of a proper quantity of electrolyte material not only lowers the TEC but also increases the TPB area in the electrode, and the diffusion rates and charge transfer of oxygen ions at the interface. On the contrary, an excess of this material in the composite can taper the electrochemical performance of the cell. [28]

A schematic diagram of the effects the addition of small amounts of the electrolyte can produce in the mechanism of the ORR is shown in Figure 1.15.

The conventional method used to prepare these composites is mechanical mixing of the two already-synthesised components (oxygen electrode and electrolyte materials), which presents several disadvantages in terms of the resulting microstructure of the electrode since it cannot be optimised nor controlled in any way. Another interesting route on the rise is the wet impregnation technique, where the majority component electrode material is

impregnated with a solution of the corresponding metallic nitrates of the minor component, which are later decomposed by firing them in air to obtain the desired phase. [64,65]

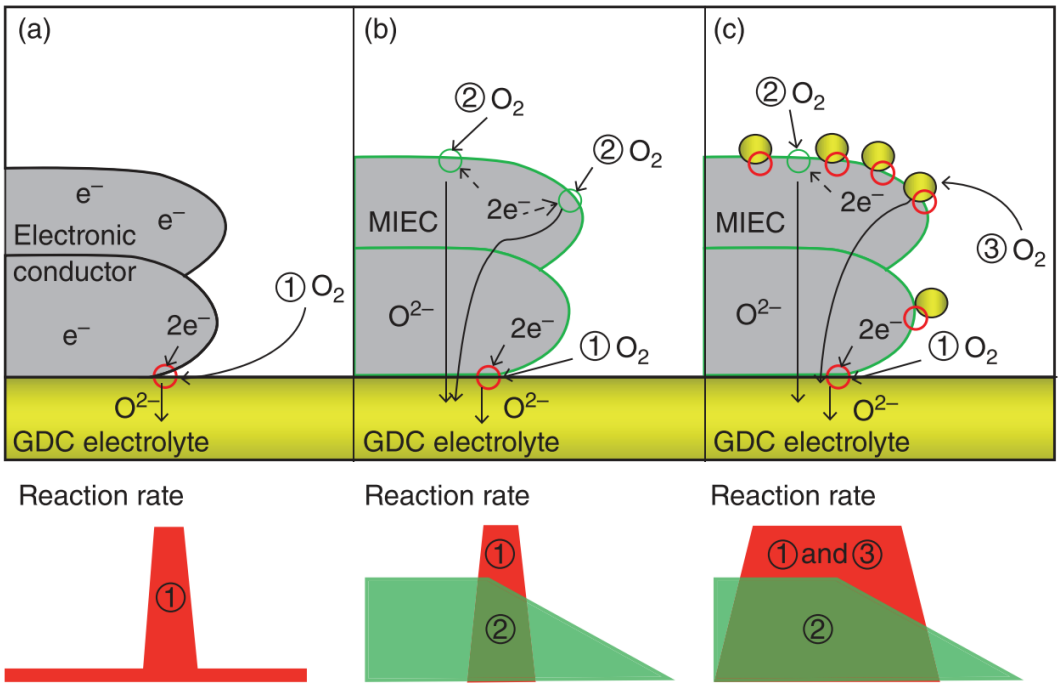

Figure 1.15. Schematics of the oxygen reduction reaction at (a) electronic conductor (TPB concept), (b) MIEC (TPB+ 2PB), and (c) MIEC-ionic conductor, GDC (enlarged TPB+2PB) (path 1: TPB point between the electrolyte and cathode, path 2: 2PB point on the surface of the cathode, and path3: enhanced TPB point by the addition of GDC). Extracted from [28].

Fuel electrode

The fuel (or hydrogen) electrode is where the hydrogen evolution reaction (steam reduction, SOEC mode) and the hydrogen oxidation reaction (steam formation, SOFC mode) take place. Therefore, it must be stable in reducing environments, exhibit high catalytic activity towards the hydrogen evolution and oxidation reactions (HER and HOR respectively) and have high porosity to enable the diffusion of gas species in and out of the

electrolyte/electrode interface. As mentioned above, other highly-desired characteristics include a matching TEC to that of the electrolyte, chemical and thermal stability when in contact with other components of the cell and tolerance to impurities/chemical poisons like sulphur.

As SOFC devices were the first ones studied, all of the materials tested in fuel electrodes of SOC are the ones previously used as SOFC anodes. The most commonly used are cermets: ceramic-metal composites where the ceramic material is the same as the electrolyte and the metal is a catalyst [28,32,51,55,66]. Due to the presence of a metallic phase and a ceramic one, the material presents mixed conductivity (the metal contributes to the electrical conductivity) and provides mechanical stability to the cell. They are usually obtained by mixing the oxide of the metal and the electrolyte (or directly the composite) and are reduced *in situ* to obtain the metallic phase dispersed homogeneously in the electrode.

The most popular cermets include Ni-GDC and Ni-YSZ, and their variants with elements such as samarium and scandium, respectively. Despite presenting several disadvantages like Ni segregation and poor mechanical stability when re-oxidised (in presence of air or oxygen), Ni-YSZ continues to be the reference material for SOCs. In the last decade, different perovskites have also emerged as potential fuel electrodes to substitute traditional cermets. [28,32,67,68]

1.2.3. Materials characterisation techniques

1.2.3.1.X-Ray Powder Diffraction (XRD)

Conventional powder X-ray diffraction (XRD) is a rapid non-destructive technique used to identify and/or quantify the crystallographic composition of a material formed by one or more crystalline phases. Specialised XRD (with data collected at specialised instruments/laboratories and properly processed) could be used for crystal structure determination, quantification of microstructure, instrument calibration, and the quantitative study of other complex systems. It is commonly employed in materials science for composition analysis and phase identification of crystalline phases, which can be in the form of powders, pellets or thin films, owing to the 'fingerprint' quality of the diffraction patterns obtained.

The electron density of long-range ordered structures, or crystals, scatter X-rays in every direction. In some specific ones, the scattered X-rays add up constructively to produce diffraction peaks and, consequently, diffraction patterns. The position of the peaks in this pattern was explained in 1913 by W.L. Bragg and W.H. Bragg in the famous Bragg´s Law:

$$n\lambda = 2d \sin\theta \qquad (1.12)$$

where λ is the wavelength of the X-ray radiation, d is the interplanar spacing of the planes within the crystal, θ is the angle of incidence above the plane surface, and n is an integer. This implies that constructive interference only occurs when the conditions of Bragg´s law are satisfied, in other words, diffraction is possible when the difference in the optical path

length between reflections of adjacent planes is a whole number of waves (or the phase shift of the waves is a multiple of 2π, Figure 1.13a).

The wavelength of the X-rays is of the same order of magnitude as the distance between the scattering centres used to produce the pattern: the atoms within the crystal, and consequently, allows us to obtain significant information about the inner structure of a material. [69,70]

The XRD data collected will be fitted using the Rietveld method to obtain structural parameters and information about the composition of the samples. [71]

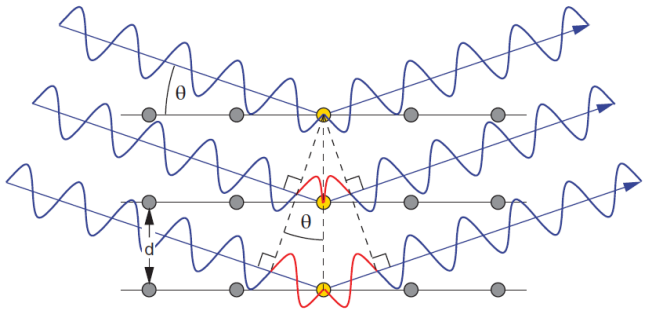

Figure 1.13. Schematic representation of Bragg's Law. Extracted from [69].

1.2.3.2.Scanning Electron Microscopy (SEM)

Scanning electron microscopy is one the most used analytical techniques in the study of the surface nano- and micro-structured materials. The generation of a beam of high-energy electrons by an electron gun focused by magnetic lenses, allows the scanning of the sample maintained under high-vacuum conditions, and therefore, the acquisition of high-resolution micrographs (Figure 1.14a).

The interaction of these electrons with the surface of the sample generates a variety of signals that are detected by the corresponding detector, the typical pear scheme of them is shown in Figure 1.14b. The most common detectors are the following:

- *Secondary Electron detector (SE).* Captures the electrons emitted by the atoms of the material under study after the excitation caused by the scanning beam (secondary electrons); they provide textural and topography information, as they come from the outermost layer (the 'pear' closest to the surface).
- *Backscattered Electron detector (BSE).* This detector captures the electrons of the scanning beam that are not absorbed by the sample but deviated back from the surface of the sample, coming from the second layer of the pear, which gives us information about the composition of the sample due to its high atomic number sensibility. Different shades of grey will be observed depending on the atomic weight of the element (clearer if it is heavier since it backscatters more electrons).
- *Energy Dispersive X-ray detector (EDX).* It captures the X-rays generated in the third layer of the pear, characteristic for each element, which yields not only qualitative information about atomic composition but also a semi-quantitative analysis of the surface. EDX can be used to study a specific point of the sample, map a line or even scan through an area creating a compositional map of the surface of the sample. [34,70,72]

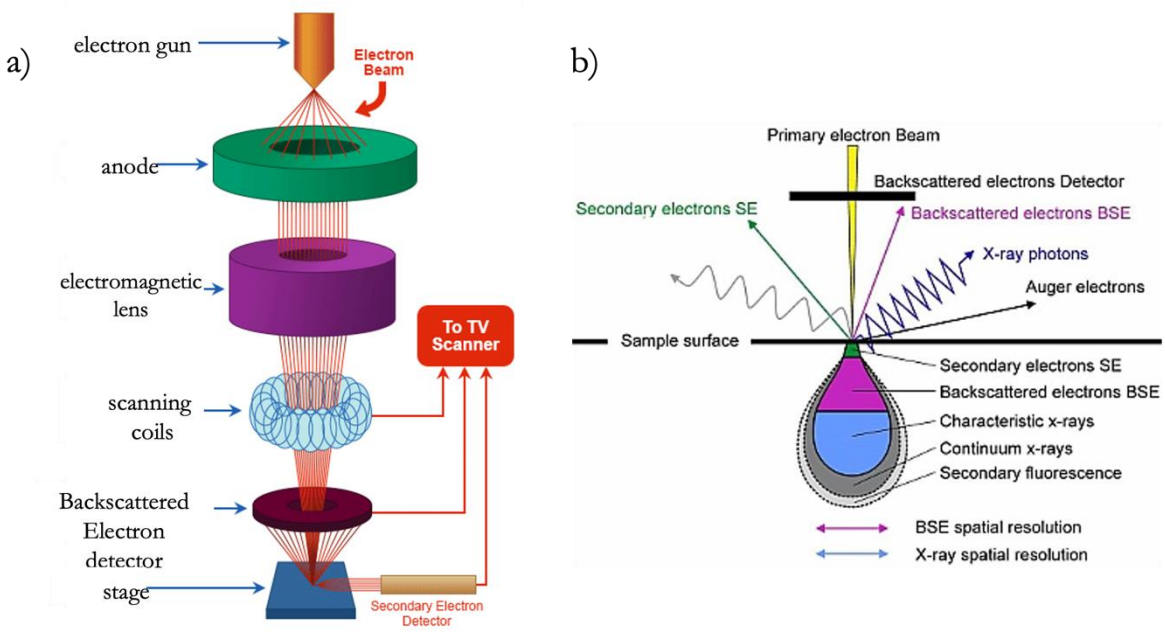

Figure 1.14. Diagrams of a scanning electron microscope working principles (a) and the various signals generated when the electron beam interacts with the sample (b). Extracted from [73] and [74].

1.3. Objectives of the thesis

Taking into consideration the path the group has followed with regard to the development of new materials for Solid Oxide Fuel Cells, it only feels natural to keep moving towards their complementary devices: Solid Oxide Electrolyser Cells and also, to study the possibility of reversible operation.

Thus, the aim of this thesis is to improve the performance of already-existing materials for SOCs oxygen electrodes and test them in reversible conditions (SOFC/SOEC) using state-of-the-art electrolyte and fuel electrodes.

In this regard, the synthesis of $La_{0.6}Sr_{0.4}Fe_{0.8}Cu_{0.2}O_{3-\delta}$-$CeO_2$ (LSFCu-CeO_2) composites in a two-step facile method was proposed and the resulting materials were characterised microstructurally and electrochemically to determine their suitability as oxygen electrodes. Moreover, the composites were tested as SOC's oxygen electrodes using commercial electrolytes and fuel electrodes, in both SOFC and SOEC modes.

According to this, the thesis focused on the following aspects:

- Two-step synthesis of LSFCu-CeO_2 composites using an auto-combustion method.
- Optimisation of the preparation of symmetrical and full-cell devices for electrochemical characterisation.
- Study of the performance of full devices employing the best-performing oxygen-electrode materials.

Chapter 2

-EXPERIMENTAL METHODS-

2. EXPERIMENTAL METHODS

This chapter aims to provide a general overview of the experimental methods and techniques used in this thesis, from the synthesis of the materials to the preparation of inks that were later employed in the assembly of the devices tested electrochemically, as well as the characterisation techniques involved in each step.

2.1. Materials synthesis

The electrode materials studied in this work were synthesised via an auto-combustion route, using ethylenediaminetetraacetic acid (EDTA) as organic fuel and chelating agent, and ammonium nitrate (NH_4NO_3) as combustion promoter. This method allows obtaining the LSFCu perovskite and LSFCu-CeO_2 composites in two steps: synthesis and posterior thermal treatment. In comparison to other methods, it is faster, cheaper (since it requires less time performing thermal treatments and consequently, less energy) and also scalable, considering that each synthesis can produce 5-10 g of the material. [57,62,75–77]

For this purpose, aqueous solutions containing stoichiometric amounts of $La(NO_3)_3{\cdot}6H_2O$, $Sr(NO_3)_2$, $Fe(NO_3)_3{\cdot}9H_2O$, $Cu(NO_3)_2{\cdot}3H_2O$, $Ce(NO_3)_3{\cdot}6H_2O$ (>99.9 %, Sigma Aldrich, USA) were prepared according to the desired composition. An alkaline solution (pH=10) containing 1.1 moles of EDTA (>99.4%, Sigma-Aldrich, USA) per mole of cation and NH_4NO_3 (>99.0 %, Sigma-Aldrich, USA) was also prepared and the solutions above were mixed. The resulting solution was heated over a hot plate at 130 °C, constantly stirring and keeping pH=10 constant by adding small aliquots of NH_4OH as required, until

the formation of a gel. Then, the magnetic stirrer was removed and the hot plate temperature was raised to 350 °C, where the gel self-ignited. A brief schematic diagram of the process is shown in Figure 2.1.

The combustion process resulted in a sponge-like dark brown powder, that after a grinding process in an agate mortar becomes a fine and homogeneous powder. After that, the samples were subjected to a heating treatment in a muffle furnace at 850 °C in air for 6 h to obtain the desired pure materials.

Some key aspects of the synthesis were previously optimised (by the author and other members of the group) to obtain the desired phases. First, the EDTA molar excess, which ensures the total complexation of the metallic cations, avoiding the formation of hydroxides and oxy-hydroxides that commonly occurs at high pH. Second, the NH_4NO_3:EDTA molar ratio -which is a fully experimental parameter since it has to be tailor-made for each perovskite (or family of perovskites)- has a direct influence on the composition of the final ashes. Higher ratios (8:1, 10:1, 12:1) might allow the preparation of the desired phase directly from the synthesis, while lower ratios (3:1, 4:1, 5:1) lead to amorphous or low-crystallinity phases. In this case, higher ratios produce a mixture of the metallic oxides (CuO, La_2O_3, SrO, Fe_2O_3, etc.) instead of the perovskite; therefore, the preparation was carried out using a 3:1 NH_4NO_3:EDTA ratio and a posterior thermal treatment at 850 ºC in air that resulted in the desired phases.

The samples containing pure $La_{0.6}Sr_{0.4}Fe_{0.8}Cu_{0.2}O_{3-\delta}$, and $La_{0.6}Sr_{0.4}Fe_{0.8}Cu_{0.2}O_{3-\delta}$-$CeO_2$ mixtures with 5%, 10%, 20% and 50% CeO_2, will be called LSFCu, LSFCu-CeO_2 5, LSFCu-CeO_2 10, LSFCu-CeO_2 20 and LSFCu-CeO_2 50, respectively.

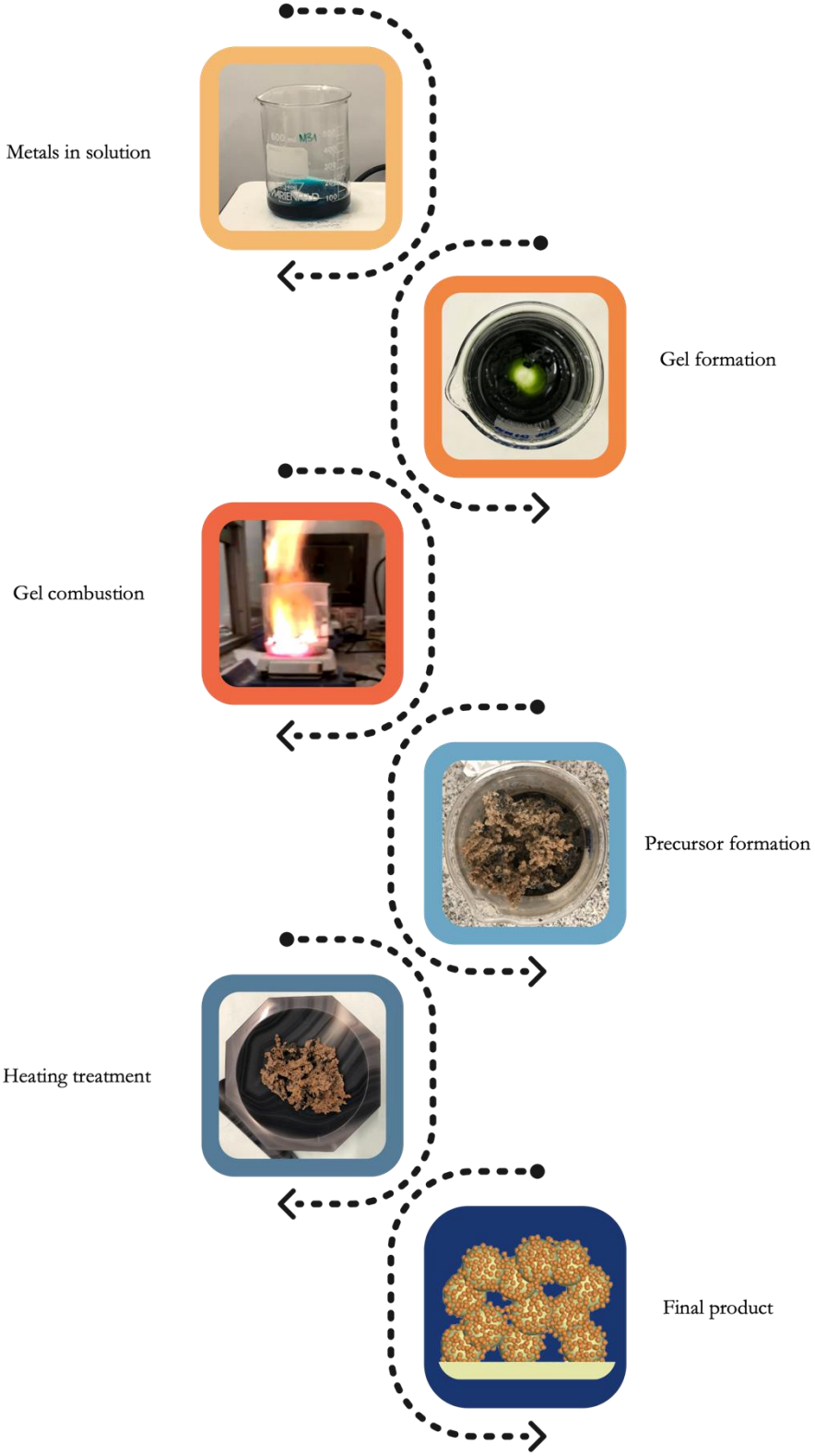

Figure 2.1. Diagram of the synthesis process used to obtain the LSFCu perovskite and LSFCu-CeO_2 composites.

2.2. Inks for SOC fabrication

This section describes the formulation of the inks used in this thesis. Table 2.1 shows an overview of the materials and solvents employed as well as the deposition method and the part of the device it was used for.

Table 2.1. Summary of the prepared inks of the materials used for different components of the cell.

	Materials	**Deposition technique**	**Part of the device**
Ethanol-based inks	GDC	Airbrush	Roughness layer
Terpineol-based inks	LSFCu, LSFCu-CeO_2 composites	Hand-painted	Oxygen electrode

2.2.1. Ethanol-based inks

GDC ethanol-based inks were employed to deposit a thin GDC roughness layer (RL) over electrolyte substrates, which enhances the adhesion of the electrode's particles to the electrolyte support. These inks were prepared by mixing 0.1 g of commercial GDC powder (Fuelcellmaterials, USA) with 0.001 g of PVP dispersant (1% in weight with respect to the solid load, Mw 55k, Sigma Aldrich, USA) in 1 g of EtOH. The dispersions were magnetically stirred for ~12 h and sonicated right before their use.

The composition used for these inks was previously optimised for their deposition by the airbrushing technique by the NIFC group (IREC, Barcelona, Spain).

2.2.2. Terpineol-based inks

The inks of LSFCu perovskite and LSFCu-CeO_2 composites were obtained by dispersing 500 mg of the powders in PVA (Mw 89k, Sigma Aldrich, USA), α-terpineol (96%, Alfa Aesar, USA) and isopropanol (28.3, 1.1, 45.2 and 25.4 % w/w respectively). The dispersions were magnetically stirred for ~12 h and sonicated before their use.

2.3. Fabrication of SOC test devices

The fabrication of testing devices implies putting together all the aforementioned components and verifying their stability at operating (or as similar as possible) conditions. Thus, chemical and mechanical compatibility between the oxygen electrode and the electrolyte should be tested before performing the electrochemical characterisation.

The chemical compatibility was studied through the phase reaction of the electrolyte and the electrodes. In this case, two different electrolytes were used: GDC for symmetrical cells and YSZ for full cells.

The reactivity between the electrodes and the GDC was examined directly over the LSFCu-CeO_2 composites owing to the similarity between the CeO_2 component and the GDC. For this, the LSFCu-CeO_2 10, 20 and 50% samples were fired in air at 1100 ºC for 12 h and XRD patterns of the resulting materials were collected.

On the other hand, it is well known that Sr-containing phases (like LSFCu) react with YSZ at high temperatures to form the $SrZrO_3$ and $La_2Zr_2O_7$ insulating phases, which have a

direct effect on cell performance and its deterioration [78–83]. Since there was no point in verifying this fact again, we decided to apply a GDC barrier layer (BL) between the electrolyte and the electrode when testing on YSZ-containing cells. The function of this BL is to avoid or, at least, delay, the contact between the Sr and Zr and in consequence, their reaction.

The mechanical compatibility of materials is studied through their Thermal Expansion Coefficient (TEC), a property usually measured using the dilatometry technique (the change in the linear dimension of a sample with temperature is recorded). The test was not performed due to the lack of equipment, but abundant literature concerning the TEC of the individual components can be found elsewhere. The value reported for GDC (30-730 ºC) is 12.5×10^{-6} K^{-1}, while the one for LSFCu (25- 850 ºC) is 14.6×10^{-6} K^{-1} (average). [42,58,62,63,84]

Later on, Vazquez et al.[62] reported that the LSFCu perovskite exhibits a reversible phase transition ~425 ºC from the rhombohedral $R\bar{3}c$ to the cubic $Pm\bar{3}m$ structure (in accordance with weight losses observed in thermogravimetric analysis, TGA). The TEC for both phases (obtained through the study of the lattice parameters of high-temperature XRD data), in the ranges RT-425 ºC and 425-900 ºC, were 14.66×10^{-6} K^{-1} and 18.62×10^{-6} K^{-1}, respectively (16.64×10^{-6} K^{-1} in average).

The phase transition might translate into a significant change in the TEC with temperature and consequently a huge disadvantage if we take into account the multiple heating/cooling cycles the device affronts while operating. This is detrimental to the cell and could eventually lead to mechanical failure. Here, the mixture of the electrode with a material similar to the electrolyte (CeO_2, TEC~ 12×10^{-6} K^{-1}) could represent an important improvement for the mechanical stability of the device since the TEC of the mixture can be approximated to the average of the individual TECs.

To sum up, the components appear to be compatible enough to develop a high-performing device. The techniques used in the assembly of the cells are presented below.

2.3.1. Fabrication techniques

2.3.1.1.Airbrushing technique

The airbrushing technique consists of an airbrush with a nozzle on the tip, which uses pressurised air to nebulise the paint or ink (with different solid loading of diverse materials) on surfaces. It is commonly used in SOC manufacturing to deposit layers of porous electrodes on top of pre-existing substrates. [85,86]

In this thesis, a 3-axis automated airbrushing (Figure 2.2) controlled with a 3D printing frame (Print3D Solutions, Spain) was routinely employed to apply thin layers of GDC on top of electrolyte tapes and fuel electrode-supported half-cells. Different parameters like the air pressure, the temperature of the substrate holder and the distance airbrush – sample, among others, can be controlled during the process to get reproducible depositions.

During the deposition, the air pressure was fixed at 2 bar, the temperature of the holder was 70 ºC to ensure proper ethanol evaporation and the distance to the substrate was ~8 cm. The reproducibility of the result was controlled by the number of layers deposited.

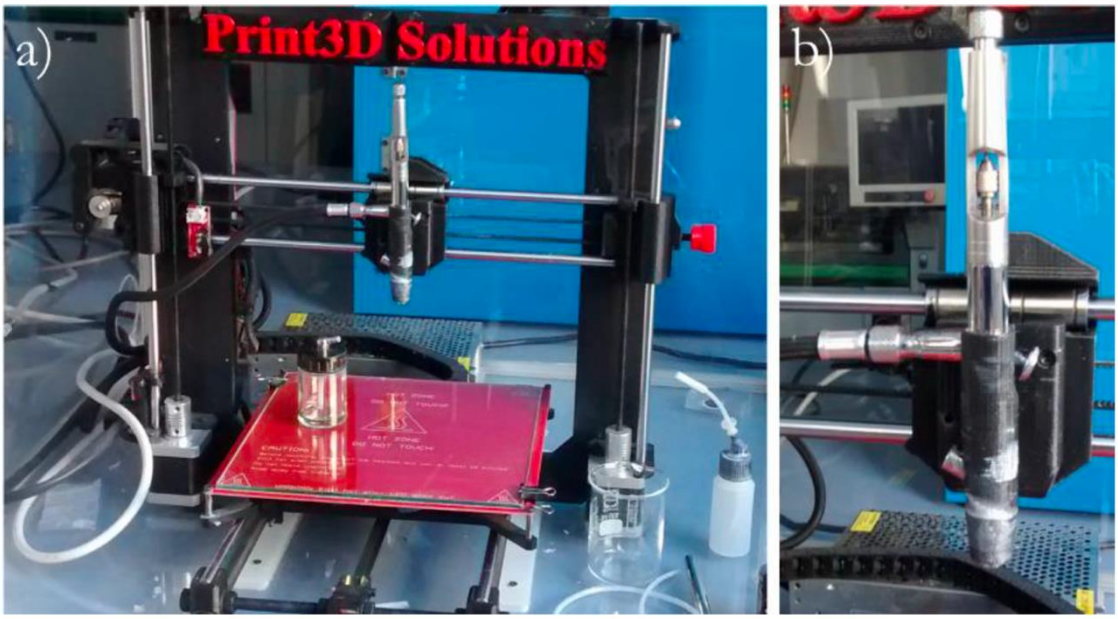

Figure 2.2. Automated airbrushing setup used for thin layer deposition (**a**) and airbrush (**b**).

2.3.1.2.Pulsed Layer Deposition (PLD)

PLD is a physical vapour deposition technique that allows to obtain high-quality thin films (from tens of nanometres to a few microns) of solid crystalline materials at lower temperatures than the ones employed in typical crystallisation processes in equilibrium conditions. As indicated by its name, this technique uses high-energy laser pulses to evaporate and ionise material from a target (Figure 2.3), which generates a plasma plume of ions that condense on top of the substrate. A system of lenses and mirrors directs the laser beam to the substrate, which is inside a chamber maintained under high vacuum conditions to minimise possible contamination. The substrate chamber can be heated to the desired temperature to improve the crystallisation process. [87]

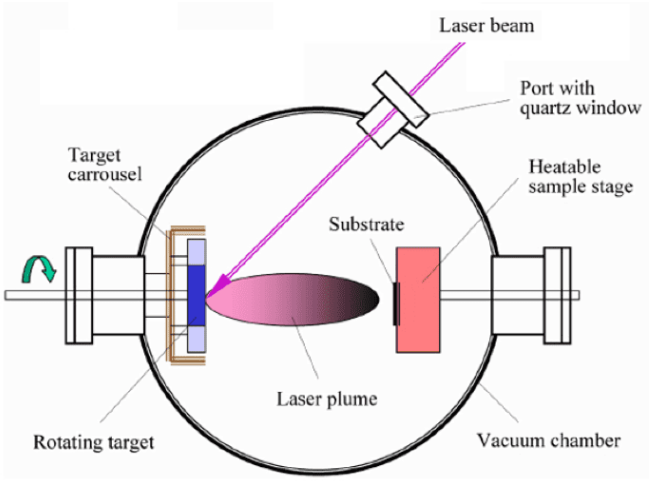

Figure 2.3. PLD working mechanism and setup diagram. Extracted from [34].

In the present work, PLD was used to deposit dense and thin GDC barrier layer films on commercial NiO-YSZ/YSZ fuel electrode-supported half cells. As mentioned before, the aim of this barrier layer (BL) is to introduce a physical barrier between the electrolyte (in this case YSZ) and the oxygen electrode avoiding the reaction among them, which would lead to the formation of insulating phases. Note that this step is not needed when using the GDC electrolyte but becomes critical when the electrolyte is YSZ.

The equipment used at the IREC facilities is a large-area PLD from PVD Products, Inc.® (Figure 2.4). During the deposition, performed by researchers of the NIFC group, the oxygen flow was kept in the range of 10^{-3} – 10^{-1} mbar, the temperature of the substrate was 600 ºC and the target was rotating constantly to deposit a homogeneous layer of GDC of ~1 μm in thickness.

Figure 2.4. PLD instrument located at IREC facilities.

2.3.2. Cells fabrication

This section describes the different cells prepared during this thesis, both symmetrical and full devices. Table 2.2 shows an overview of them and the materials used for each component.

Table 2.2. Summary of the prepared cells and the materials used for their construction.

Type	**Support**	**Electrolyte**	**Oxygen electrode**
Symmetrical cells	GDC pellet/ tape	GDC	LSFCu and LSFCu-CeO_2 composites
Full cells	NiO-YSZ/YSZ fuel electrode tape	YSZ	LSFCu and LSFCu-CeO_2 composites

2.3.2.1.Symmetrical cells

Electrolyte-supported symmetrical cells were prepared and electrochemically tested to measure the performance of the oxygen-electrode material and to optimise the electrodes' deposition and cell assembly procedure using GDC electrolytes of different origins and preparation.

First, the electrolyte consisted of GDC pellets prepared with commercial powder (Kceracell Co., Ltd., Republic of Korea) by pressing ~2 g in disks of 25 mm in diameter at 8 MPa and then annealed at 1450 ºC for 6h (2º/min up and 1 ºC/min down). A GDC ethanol-based ink (section 2.2.1.) was deposited on both sides through an airbrush to create the RL, which was later sintered at 1250 ºC for 2 h (5 º/min).

Secondly, the electrolyte consisted of GDC tapes (Fuelcellmaterials, USA), 20 mm in diameter and ~200 μm in thickness. These tapes with a very polished surface also required the deposition of a roughness layer (RL) before the application of the electrode material. A GDC ethanol-based ink was also deposited on both sides of the tapes.

In both cases, the electrodes' layer (terpineol-based ink, section 2.2.2.) was painted by hand on top of the electrolyte, and sintered in air at 950 ºC for 4h (5 º/min, with a pre-step of 1 h dwell at 500 ºC to remove all the organic components of the ink). Figure 2.5 shows a diagram of the final configuration of a symmetrical cell. Note: the determination of the sintering temperature of the electrodes will be discussed in Chapter 3.

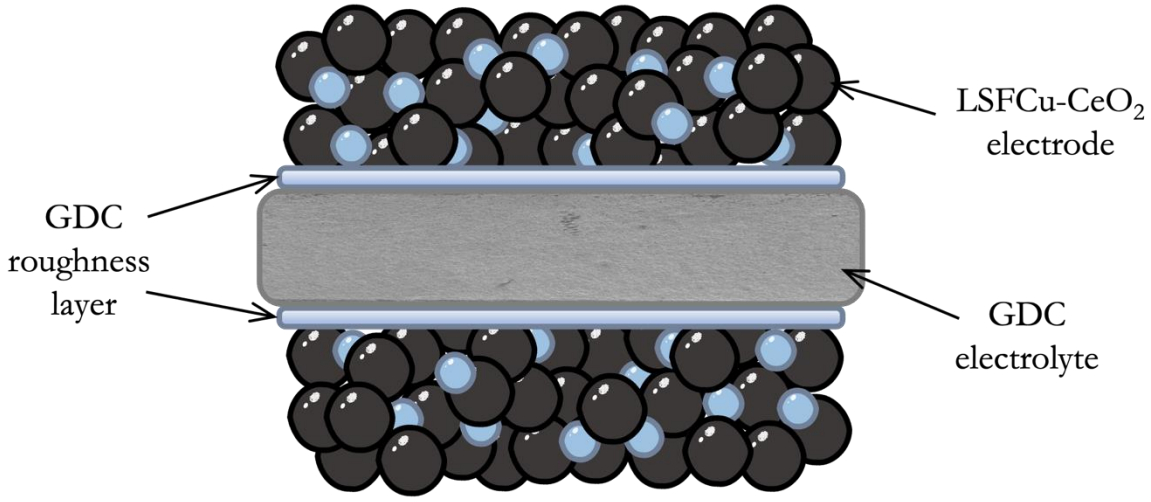

Figure 2.5. Schematic design of the symmetrical cell (electrode/GDC/electrode) used to study the oxygen electrode electrochemical performance. Modified from [35].

2.3.2.2.Fuel electrode-supported full cells

Full cells were prepared by the deposition of a GDC barrier layer (BL, ~1μm) on commercial anode-supported half cells (NiO-YSZ//YSZ) using the PLD technique. The half cells were provided by SOLIDpower SpA (Italy) and have 20 mm in diameter and ~300 μm in thickness. The BL was sintered in air at 1150 ºC for 2 h (5 º/min).

A GDC RL was deposited on top of the BL employing the airbrushing technique and subsequently fired in air at 1250 ºC for 2 h (5 º/min). The electrode layer was painted by hand using a 16 mm mask to guarantee a minimum area coverage and sintered in air at 950 ºC (with the same pre-step as symmetrical cells) to ensure their correct attachment to the RL.

An example of the resulting configuration of the full solid oxide cells is shown below in Figure 2.6:

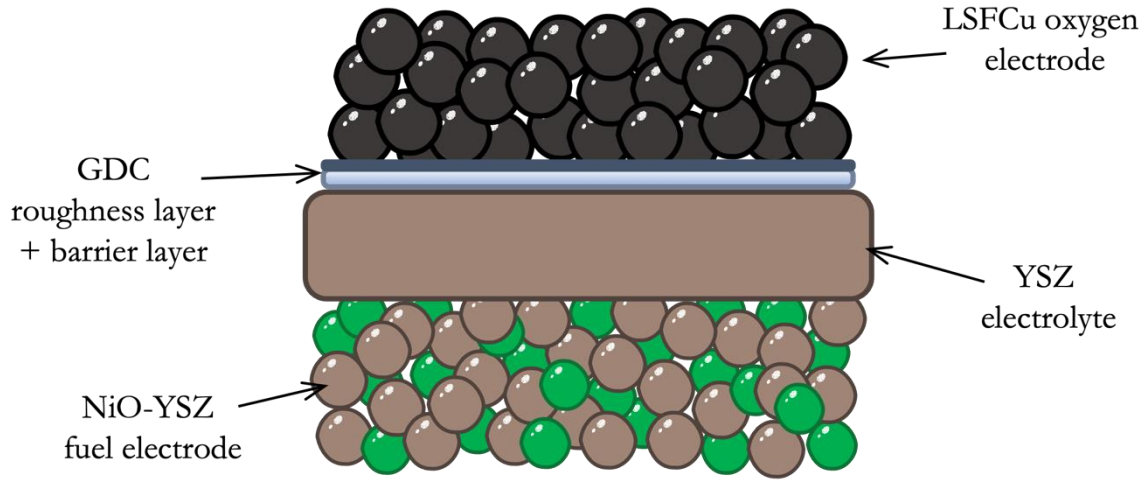

Figure 2.6. Schematic design of a full cell with the configuration NiO-YSZ/YSZ/GDC_{BL}/oxygen electrode. Modified from [35].

2.4. Characterisation techniques

2.4.1. Electrochemical characterisation

As mentioned above, all the prepared button cells (both symmetrical and full cells) are circular and have 2 cm of diameter and a theoretical active area of ~2 cm^2. The characterisation techniques used include I-V polarisation curves and Electrochemical Impedance Spectroscopy (EIS). The experimental setups employed and the techniques used for this, are described in the following sections.

2.4.1.1.Experimental set-up

The electrochemical characterisation of symmetrical cells was carried out by using a commercial ProboStat™ station (NorECS AS, Norway), a high-temperature vertical tubular furnace with thermal control system and a Novocontrol spectrometer (impedance analyser, Novocontrol Technologies GmbH & Co., Germany). The gas flow consisting of synthetic air for the symmetrical cells or hydrogen/air, argon/water steam, depending on the cell and operation mode, is controlled by a mass flow system.

To perform the characterisation in full cells, some important additions need to be done. First, a power source, load and a potentiostat/galvanostat to measure the I-V curves. In the second place, a steam generator and heated gas flow lines are incorporated, which are crucial in SOEC mode to introduce vaporised water and avoid its condensation. Another key aspect here is the inclusion of a seal, to ensure gas tightness and avoid the mixture of pure hydrogen and oxygen, circulating in the inner and outer chambers of the ProboStat, respectively. In this case, Ceramabond™ ceramic seal from Aremco (Spain) was used to separate the atmospheres. Finally, the electrochemical measurements (both I-V curves and EIS) were acquired using a PARSTAT® 2273 from PAR Instruments (Ametek Inc., USA).

Figure 2.7a shows the experimental setup mentioned above when already mounted inside the furnace, while Figure 2.7b displays a scheme of the system. To ensure a proper current collection a thin gold (oxygen electrode) or nickel paste (fuel electrode) layer is painted on top of the electrodes and the sample is positioned inside the ProboStat in between two metallic meshes. The meshes were made of gold for symmetrical cells, and of gold (oxygen electrode) and nickel (fuel electrode) in the full-cell configuration. The Ceramabond™ sealing and gas supply tubes are also represented. After the sample is correctly assembled,

the ProboStat® is set inside the furnace and the gas supply is connected. In addition, the steam is produced by the steam generator at 150-160 ºC and conducted through the heated lines. A heating wire and isolating fabric are used to cover the exposed parts amidst the gas entry and the furnace to avoid water condensation.

The electrochemical measurements were controlled using IonX in-house software developed at IREC (Novocontrol and I-V curves) and PAR Instruments Power Suite (PARSTAT).

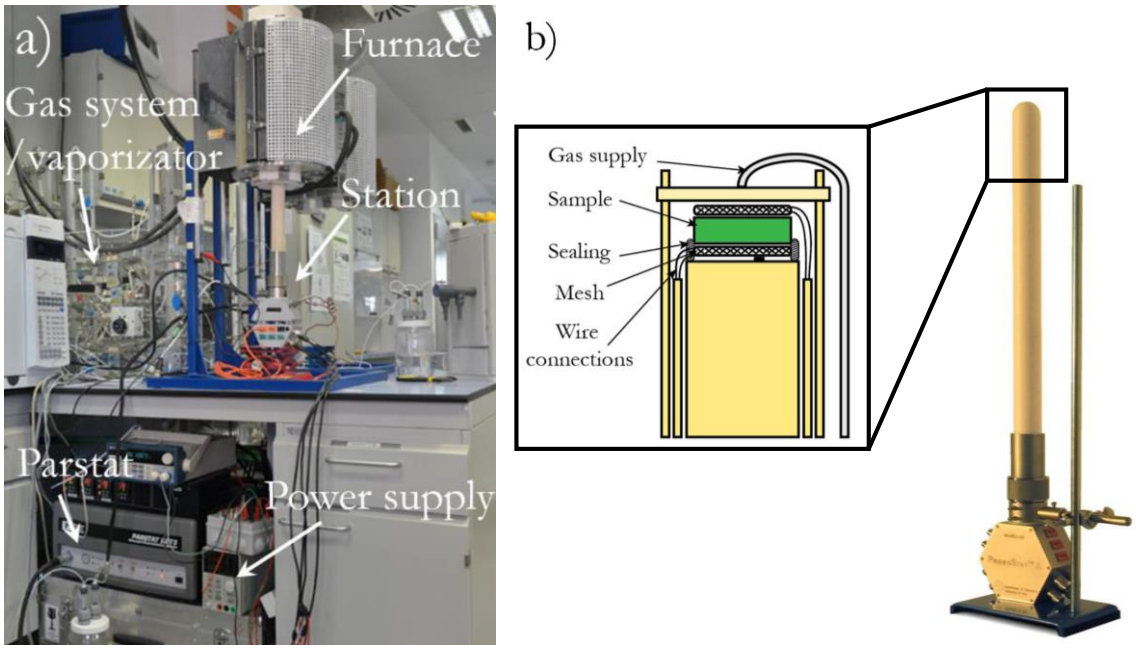

Figure 2.7. Experimental setup for electrochemical measurements fully assembled (a) and ProboStat internal scheme (b). Extracted from [35,88].

2.4.1.2.Electrochemical Impedance Spectroscopy (EIS)

As mentioned in the introduction, EIS is a very important technique used for the electrochemical characterisation of new materials and full operating devices. It was widely used in this thesis to characterise the electrodes prepared and the full-cell performance. The measurements were conducted in potentiostatic mode from 10 mHz to 1MHz and 50 mV amplitude (AC) over OCV; the operation temperature was between 850 and 500 ºC (50 ºC step) and an air or synthetic air atmosphere (50 mL/min) was used. ZView software (version 3.2, Southern Pines, USA) was used to evaluate the obtained impedance spectra.

2.4.1.3.Galvanostatic and Potentiostatic modes for I-V curves

The OCV of the cell and the I-V curves of the electrochemical cells in both SOFC and SOEC modes under different operating conditions were registered using a potentiostat/galvanostat PARSTAT 2273 from PAR. The measurements were performed in galvanostatic mode using a 50 mA amplitude and stopping when a voltage ~0.6 V (SOFC) or ~1.2 V (SOEC) was reached. The selected temperature range was between 600 and 800 ºC. The fuel side was supplied with a hydrogen flow that varied from 50 to 77 mL/min (SOFC) and a steam flow of 1900 mg/h (SOEC). An air flow between 50 and 192 mL/min was delivered to the oxygen electrode side. The specific conditions for each set of measurements are detailed in the results section presented in Chapter 3.

2.4.2. Structural and microstructural characterisation

2.4.2.1.X-ray Powder Diffraction (XRD)

XRD measurements were performed over the prepared samples both at Facultad de Química (CADifRaX) and IREC. The equipment used in the former is a Rigaku ULTIMA IV diffractometer of 285 mm radius in the Bragg-Brentano geometry, with CuK_α sealed-tube radiation (λ=1.5418 Å) operating at 40 kV and 30 mA. A diffracted-beam curved Ge monochromator and NaI scintillation detector were used for intensity recording. In the latter, the instrument is a Bruker D8 Advance diffractometer of 280 mm radius also in the Bragg-Brentano geometry and with CuK_α sealed-tube radiation (λ=1.5418 Å) operating at 40 kV and 40 mA. A Lynxeye 1D detector was used for data collection.

The data used for confirmation of phase purity were collected at room temperature in the 2θ=10-70° range in 0.04° steps with 3 s/step while the patterns measured to perform the structural characterisation using the Rietveld method were collected in the 2θ=10-120° range in 0.02° steps with 10 s/step. The fit of the data by the Rietveld method was performed using the GSAS-II software suite [89].

2.4.2.2.Scanning Electron Microscopy (SEM)

In this thesis, SEM was routinely used to study topography and microstructure of the powders obtained and the cross-sections of both symmetrical and full cells after testing. Digital micrographs were acquired in the energy range of 1.5-20 kV in a Zeiss Auriga microscope (Germany) using SE2, InLens (SE detector), and BSE detector.

Chapter 3

-RESULTS AND DISCUSSION-

3. RESULTS AND DISCUSSION

The aim of this chapter is to discuss the results obtained in all the steps of the experimental work, from the synthesis of the materials to the characterisation of full electrochemical devices.

3.1. Synthesis of LSFCu-CeO_2 composites

In this section, the synthesis process used to obtain the LSFCu perovskite and LSFCu-CeO2 x% (x= 5, 10, 20, 50), and the resulting materials' characterisation through XRD and electron microscopy are presented.

As mentioned in the previous chapters, the selected auto-combustion method is a modification of Pechini's original route to prepare alkaline-earth titanates. In this case, the chosen chelating agent (and organic fuel) is EDTA, instead of citric acid, which is mixed with ammonium nitrate (combustion promoter). The ratio used between them is 1:3 EDTA:NH_4NO_3 in moles.

The materials obtained directly from the synthesis are sponge-like dark brown powders (Figure 3.1) and consist of a low-crystallinity phase of the desired compounds and additional amorphous metal oxides. They were ground and calcined in air at 850 ºC for 6 h to obtain the final samples.

Figure 3.1. Example of the resulting powders obtained through the auto-combustion synthesis before and after grinding.

Figure 3.2 shows the diffraction patterns for all the calcined materials and the difference between the as-prepared sample and the calcined one for the LSFCu-CeO_2 20 composite where the poor crystallinity and presence of amorphous phases are depicted. The XRD data were modelled using the Rietveld method to obtain relevant structural parameters and confirm the composition of the samples as shown in Figure 3.3 for LSFCu, LSFCu-CeO_2 10 and 20.

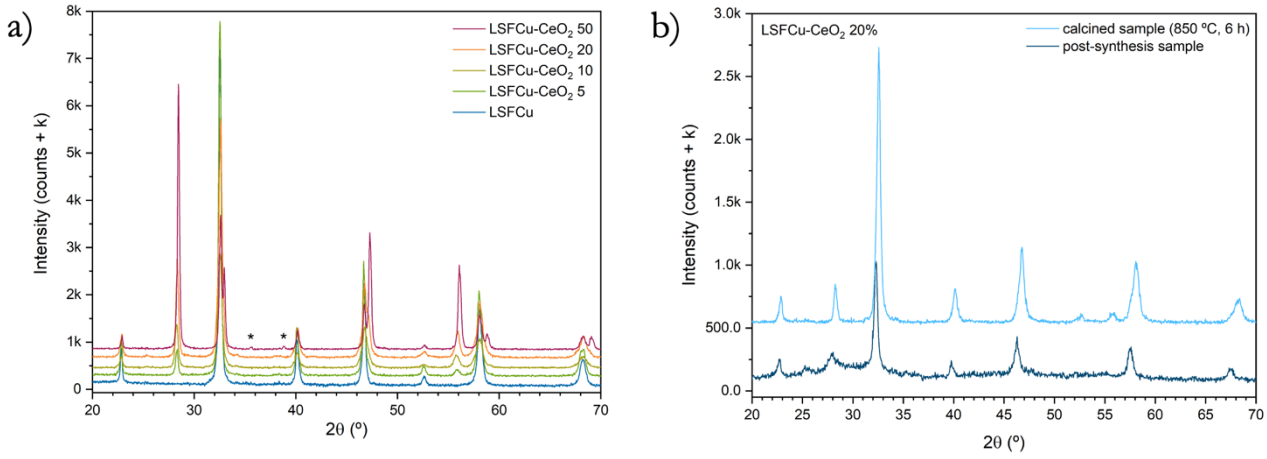

Figure 3.2. XRD patterns of (**a**) the final samples (the asterisks indicate the peaks corresponding to CuO impurity) and (**b**) the as-prepared and calcined sample corresponding to the 20% composite.

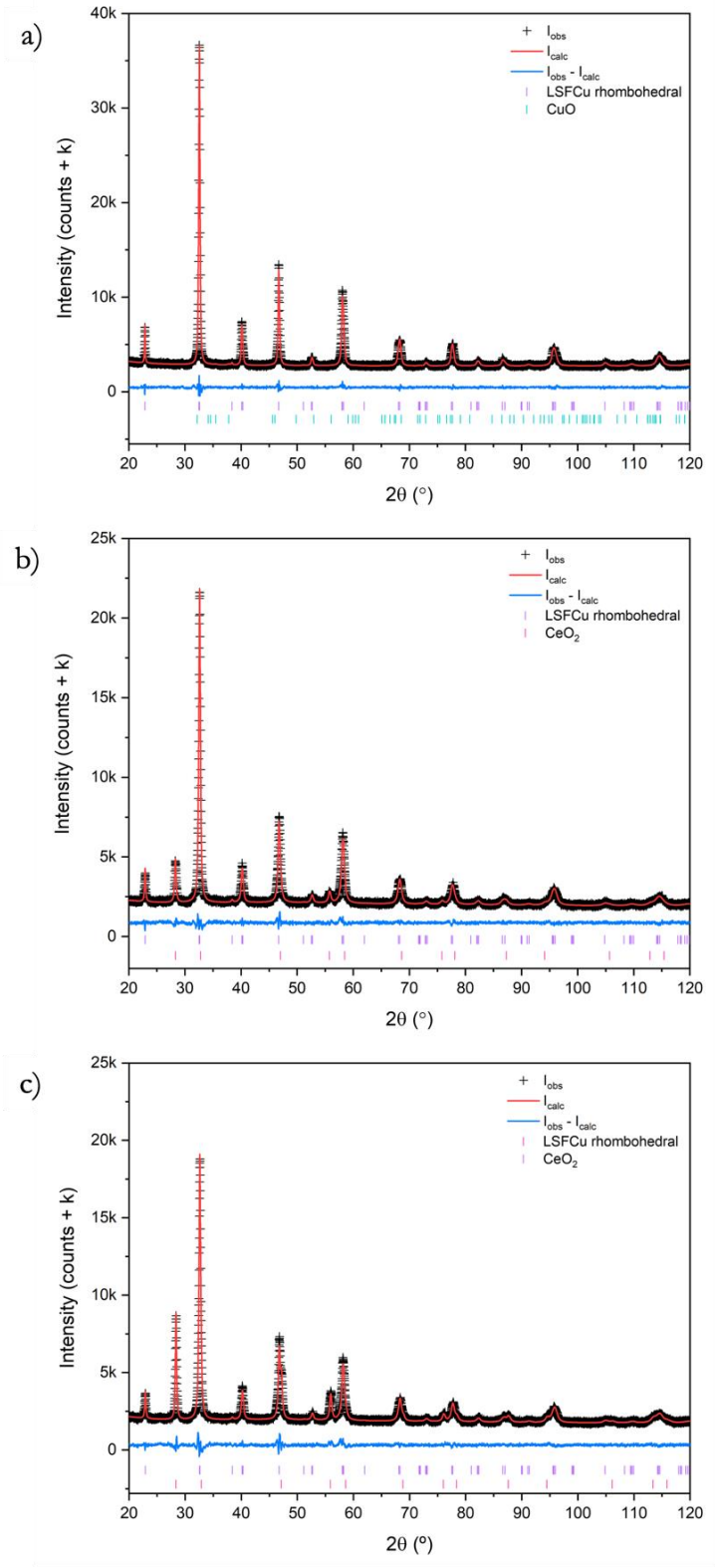

Figure 3.3. Rietveld fits of the (**a**) LSFCu, (**b**) LSFCu-CeO_2 10 and (**c**) LSFCu-CeO_2 20 samples after the thermal processing.

Table 3.1. Rietveld fit results of the structural parameters obtained for the LSFCu and CeO_2 phases (when corresponding) in the LSFCu sample and the LSFCu-CeO_2 10 and 20 composites.

Parameter	***LSFCu***		***LSFCu-CeO₂ 10***		***LSFCu-CeO₂ 20***	
	LSFCu	CeO_2	LSFCu	CeO_2	LSFCu	CeO_2
Space group	$R\bar{3}c$	$Fm\bar{3}m$	$R\bar{3}c$	$Fm\bar{3}m$	$R\bar{3}c$	$Fm\bar{3}m$
a (Å)	5.5070 (2)	-	5.5100 (5)	5.4709 (6)	5.5063 (7)	5.4550 (2)
c (Å)	13.4255 (5)	-	13.4366 (10)	-	13.4385 (13)	-
Wt. fraction (%)	100	-	91.2	8.8	80.7	19.3
wRp (%)	2.272		2.811		3.208	

One of the questions that came up after the synthesis, is if the obtained material is a mixture of both phases, LSFCu and CeO_2, or if it existed cation interchange with the formation of secondary phases among the perovskite and the fluorite (due to La^{3+} and Ce^{3+} similar ionic radii). In this light, we were able to determine through the Rietveld method (fit results are shown in Table 3.1) that the only phases present in the final samples are LSFCu, lightly La-doped CeO_2 and a small amount of CuO phase (< 2 wt.%). The doping of La in CeO_2 could be assessed through the change in cell parameters of CeO_2. The a-axis length of pure CeO_2 is expected to be 5.41 Å, while the refined values are close to 5.47 Å, a difference much larger than the standard uncertainty of the literature and refined values respectively [90]. From this, we infer that the doping has probably occurred during synthesis and the observation of a small amount of CuO in the doped samples could be a consequence of a slight depletion of La in LSFCu. However, we can still confirm that the synthesis process was successful and allowed us to obtain composites with the expected structures and compositions. Due to the impossibility to quantify La-doping in CeO_2 with the available data we will continue describing the fluorite phase as CeO_2.

The particle's size and the homogeneous distribution of the desired phases throughout the material were corroborated using electron microscopy. The SEM micrographs acquired with different detectors for the LSFCu-CeO_2 10 and 50% composites are shown in Figure 3.4.

The left-hand images were acquired using an SE2 detector, which gives more details about the samples' topography. The micrographs in the centre of the figure were obtained employing an InLens detector (better resolution). Finally, the right-hand pictures were taken with a BSE detector (backscattered electrons) where the contrast between the dark LSFCu and bright CeO_2 grains is visible.

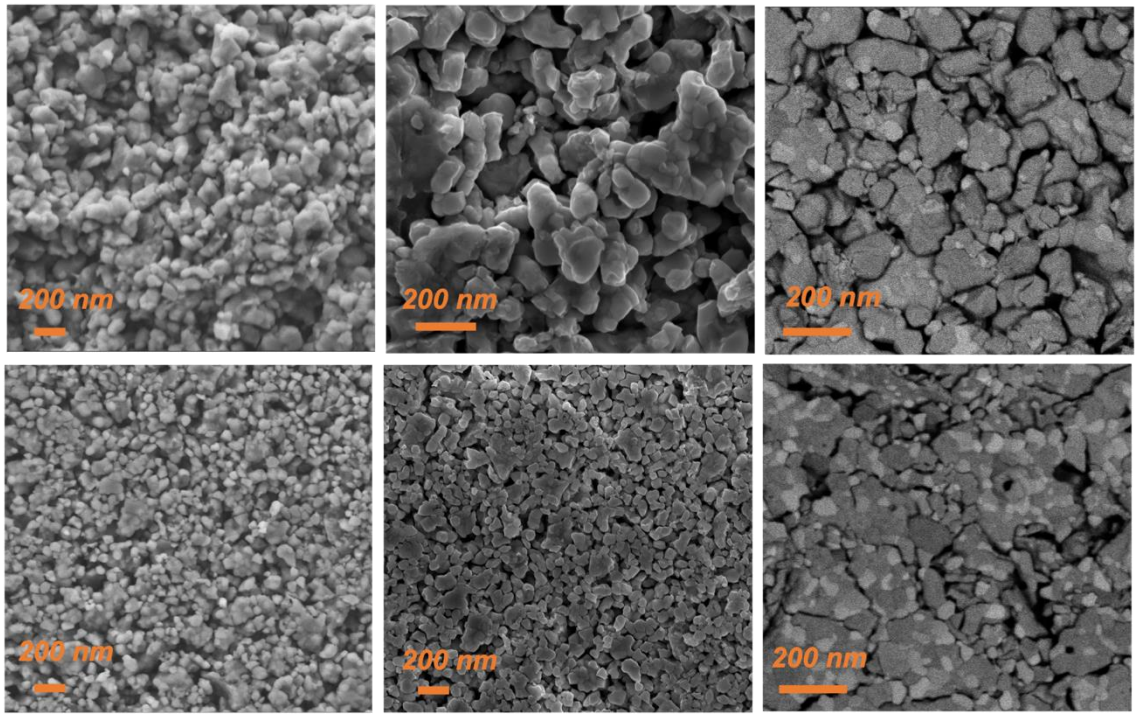

Figure 3.4. SEM micrographs of LSFCu-CeO_2 10 (**top**) and LSFCu-CeO_2 50 (**bottom**).

As seen in the pictures, the particle size of the sample is in the 10-150 nanometres range but there seem to be two particle size distributions (especially noticeable in the right-hand pictures), whitish and small particles and darker and larger ones. The brightness level in this technique is directly related to the average scattering density of the materials, which depends on sample density and elemental composition. The CeO_2 particles are most definitely the smaller ones, consistent with the preparation method and the calcination temperature.

To sum up, new LSFCu-CeO_2 composites were synthesised via a facile and rapid method in two steps. The particles of the composite in the powders obtained are homogeneously distributed and their sizes belong to the nanometric scale.

3.2. Chemical reactivity study with other cell components

Once the electrodes' materials are synthesised, the following critical test is the chemical reactivity study with the other cell components the electrode will be in contact with. In this case, with $Ce_{0.9}Gd_{0.1}O_{1.95}$ (GDC) which was used as an electrolyte in symmetrical cells and as a barrier layer in commercial Ni-YSZ anode-supported full cells. As already mentioned in Chapters 1 and 2, Sr-containing phases react with the Zr in YSZ and therefore, this reactivity test was not performed again.

For this purpose, and owing to the similarity between GDC and the slightly La-doped CeO_2 from the composites (which would prevent separating GDC and CeO_2 peaks in the XRD data), the reactivity measurements were conducted directly on the composite samples by firing them in air at a much higher temperature (1100 ºC) than the operation temperature. Given that the majority of chemical reactions (decomposition, formation of oxides, etc.) are

thermally activated, if there is no reaction at 1100 ºC we can assume they will not react at lower temperatures. The products of the thermal treatment were studied through powder XRD, and the collected data was modelled through the Rietveld method as shown in Table 3.2 and Figure 3.5 for pure LSFCu, and LSFCu-CeO_2 10 and 20 composites.

Table 3.2. Rietveld fit results of the structural parameters obtained for the LSFCu and CeO_2 phases (when present) in the LSFCu and LSFCu-CeO_2 10% and 20% composites.

Parameter	***LSFCu***		***LSFCu-CeO_2 10***		***LSFCu-CeO_2 20***	
	LSFCu	CeO_2	LSFCu	CeO_2	LSFCu	CeO_2
Space group	$R\bar{3}c$	$Fm\bar{3}m$	$R\bar{3}c$	$Fm\bar{3}m$	$R\bar{3}c$	$Fm\bar{3}m$
a (Å)	5.51268 (10)	-	5.51511 (12)	5.47686 (14)	5.51625 (12)	5.46238 (7)
c (Å)	13.41105 (15)	-	13.41464 (17)	-	13.41617 (18)	-
Wt. fraction (%)	100	-	88.2	10.3	77.8	20.4
wRp (%)	6.028		6.455		6.110	

None of the samples showed decomposition or reaction that would imply the observation of additional phases after the process. There is also no evidence of further La-Ce cation exchange between LSFCu and CeO_2 (besides the one that might be present already from the synthesis). The refined cell parameters of LSFCu in the three samples remain constant and comparable with that of calcined samples within 3 s.u. and the two refined cell parameters for CeO_2 are close to that from calcined samples and do not show a variation that may suggest a trend for La-doping [65]. Besides the desired phases, almost all of the samples presented the same small amounts of CuO (< 2 wt.%), which was already present after the thermal treatment at 850 ºC and thus cannot be related to this new processing conditions or reaction.

In summary, the LSFCu compound is chemically and thermally stable in presence of La-doped CeO_2 (and GDC) and therefore can be effectively used as an oxygen electrode in SOC devices.

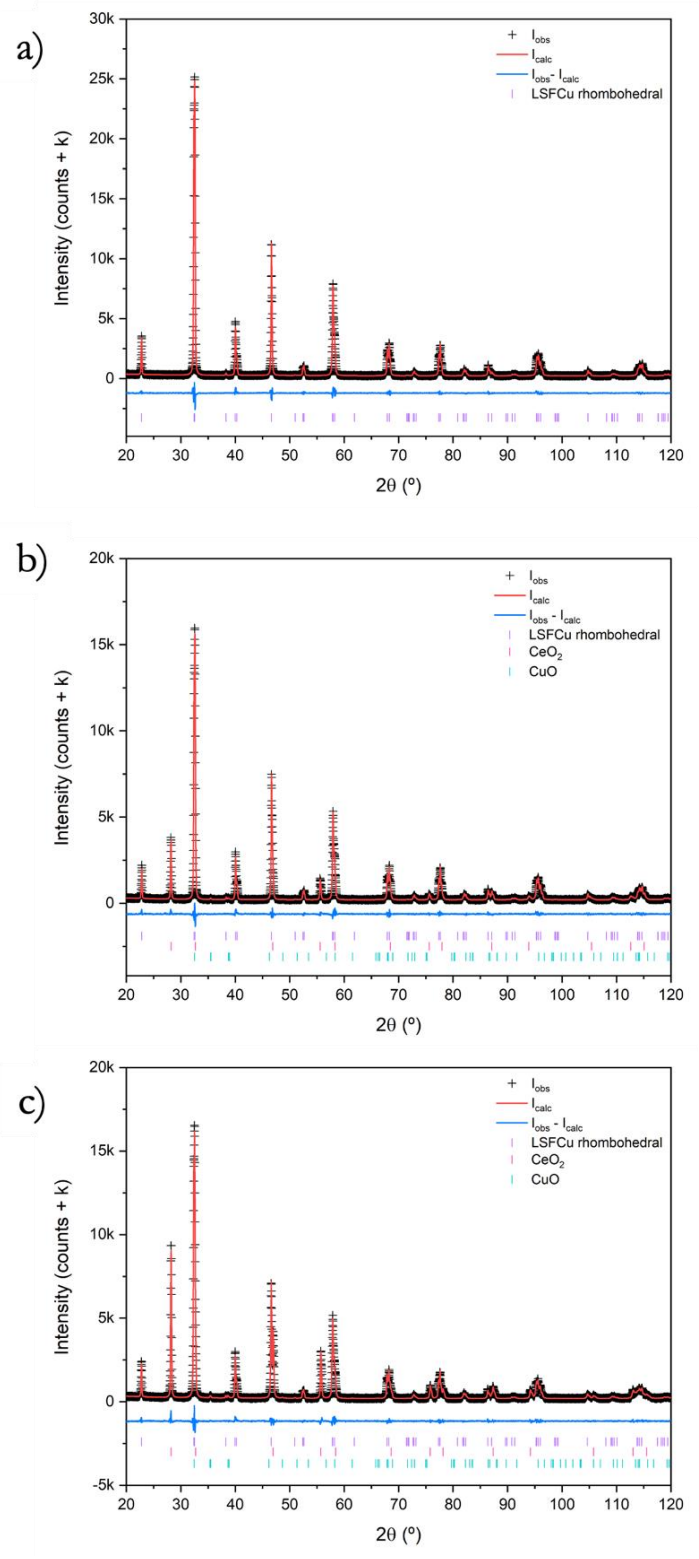

Figure 3.5. Rietveld refinement results for the LSFCu, LSFCu-CeO_2 10 and LSFCu-CeO_2 20 composites after a 12 h thermal treatment at 1100 ºC.

3.3. Optimisation of the electrode's manufacturing temperature

After the verification of the chemical and thermal compatibility of the electrode with the other cell components, the following key aspect is to ensure a correct attachment of the oxygen electrode to the electrolyte. If the adhesion between them is poor, there will be fewer points where the reaction can occur (lower TPB area), the conduction of oxygen dianions from the electrode to the electrolyte will be reduced and the difference in TEC combined with thermal cycling will quickly detach the components. As a consequence, the performance of the cell may be significantly reduced.

If the surface of the electrolyte is too smooth, as happens with commercial tapes and pellets after the sintering process, the attachment of the electrode requires higher sintering temperatures and may be less effective. To prevent this, an additional layer is deposited on top of the electrolyte to enhance the adhesion. This layer is commonly known as the roughness layer (RL) and is usually composed of the same material as the electrolyte, but deposited as loose powder sintered over the dense electrolyte. In this case, the RL was made of GDC commercial powder.

The optimisation of the electrode's attachment temperature was made by sintering three different GDC-supported symmetrical cells with the following configuration: LSFCu-CeO_2 20/GDC/LSFCu-CeO_2 20, at 900, 950 and 1000 ºC. The oxygen electrode impedance contribution was then tested by means of EIS to evaluate the different temperatures used and the obtained results were examined to select the best one. Note that the attachment of ceramic materials requires co-sintering of them in the contact surface. For this process to occur, at least one of the materials should show particle growth during the thermal treatment. This particle growth will harm the electrode's performance since an increase in particle size results

in a reduction of the active electrode surface, therefore, selecting the correct attachment temperature is a compromise between keeping the temperature low enough to prevent significant particle growth and ensuring a stable adhesion of the electrode and electrolyte material [62]. This was studied by our group for $Ba_{0.5}Sr_{0.5}Fe_{0.8}Cu_{0.2}O_3$-GDC electrode-electrolyte samples and applied to LSFCu and related materials [61], where it was found that the attachment temperature should be at least 50 ºC higher than the last calcination temperature of the electrode material. However, these findings might not be simply translated to LSFCu-CeO_2 composites because of the different particle sizes and thermal behaviour of LSFCu and CeO_2.

This test was first performed using GDC pellets, made in the laboratory as described in the experimental section in Chapter 2. Figure 3.6a shows the pellets after the sintering process (left) and after the application of the roughness layer (right), and Figure 3.6b shows the symmetrical cell after the sintering of the electrode, applied on both sides.

The performance of materials using EIS is done by inspection of the R_s and R_{pol} values extracted from the spectra. As mentioned in Chapter 1, R_s is a purely ohmic (electrolyte component) factor and R_{pol} is related to the processes occurring in the electrode. In general, as for every electrochemical process, lower resistance values will lead to higher performances due to fewer impediments in the way to achieving the desired reactions. As the active area of every material is different, the Z' and Z'' values of the impedance curve are normalised by the area of the electrode used and expressed in terms of $\Omega \cdot cm^2$.

The EIS spectra obtained for the oxygen electrode composite sintered at 950 ºC are shown in Figure 3.6c for the temperature range between 700 and 800 ºC. The top-left image shows big impedance arcs for all of the temperatures measured, which could not be attributed

to the electrode due to the frequency of the process(es) (~10^5-10^6 Hz). After studying the spectra in more detail, a small arc at the end of the big arcs was detected. The frequency of these arcs, observed for all the temperatures, corresponds to electrode-related processes (~10^{-1}-10^4 Hz). Thus, exists another process which is not related to the electrode which is interfering with the measurement of the desired spectra. The close-ups for each temperature showing the smaller arcs are exemplified for the composite sintered at 950 ºC in the remaining images of Figure 3.6c. This problem was also observed in the sample with the electrode sintered at 900 ºC, therefore, we decided not to measure the sample with T_{att}=1000 ºC and to change the electrolyte support to GDC commercial tapes.

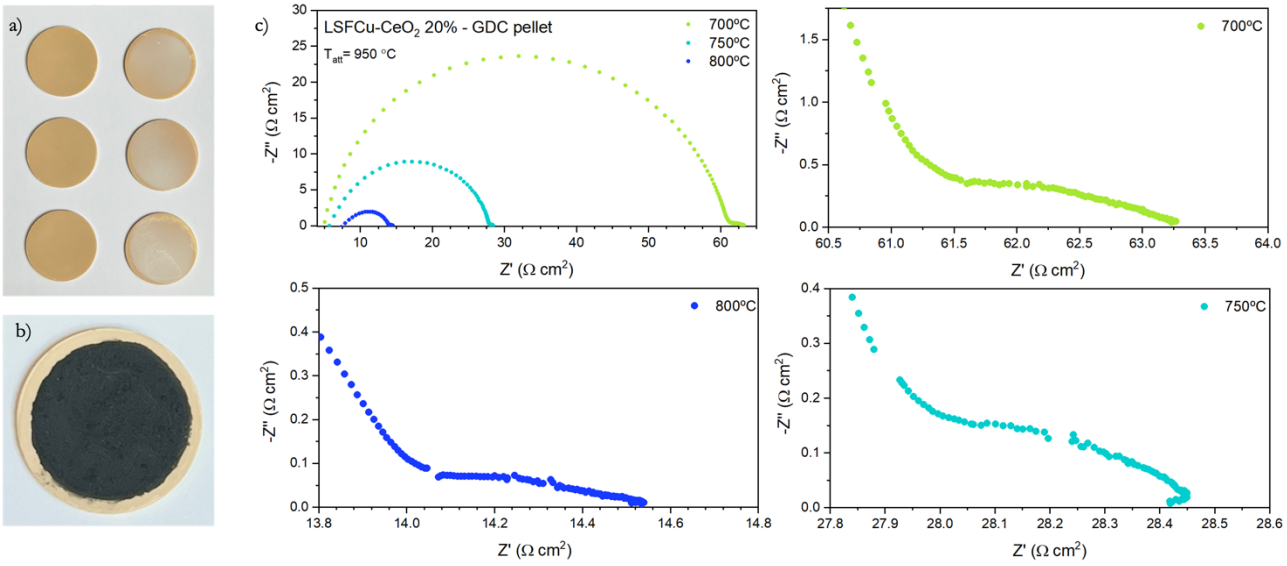

Figure 3.6. Pictures of the sintered GDC pellets before and after the application of the RL (**a**) and after the deposition of the electrode (**b**); and EIS spectra measured at different temperatures for the LSFCu-CeO_2 20 composite sintered at 950 ºC (**c**).

As a consequence, the determination of the attachment temperature of the electrode had to be performed again, this time was done using the same LSFCu-CeO_2 20 electrode but with GDC tapes as support. The EIS spectra obtained for the three different sintering temperatures

are shown in Figure 3.7 for the temperature range between 750 and 850 ºC (closest to operation temperature).

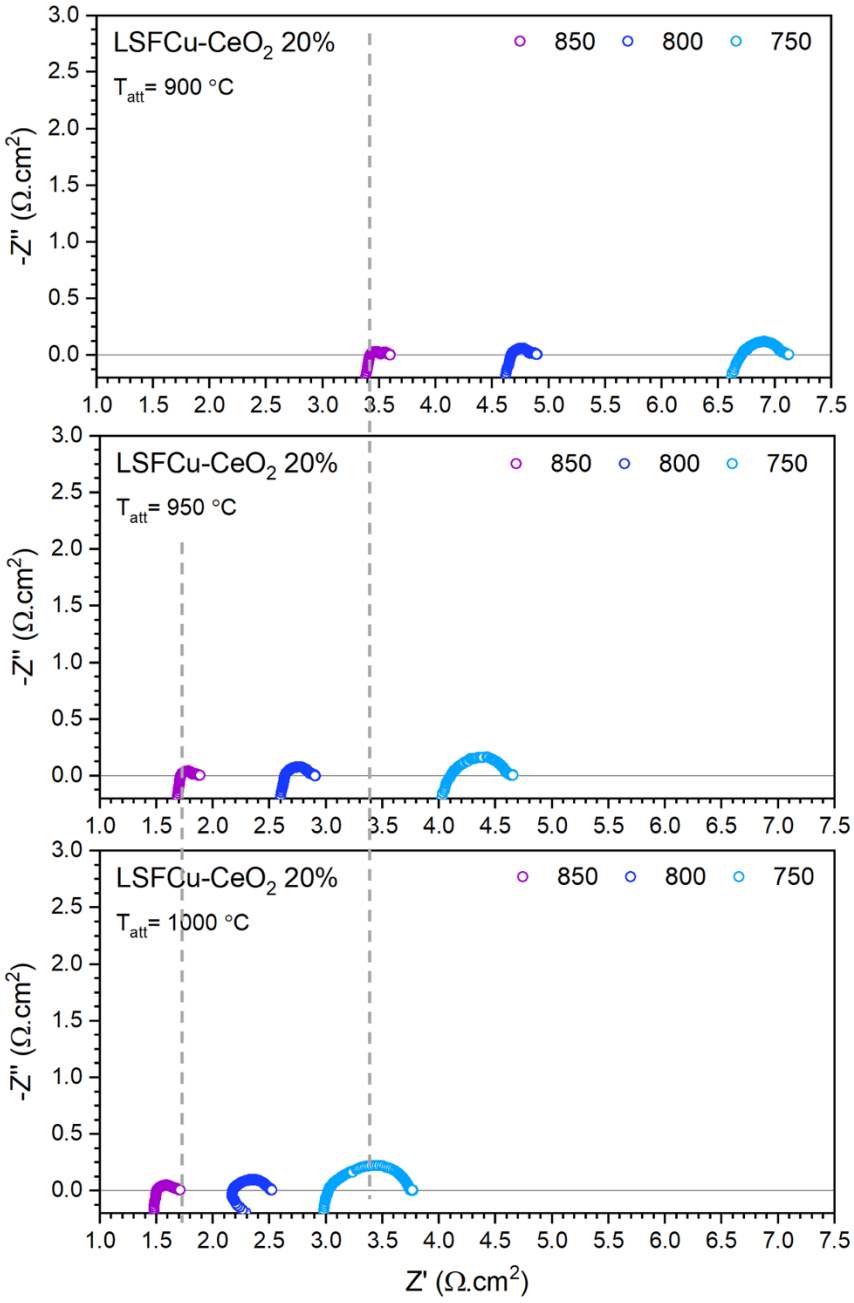

Figure 3.7. EIS spectra measured at different temperatures for the LSFCu-CeO_2 20 composite with three attachment temperatures.

The measurements in this range of temperature did not exhibit the big arc at higher frequencies, but the data at a lower temperature (700-500 ºC) seems to have the same problem. These findings will be discussed in the following section.

In Figure 3.7, we can notice that despite showing lower polarisation resistances, the electrode attached at 900 ºC exhibits higher serial resistance contribution (larger R_s) which is probably due to a poor attachment of the electrode. Among the other two temperatures, the lowest polarisation resistances were obtained for the electrode sintered at 950 ºC (although the R_s is slightly bigger than the one for the 1000 ºC sample). In this perspective, the attachment temperature that shows better electrode performance (lower R_{pol}) with the lowest ohmic resistance (R_s) is 950 ºC and was the one later used to sinter all the other composites.

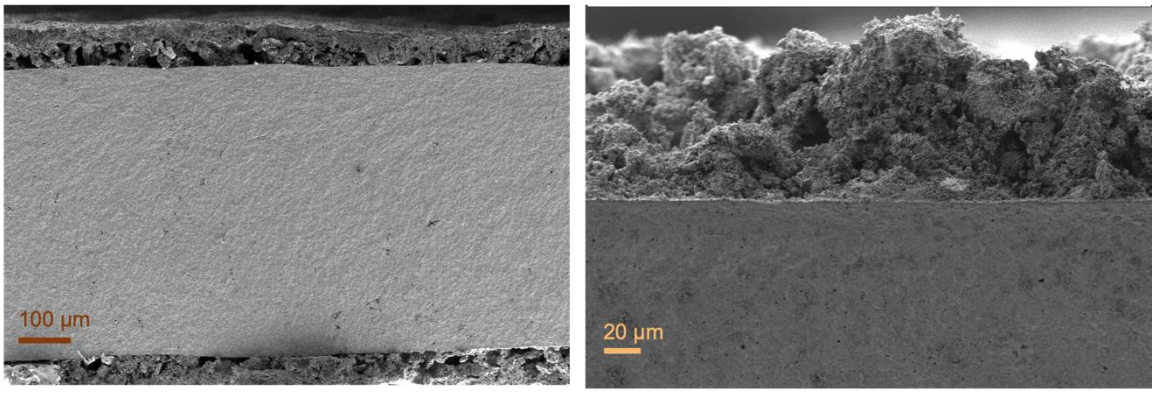

Figure 3.8. SEM micrographs of the cross-section of a symmetrical cell with a poorly-attached electrode (**left**) and a well-attached one (**right**). They were obtained after EIS measurements.

Figure 3.8 shows the micrographs of a poorly attached electrode (left, T_{att}= 900 ºC, taken before the optimisation) and a properly attached electrode (right, T_{att}= 950 ºC). Despite the normal holes that may appear while breaking the cell to observe its cross-section, the ones shown in the left-hand picture do not seem to be originated in this way since all of them are located next to the electrolyte layer (dense, light grey coloured). On the other hand, the right-

handed picture shows some imperfections on top and horizontal displacements but looks well-attached and even the thin RL (2-5 μm) can be appreciated (the whitish layer between the dense electrolyte and the porous electrode).

3.4. Oxygen electrodes' electrochemical performance characterisation

After the attachment temperature was set, symmetrical cells with the other oxygen electrodes synthesised were produced on commercial GDC tapes as described in the experimental chapter.

Figure 3.9a shows one of the symmetrical cells prepared on GDC tapes, where the GDC roughness layer can be also perceived (clearer ring around the electrode), while Figure 3.9b shows the painted area of one of the electrodes. SEM micrographs of a symmetrical cell are shown in Figures 3.9c and 3.9d, where the different components of the cells can be differentiated: a zone with a dense material which corresponds to the electrolyte, next to a thin semi-dense layer that can be identified as the GDC roughness layer, and then, the porous electrode.

The electrode's performance towards the ORR was evaluated by performing EIS measurements under OCV conditions on the symmetrical cells prepared. The data collected in the 850-600 ºC range are shown in Nyquist and Bode's plots for the LSFCu, LSFCu-CeO_2 10 and LSFCu-CeO_2 20 samples in Figures 3.10, 3.11 and 3.12. Each figure shows the Nyquist plots for all the temperatures in (**a**), a zoomed image of the high-temperature (HT) range (700-850 ºC) plots in (**b**), and the Bode plots with an inset of the HT data in (**c**).

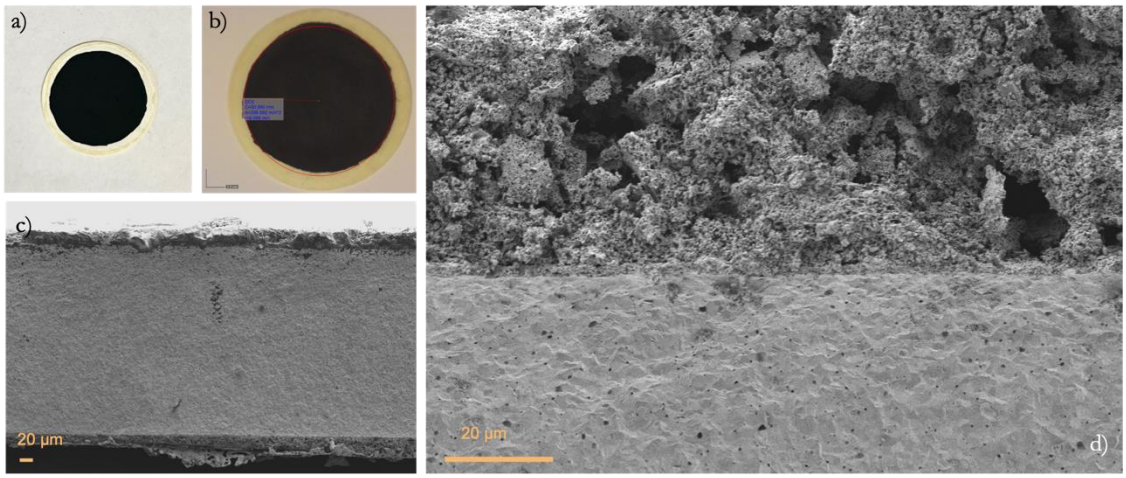

Figure 3.9. Top view of symmetrical cells (**a**, **b**) and SEM micrographs of the cross-section of a symmetrical cell where the cell components can be observed (**c**, **d**).

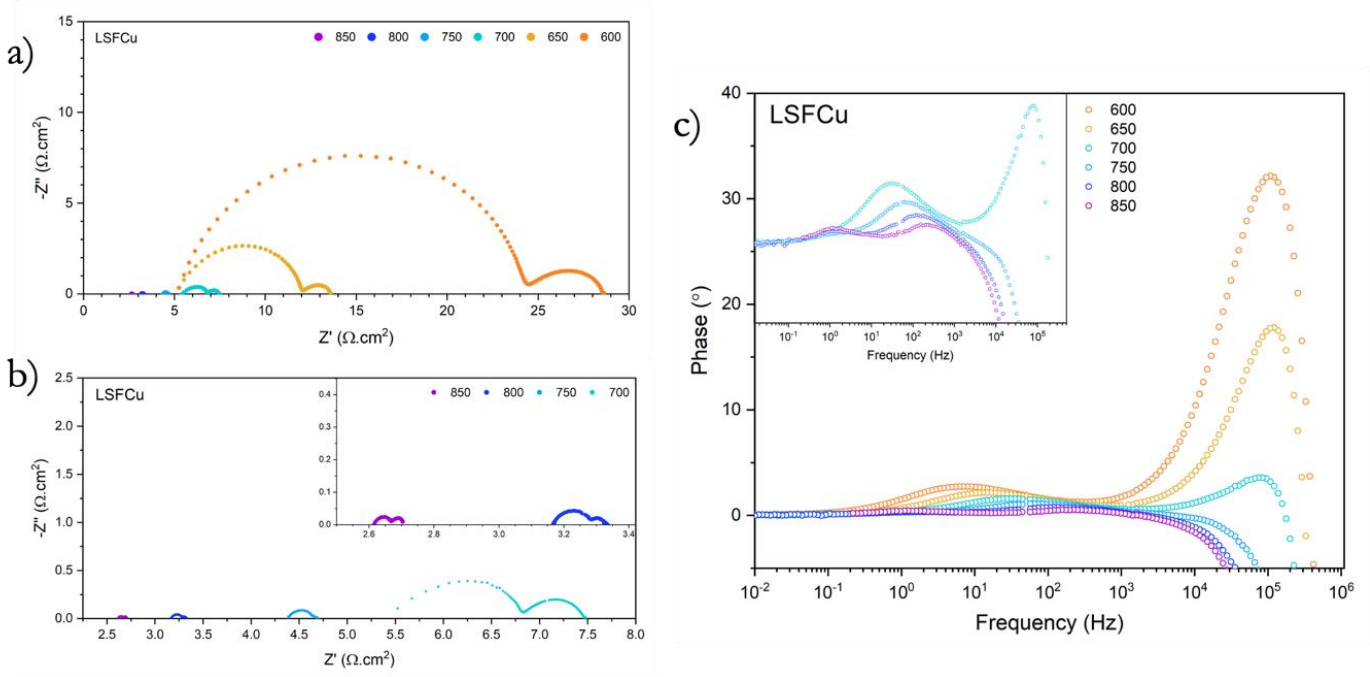

Figure 3.10. Nyquist (**a**, **b**) and Bode (**c**) plots for the LSFCu sample.

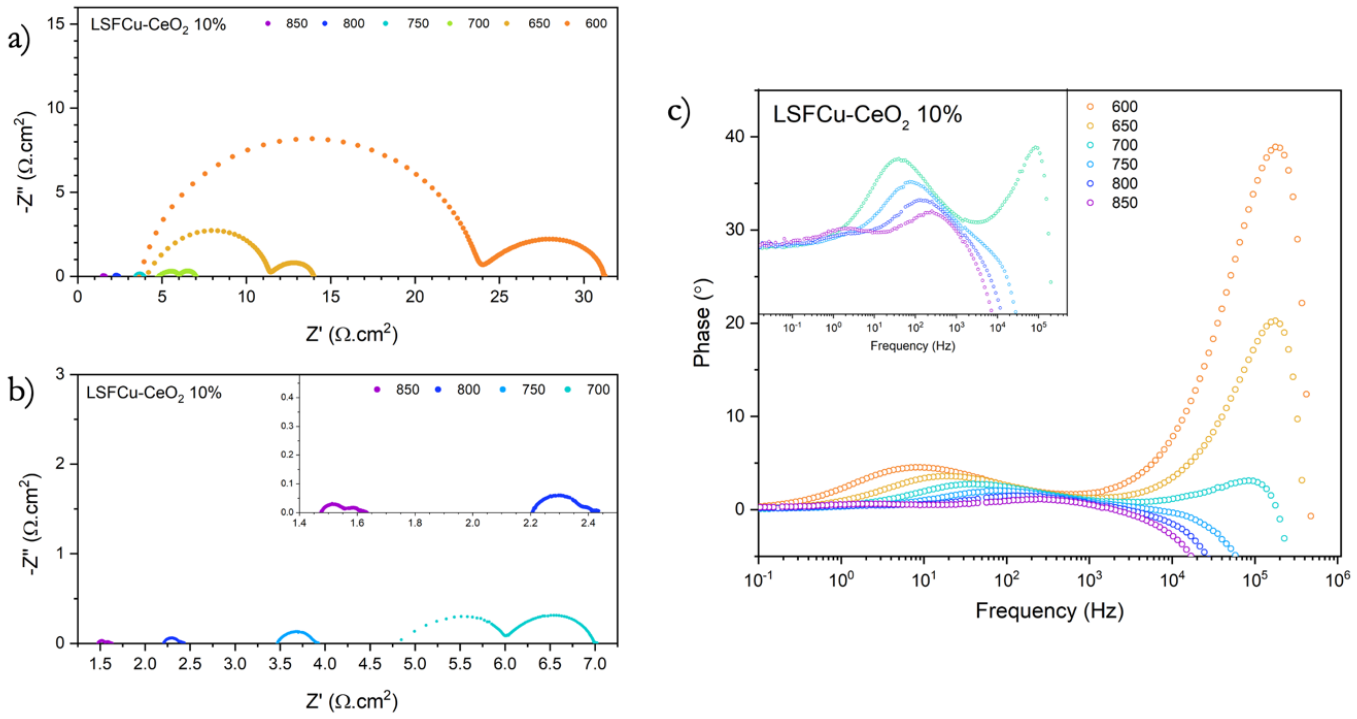

Figure 3.11. Nyquist (**a**, **b**) and Bode (**c**) plots for the LSFCu-CeO_2 10 sample.

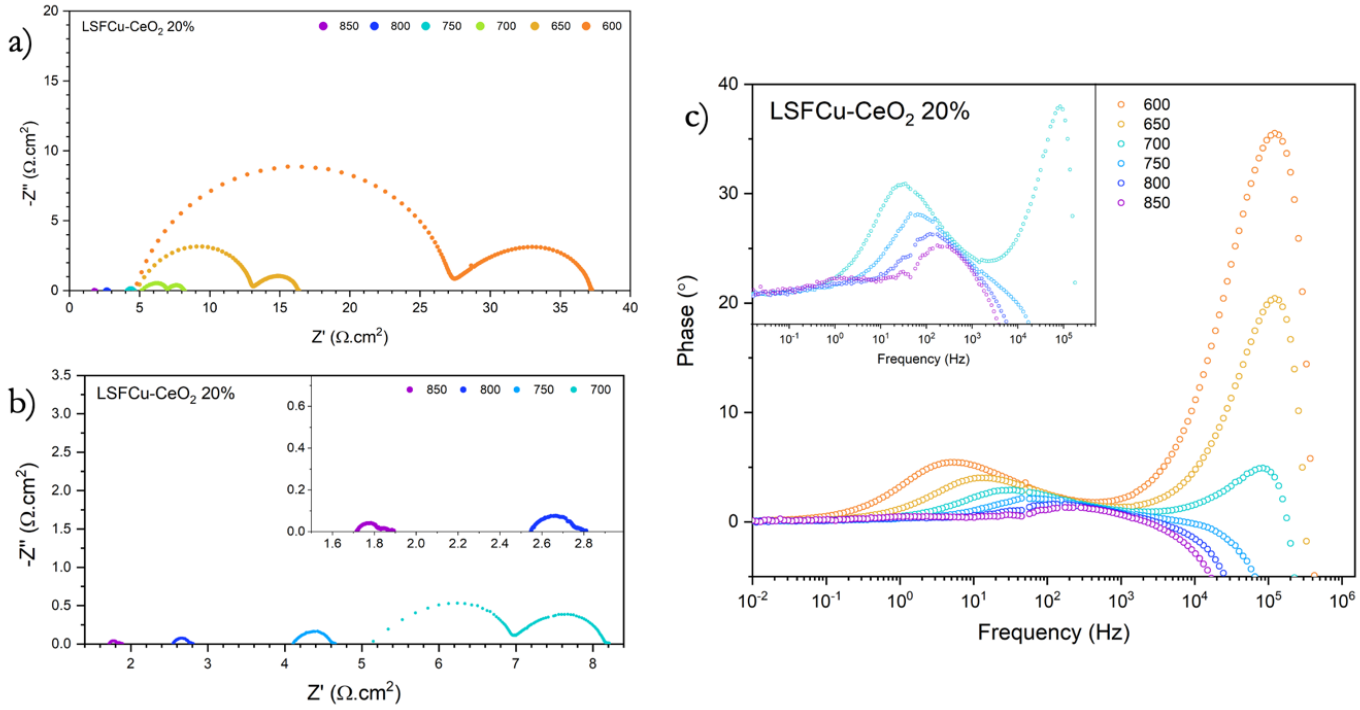

Figure 3.12. Nyquist (**a**, **b**) and Bode (**c**) plots for the LSFCu-CeO_2 20 sample.

The performance of a material is usually expressed through its Area Specific Resistance ($ASR = \frac{R_{pol}}{2} \times Area$), which is obtained by normalising the R_{pol} values obtained from the fitting of data shown in the Nyquist plot with the area of the electrode. Each spectrum was fitted employing the ZView software, using the following equivalent circuit: -(L)-(R_s)-(R_1||CPE_1)-(R_2||CPE_2). This circuit consists of an inductance (L), a serial resistance (R_s) and two ZARC elements (R in parallel to a CPE), and was the simplest circuit that allowed to fit the experimental data and showed correlation with the processes that occur in the electrode.

The observed inductance L of the circuit is due to the setup, while the R_s provide information about the ohmic contributions, which are mainly attributed to the oxide anion mobility through the electrolyte, but also include the resistance associated with the electrode-electrolyte interfaces, current collectors and electric contacts. The ZARC elements are standard electrical circuit elements associated with the polarisation contribution of different electrochemical and physical processes taking place in the electrode and electrode/electrolyte interfaces (gas diffusion, grain boundary resistance, and electrochemical reactions). [33,35]

Firstly, the ohmic conductivity of the electrolyte was examined through serial resistance, R_s. As depicted in the Nyquist and Bode plots, a big arc before the one corresponding to the electrode appears at 700 ºC ($f \approx 10^5$ Hz, clearly seen in Bode plots of Figures 3.10, 3.11 and 3.12). The origin of this arc is not clear to us. It could be related to a process occurring in the electrolyte, probably due to a predominantly capacitive process arising in the electrolyte-RL or RL-electrode interface. The EIS measurement of a blank sample composed of the GDC electrolyte tape with RL and gold paste allowed us to verify that the effect is not related to the electrode. The Bode plot of the blank sample is shown in Figure 3.13, and the process

with the high frequency that appeared in the other samples can be observed from 750 ºC. Therefore, we decided to omit the first arc for the fit of the EIS spectra.

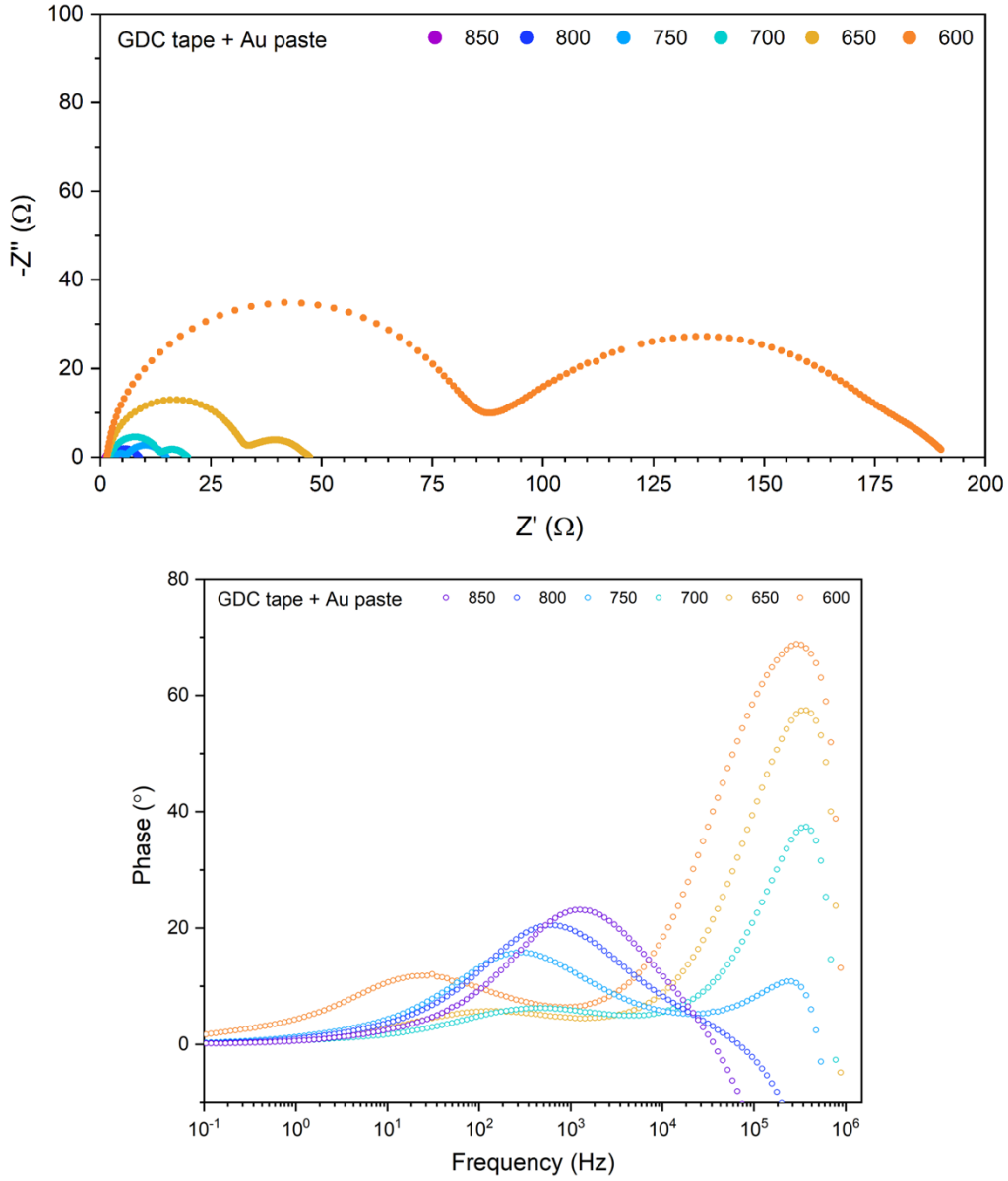

Figure 3.13. Nyquist and Bode plots for the blank sample (GDC tape + RL +Au paste).

Figure 3.14 shows the spectra and fits performed on the three studied materials at three different temperatures (850 ºC (top), 800 ºC (middle) and 750 ºC (bottom), respectively) and the circuit used as a model (as an inset in all of them). The values of R_s, R_{pol} (with $R_{pol}=R_1+R_2$), ASR_{pol} and ohmic conductivity are summarised in Table 3.3.

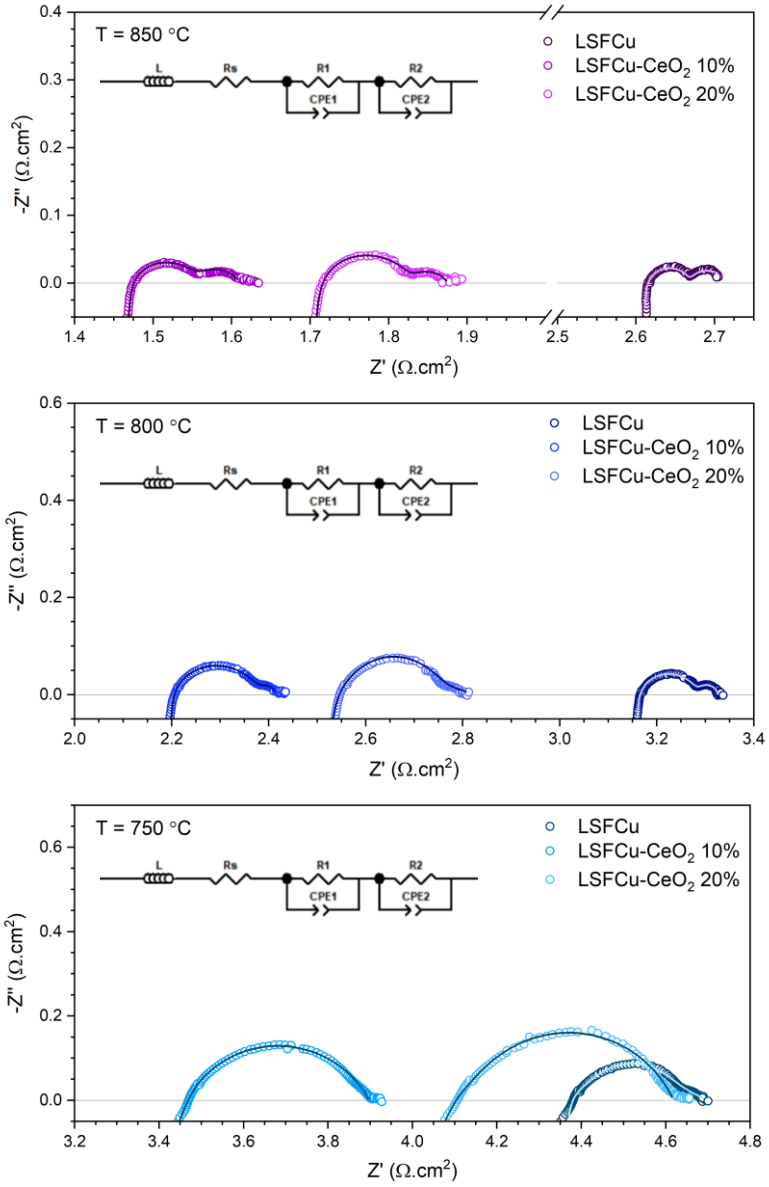

Figure 3.14. Nyquist plots with the EIS spectra and EC model fit for the three samples.

Table 3.3. EIS spectra fit results for the three samples shown in the figure at the left.

LSFCu				
A_{teo}= 2.2574 cm²				
T (ºC)	Rs (Ω)	R_{pol} (Ω)	ASR (Ω.cm²)	σ (S.cm⁻¹)
850	1.147	0.04574	0.05163	7.72×10^{-3}
800	1.388	0.07468	0.08429	6.38×10^{-3}
750	1.907	0.15727	0.17751	4.65×10^{-3}
700	2.96	0.32365	0.36530	2.99×10^{-3}
650	5.158	0.82581	0.93209	1.72×10^{-3}
600	10.51	2.0579	2.3238	0.84×10^{-3}

LSFCu-CeO₂ 10 %				
A_{teo}= 2.0936 cm²				
T (ºC)	Rs (Ω)	R_{pol} (Ω)	ASR (Ω.cm²)	σ (S.cm⁻¹)
850	0.7001	0.06911	0.07234	12.65×10^{-3}
800	1.048	0.10554	0.11048	8.45×10^{-3}
750	1.602	0.25953	0.27167	5.53×10^{-3}
700	2.845	0.49497	0.51813	3.11×10^{-3}
650	5.344	1.3450	1.4079	1.66×10^{-3}
600	11.21	3.7310	3.9056	0.79×10^{-3}

LSFCu-CeO₂ 20 %				
A_{teo}= 2.2540 cm²				
T (ºC)	Rs (Ω)	R_{pol} (Ω)	ASR (Ω.cm²)	σ (S.cm⁻¹)
850	0.7558	0.07618	0.08585	11.72×10^{-3}
800	1.133	0.1619	0.18244	7.82×10^{-3}
750	1.825	0.2578	0.29054	4.85×10^{-3}
700	3.051	0.5777	0.65105	2.90×10^{-3}
650	5.706	1.5301	1.7244	1.55×10^{-3}
600	11.92	4.6060	5.1910	0.74×10^{-3}

Figure 3.15 exhibits the Arrhenius plots of the ohmic conductivity (obtained from R_s) vs temperature (expressed in log scale vs 1000/T), in the 600-850 ºC range for the three samples measured, as well as a reference curve extracted from [91], and their corresponding apparent activation energies. The linearity of the obtained curves, suggests that the omission of the first impedance arc in the fit was appropriate and that the electrode's serial resistance was closer to the one of the second arc. However, both the lower conductivity and larger activation energy values (when compared to the reference), suggest that the electrolyte used

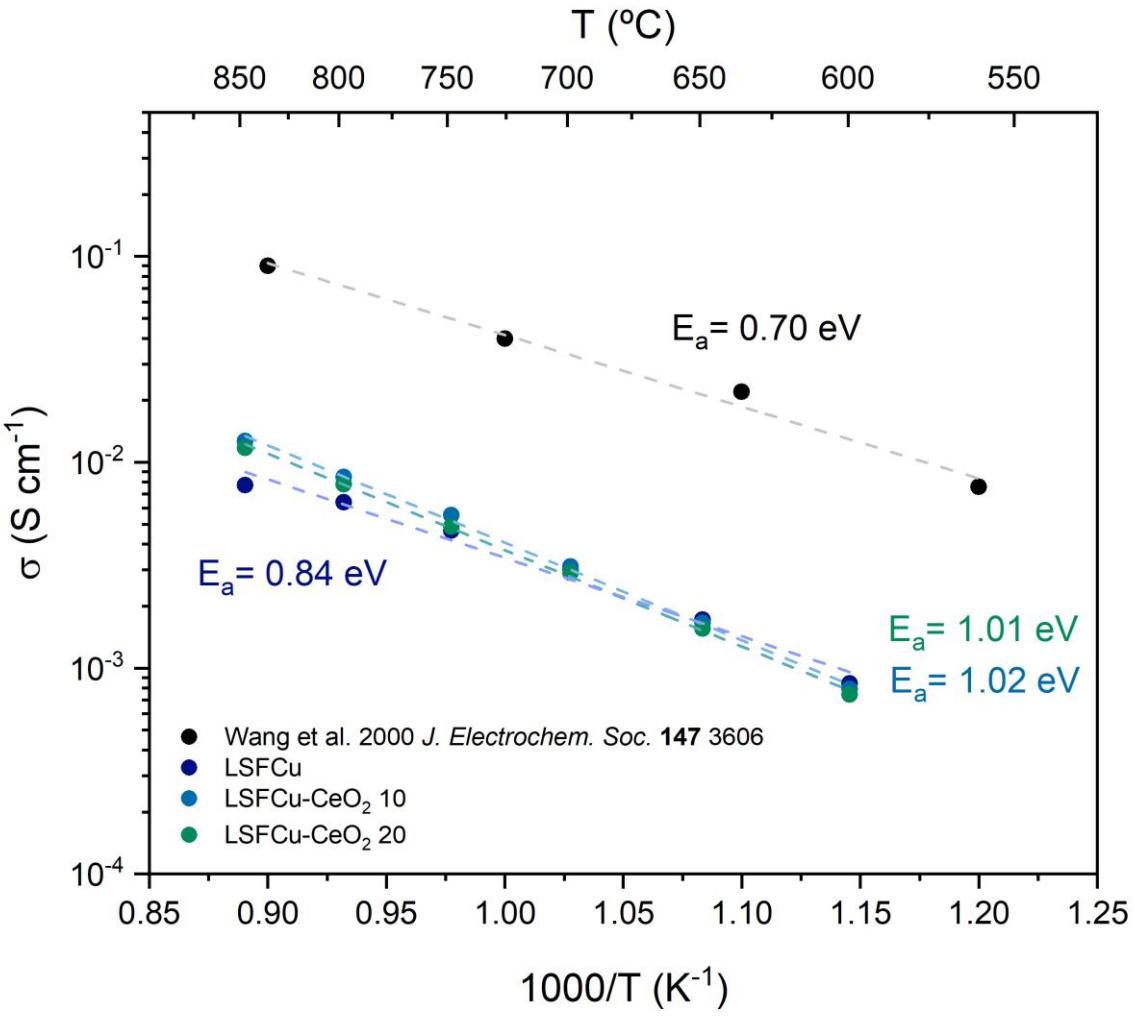

Figure 3.15. Arrhenius plots of the ionic conductivity of the tested materials.

is not a proper ionic conductor (might be owed to the low density of the tape, for example) and, consequently, not the best material to be used as an electrolyte.

After this, the polarisation resistance of the EIS data was examined through the Arrhenius plots of the ASR_{pol} (in log scale vs. 1000/T), which are depicted in Figure 3.16. In general, it can be said that the R_{pol} values obtained for all the materials are low and comparable to those reported in the literature for Co and Cu-based materials [6,57,59,76,92].

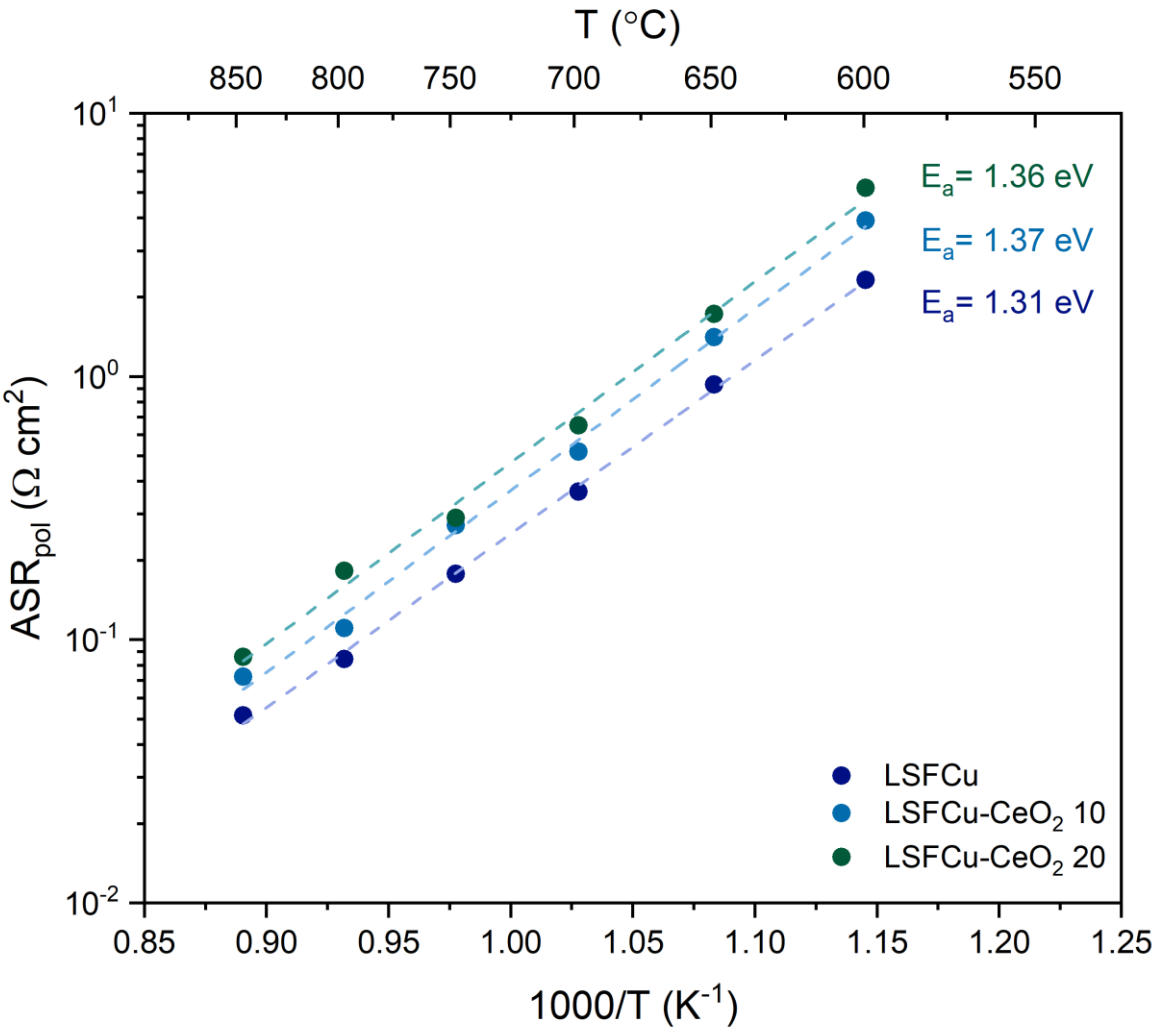

Figure 3.16. Arrhenius plots for LSFCu and the LSFCu-CeO_2 10 and 20% composites.

The linear fit of the $lnASR_{pol}$ vs. 1000/T data enabled the calculation of the apparent activation energies (E_a) associated with the processes happening in the electrode during operation from the slope of the curve. The high quality of the fittings (R^2= 0.998, 0.996 and 0.995 for the LSFCu, LSFCu-CeO_2 10 and LSFCu-CeO_2 20 samples, respectively), suggests that the ORR limiting process is the same in the whole studied temperature range, and, accordingly to these processes, is thermally activated. The activation energies are in the range of 1.3-1.4 eV, which are typical values for MIECs used as oxygen electrodes, and the difference between them is not significant. Therefore, all of them could be considered good catalysts for the ORR. That being said, the LSFCu sample is the one that exhibits the lowest activation energy value and is consequently, the best-performing material among the tested samples.

3.5. Evaluation of the electrochemical performance of the LSFCu and LSFCu-CeO_2 composites as oxygen electrodes of a SOC device

After the electrochemical characterisation of the materials was done, they were evaluated as oxygen electrodes of a full SOC device. Taking into account the results presented in the previous section regarding the poor performance of the electrolyte, we decided to use the state-of-the-art YSZ electrolyte instead of GDC for the full cell characterisation.

As mentioned before, the oxygen electrode material was painted on top of commercial fuel electrode-supported half-cells fabricated with state-of-the-art techniques and materials. The cells consist of a relatively thick NiO-YSZ fuel electrode support (~250 μm) with a very thin YSZ electrolyte layer on top (8-10 μm) (all of the data was provided by the manufacturer). The prepared half-cells before and after the electrode-sintering process are

depicted in Figure 3.17. Here, the green zone corresponds to the NiO-YSZ support and can be seen clearly from the top because of the narrow thickness of the electrolyte layer. If we move towards the centre of the cell (Figure 3.17a), a slim white ring appears between the green zone and the black oxygen electrode; this ring corresponds to a portion of the GDC barrier and roughness layers.

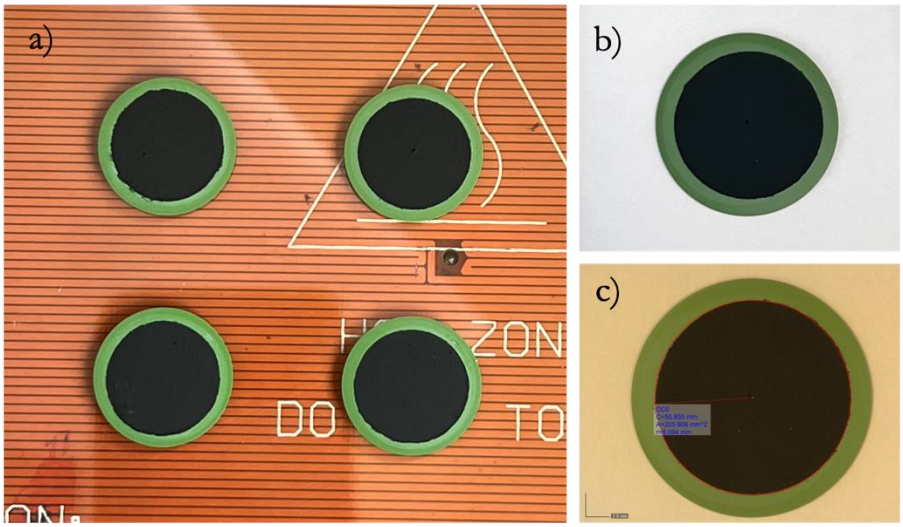

Figure 3.17. Full anode-supported cells with the painted LSFCu electrode before (**a**) and after the sintering process (**b**,**c**).

Three of the prepared cells containing the LSFCu, LSFCu-CeO_2 10 and LSFCu-CeO_2 20 oxygen electrodes (one each) were mounted in the ProboStat system and the inner and outer chambers were sealed with Ceramabond™ ceramic seal, as described in the Experimental section. Once the curing of the seal was finished, the NiO-YSZ layer was reduced to form Ni-YSZ active fuel electrode and the cell was characterised by means of polarisation curves. The results shown below correspond to the LSFCu and the 10% in CeO_2 composite samples because the test with the LSFCu-CeO_2 20 one did not reach the minimum OCV value to be measured. The post-mortem examination showed that the Ceramabond™

seal was broken (Figure 3.18), and therefore, a mix of H_2 and O_2 was taking place everywhere around the cell. Moreover, there were also some cracks in the cell, probably due to incorrect curing of the seal that caused a sudden shrinkage in the ceramic material, breaking it.

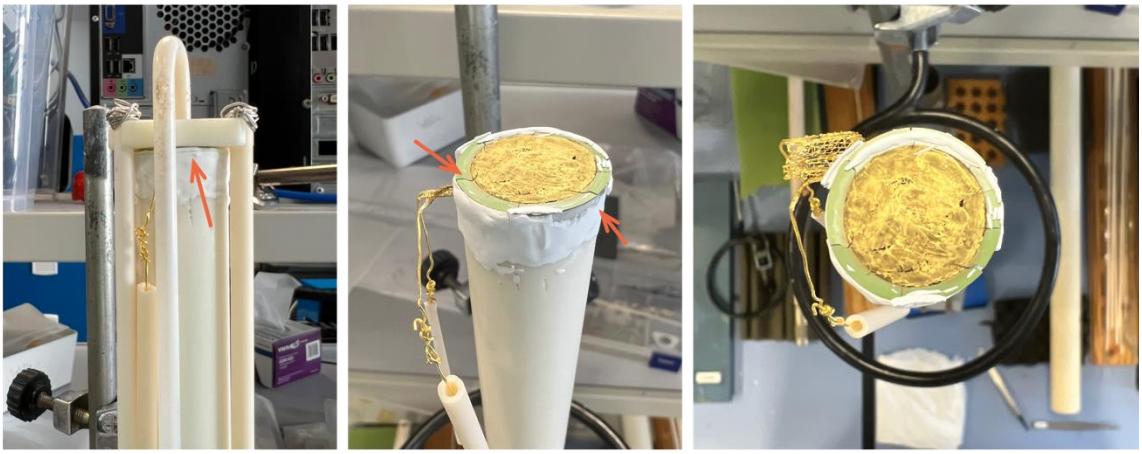

Figure 3.18. Examination of the mounted cell with LSFCu-CeO_2 20 electrode after the measurement.

Figure 3.19 shows the I-V curves obtained for the LSFCu sample in SOFC mode at different operation temperatures using a 1:2.5 ratio of H_2:air on the oxygen and fuel electrode side, respectively (H_2 flow ~ 22.2 mL/min/cm^2). The OCV value (~1.1 V) for the tested cell is consistent with the expected theoretical value and stable in time, which ensures the good quality of the seal despite not being perfectly gas-tight.

A power of 0.5 W.cm^{-2} was achieved at ~0.7 A.cm^{-2} current density. This value is comparable to the results obtained for LSFCu by Zhou et al. in 2009 but falls somehow short compared to modern cells containing state-of-the-art oxygen electrodes. However, these results could be improved since the curves presented in the figure above do not seem to have reached the maximum at the applied current densities.

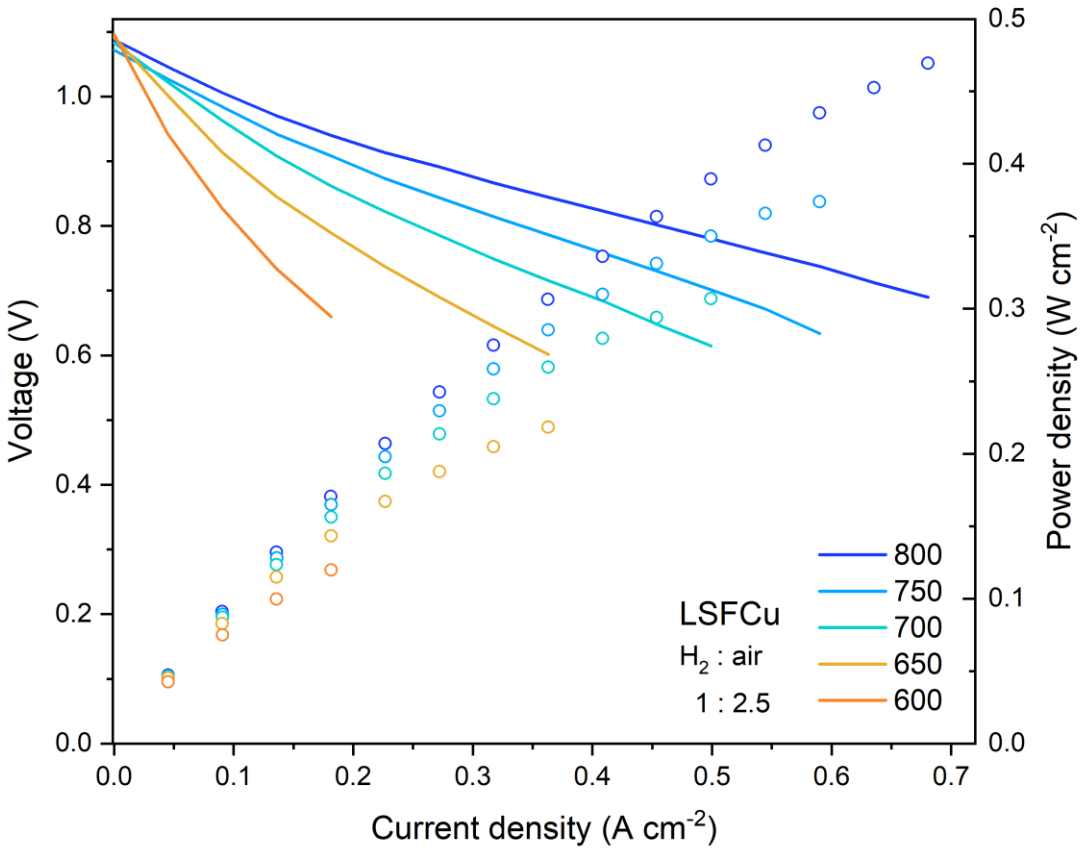

Figure 3.19. Polarisation (**line**) and power (**scatter**) curves for a full cell with LSFCu oxygen electrode in the 600-800 ºC temperature range.

A new set of measurements on SOFC mode was hence performed on a duplicate of the previous cell. This time, the temperature was set at 800 ºC and different H_2:air ratios and flows were tested. Moreover, impedance spectra data was collected on OCV conditions to observe the effect of the pO_2 variation on the performance of the cell. The results are shown in Figures 3.20 (a) and (b).

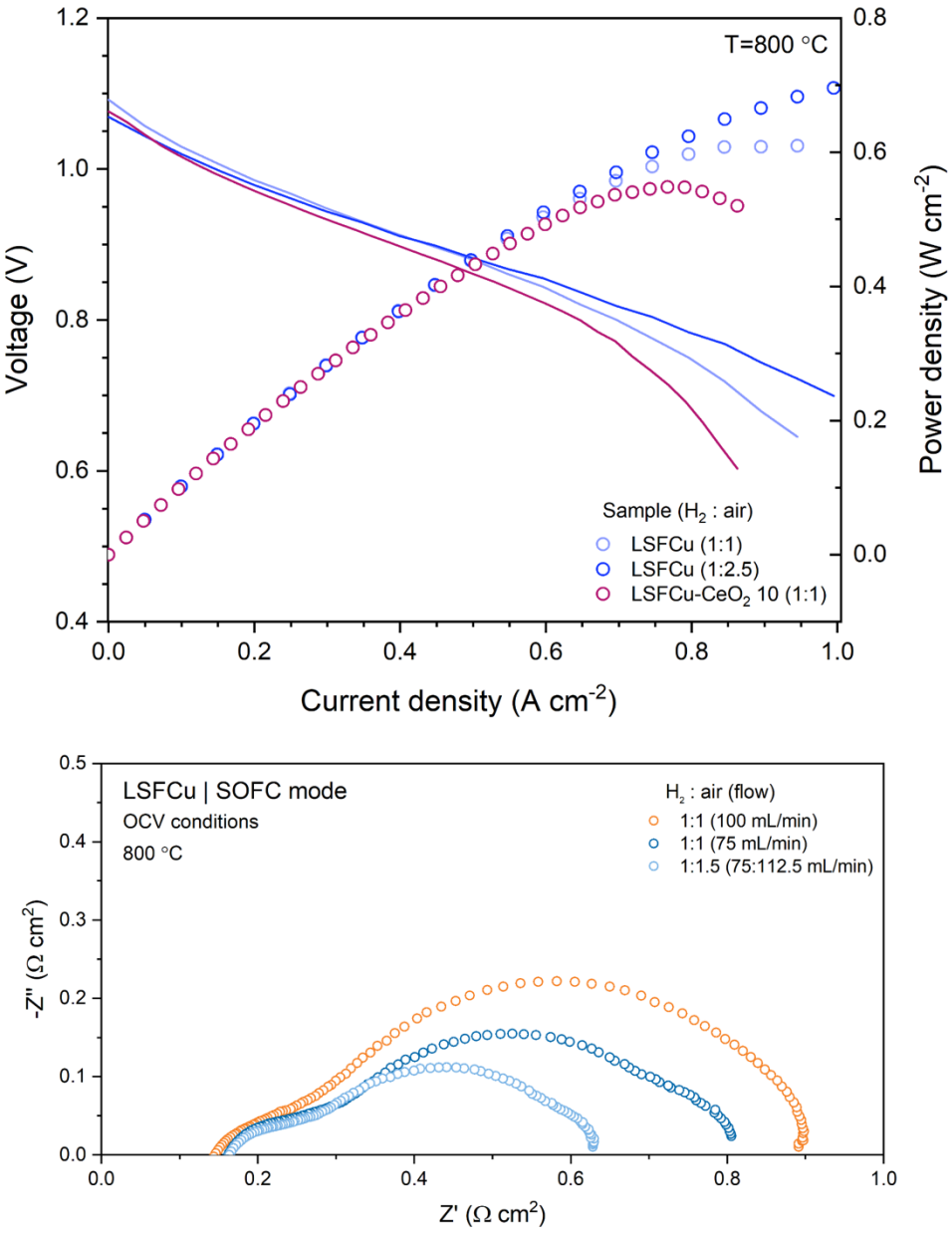

Figure 3.20. (**a**) I-V (**line**) and power (**scatter**) curves for the new full cell with LSFCu (two different flow ratios) and the LSFCu-CeO_2 10% oxygen electrodes at 800 ºC and (**b**) EIS spectra for the LSFCu sample showing the response of the device when subjected to different H_2 and air pressures.

In this case, the OCV value did not change with respect to the one obtained for the previous cell and is acceptable for testing. Neither activation nor polarisation significant

losses can be perceived in the 1:2.5 ratio I-V curve, nonetheless, the 1:1 ratio curve shows increased diffusion losses (at higher current densities). The power density curves in Figure 3.20a depicts a clear improvement in the performance of the cell, reaching ~0.6 $W.cm^{-2}$ at 0.7 $A.cm^{-2}$ and ~0.7 $W.cm^{-2}$ when a current density of 1 $A.cm^{-2}$ is applied. These values are larger than the ones reported by Zhou et al. (~0.51 $W.cm^{-2}$ at 1 $A.cm^{-2}$, ~0.53 $W.cm^{-2}$ at 1.3 $A.cm^{-2}$) and comparable to other new materials [57,63,92,93]. It must be noted that higher currents could not be applied due to equipment limitations (PARSTAT analyser can only apply a current intensity of 2A), which makes it impossible to confirm that the maximum power values were reached, especially when the voltage had not dropped below 0.6 V. This will be taken into account on future measurements.

Figure 3.20a also shows the results in SOFC mode obtained for the LSFCu-CeO_2 10 composite using a 1:1 fuel:air ratio (higher quantities of air decreased significantly the OCV value). The maximum power reached was ~0.55 $W.cm^{-2}$ at 0.77 $A.cm^{-2}$. Furthermore, the I-V curve is similar to the one obtained for the LSFCu sample (with the same fuel:air ratio) but it presents higher diffusion losses, observed at higher current densities. These could be owed to a lower performance of the material, but also a shortage in the fuel supply. New measurements with higher flows of fuel and air should be performed to verify this hypothesis.

After the SOFC mode testing, a constant flow of water steam was injected into the fuel electrode side to evaluate the performance of the LSFCu and LSFCu-CeO_2 10 oxygen electrodes in SOEC mode (Figure 3.21 a and b, respectively). The gases used on both sides were a 60:40 H_2O:H_2 mixture (22.2 $mL/min/cm^2$ in total) at the fuel electrode side and air at the oxygen electrode side (ratio fuel:air 1:2.5 for LSFCu and 1:1 for LSFCu-CeO_2 10). In this case, the hydrogen is added to avoid the re-oxidation of the fuel electrode due to local water presence, ensuring a completely-reduced state during the measurements.

The OCV value of the LSFCu sample was recorded (~0.88 V) and SOEC polarisation curves were measured at 750 and 800 ºC to study the performance of the cell. As evidenced

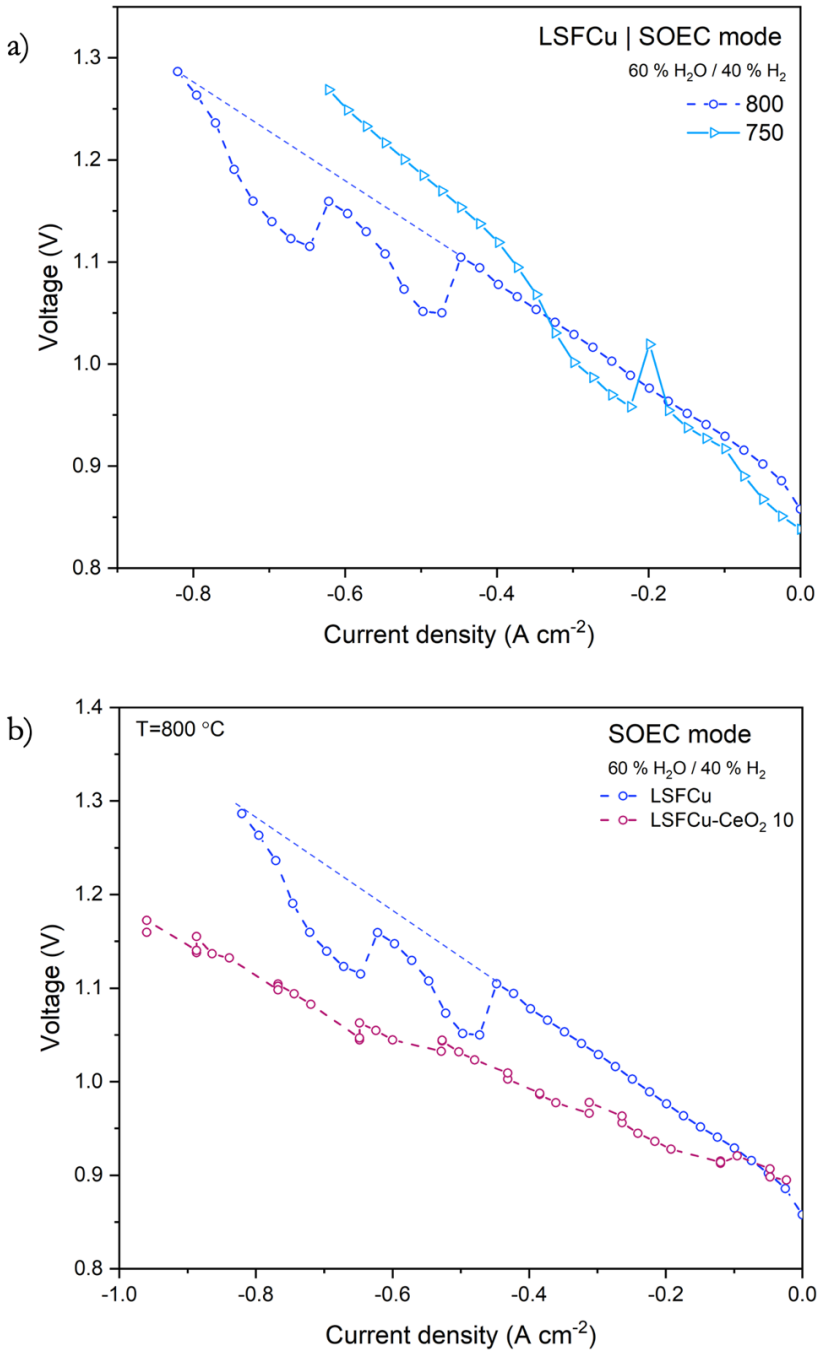

Figure 3.21. Polarisation curves in SOEC mode for the LSFCu oxygen-electrode full cell at two different temperatures (**a**) and LSFCu and the composite sample (**b**).

in the results, shown in Figure 3.21a, there is a voltage fluctuation in some areas of the curves (evident for the 800 ºC measurement, a dashed line was added for clarity); this can be attributed to a variation in the water steam flow and/or loss of some thermal isolation in the water supply entrance. Notwithstanding, the overall performance of the cell in SOEC mode is good, exhibiting values of 0.62 A.cm^{-2} at 1.27 V (750 ºC) and 0.82 A.cm^{-2} at 1.29 V (800 ºC), which indicates that the performance at 800 ºC is slightly better.

Regarding the LSFCu-CeO_2 10 composite sample, the OCV value recorded was ~0.91 V, and a single measurement at 800 ºC was performed due to problems with the sealing. Figure 3.21b shows the polarisation curves in SOEC mode for the two samples at 800 ºC. The composite outperforms the LSFCu sample in SOEC mode, exhibiting a current density value of 0.96 A.cm^{-2} at 1.17 V.

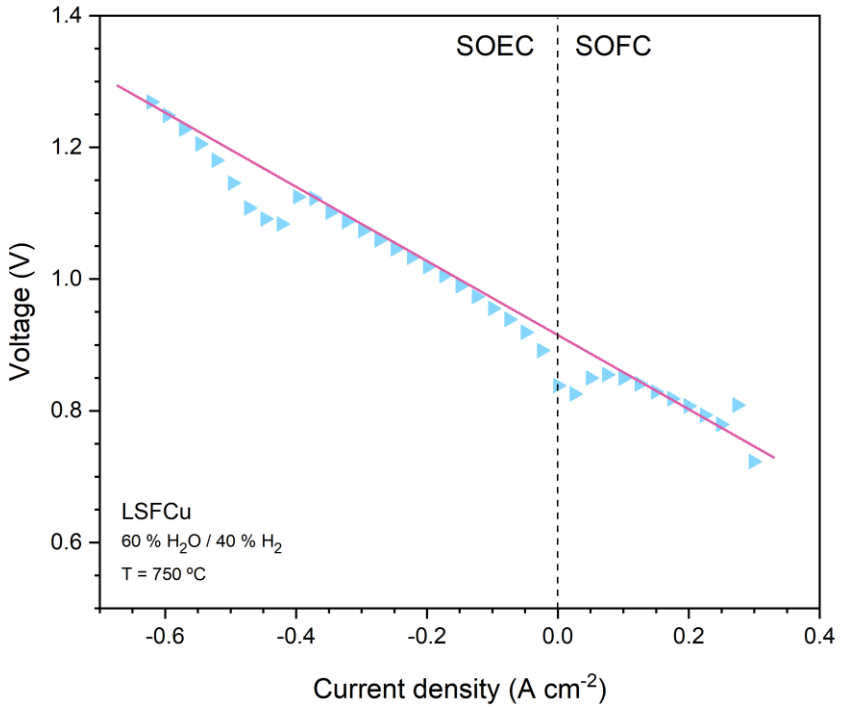

Figure 3.22. Polarisation curves in both SOFC and SOEC modes (reversible conditions) for the LSFCu oxygen-electrode full cell at 750 ºC.

SOFC/SOEC polarisation measurements on reversible conditions were also carried out at 750 ºC, using the same flows and ratios of the previous SOEC test; the results are shown in Figure 3.22 (the pink line in the curve is not a linear fit but a guide to the eye). It is worth noting that the smooth transition around OCV in the I-V curve indicates that SOCs with LSFCu oxygen electrode have favourable reversibility.

Overall, it can be said that the LSFCu oxygen electrode demonstrated an excellent performance in both SOFC and SOEC modes which is comparable to state-of-the-art materials. Further studies will be required to examine the other prepared electrodes.

Moreover, when thinking about full devices operating in long-term applications, not only the electrochemical performance of the oxygen electrode but other several aspects should be considered. The mechanical compatibility among the different cell components (including interconnects, seals, end plates, and other stack components that were out of the scope of this thesis), the chemical reactivity in the long-term and the performance during cycling, among others, should be studied in detail and optimised to ensure the most efficiently operating device.

Chapter 4

-CONCLUSIONS AND FUTURE WORK-

4. CONCLUSIONS AND FUTURE WORK

4.1. Conclusions

The present thesis was devoted to the development of new ion-conducting ceramics for their use as oxygen electrodes in reversible solid oxide cells (rSOC) for SOFC/SOEC applications.

In the first place, the results of the implementation of a novel two-step synthesis method for the preparation of LSFCu-CeO_2 composites were presented. This route proved to be an effective and rapid way to obtain cobalt-free, micro and nanostructured composites in the grams scale for SOC applications.

Secondly, the good performance of the LSFCu, LSFCu-CeO_2 10 and LSFCu-CeO_2 20 samples towards the oxygen reduction reaction (the ASR_{pol} at 800 ºC are ≈0.084 $\Omega.cm^2$, ≈0.11 $\Omega.cm^2$ and ≈0.18 $\Omega.cm^2$, respectively) was demonstrated, being the LSFCu the best-performing material of the series and comparable to state-of-the-art oxygen electrodes. Notwithstanding, the performances of the composites are also comparable to the ones reported in the literature, and the similar mechanical properties they exhibit regarding the electrolyte might significantly enhance the performance of the full devices.

In the third place, the construction of a complete SOC device using commercial fuel electrode-supported half-cells (NiO-YSZ fuel electrode + YSZ electrolyte) and the synthesised LSFCu and LSFCu-CeO_2 10% oxygen electrodes was accomplished, and the cells were tested as reversible SOFC/SOEC devices.

The LSFCu sample exhibited good performance in SOFC mode at 800 ºC, showing a power density of ~0.7 $W.cm^{-2}$ at 1 $A.cm^{-2}$, outperforming the same electrode material obtained and studied by other authors and presenting a comparable value to those reported in the literature for Co-free and Cu-containing electrodes. Moreover, the material was tested for the first time -to the best of our knowledge- in SOEC mode exhibiting a current density of ~0.82 $A.cm^{-2}$ at 1.29 V at 800 ºC and also in reversible conditions, demonstrating the potential for its application in reversible SOC devices.

The LSFCu-CeO_2 10% sample showed a regular performance in SOFC mode (~0.55 $W.cm^{-2}$ at 0.77 $A.cm^{-2}$) but really interesting results in SOEC mode, presenting a current density of ~0.96 $A.cm^{-2}$ at 1.17 V at 800 ºC. This might indicate that small percentages of La-doped CeO_2 can improve the behaviour of the materials in the electrolysis mode.

Lastly, it is worth mentioning that the contents shown in this thesis are the first full-device characterisation results of a SOEC obtained for a material prepared in our group.

4.2. Future work

Time and materials constraints prevented the testing of the LSFCu-CeO_2 5 and 50 % composite samples in symmetrical cells (activity towards the ORR) and the full-cell electrochemical characterisation (material performance as oxygen electrode of a reversible solid oxide cell) of the 5, 20 and 50 % in ceria LSFCu-CeO_2 composites.

Deeper crystallographic studies and other studies like mechanical compatibility (thermal expansion coefficients) and microstructural ones should be carried out to fully characterise the La-doping of CeO_2. This will help us delve deeper into the possible beneficial effects of

the ceria (or La-doped ceria) on the activity of the LSFCu-CeO_2 composites as oxygen electrodes in both SOFC and SOEC modes.

Moreover, other electrochemical measurements are needed to verify the potential long-term application of the prepared materials as oxygen electrodes and the long-term stability of the prepared cell working in an alternating reversible SOC device.

This work is already ongoing and the results of the characterisation of the full series will be submitted for publication in the near future.

References

[1] J. Kim, A. Jun, O. Gwon, S. Yoo, M. Liu, J. Shin, T.H. Lim, G. Kim, Hybrid-solid oxide electrolysis cell: A new strategy for efficient hydrogen production, Nano Energy. 44 (2018) 121–126. https://doi.org/10.1016/j.nanoen.2017.11.074.

[2] J. Kim, S. Sengodan, S. Kim, O. Kwon, Y. Bu, G. Kim, Proton conducting oxides: A review of materials and applications for renewable energy conversion and storage, Renew. Sustain. Energy Rev. 109 (2019) 606–618. https://doi.org/10.1016/j.rser.2019.04.042.

[3] H.J. Men, N. Tian, Y.M. Qu, M. Wang, S. Zhao, J. Yu, Improved performance of a lanthanum strontium manganite–based oxygen electrode for an intermediate-temperature solid oxide electrolysis cell realized via ionic conduction enhancement, Ceram. Int. 45 (2019) 7945–7949. https://doi.org/10.1016/j.ceramint.2019.01.107.

[4] M. Li, B. Hua, J. Chen, Y. Zhong, J.L. Luo, Charge transfer dynamics in RuO2/perovskite nanohybrid for enhanced electrocatalysis in solid oxide electrolyzers, Nano Energy. 57 (2019) 186–194. https://doi.org/10.1016/j.nanoen.2018.12.048.

[5] Y. Tian, N. Abhishek, C. Yang, R. Yang, S. Choi, B. Chi, J. Pu, Y. Ling, J.T.S. Irvine, G. Kim, Progress and potential for symmetrical solid oxide electrolysis cells, Matter. 5 (2022) 482–514. https://doi.org/10.1016/j.matt.2021.11.013.

[6] R. Vinoth Kumar, A.P. Khandale, A review on recent progress and selection of cobalt-based cathode materials for low temperature-solid oxide fuel cells, Renew. Sustain. Energy Rev. 156 (2022) 111985. https://doi.org/10.1016/j.rser.2021.111985.

[7] A. Vieira da Rosa, Fundamentals of Renewable Energy Processes, Third, Academic Press, 2012.

[8] Presente y futuro de las energías renovables en Uruguay, (2019) Oficina de Planeamiento y Presupuesto, Presidencia. https://www.opp.gub.uy/sites/default/files/inline-files/12_ Presente y futuro de las Energías Renovables en Uruguay.pdf.

[9] E. y M. Ministerio de Industria, Green Hydrogen Roadmap in Uruguay, Green

Hydrog. Roadmap Uruguay. (2022). https://www.gub.uy/ministerio-industria-energia-mineria/green-hydrogen.

[10] Breakdown of renewables in the energy mix- Our World in Data, (2022) BP Statistical Review of World Energy. https://ourworldindata.org/renewable-energy (accessed October 14, 2022).

[11] H. Ritchie, M. Roser, P. Rosado, Energy, Online Resour. (2020). https://ourworldindata.org/energy (accessed October 14, 2022).

[12] V. Venkataraman, M. Pérez-Fortes, L. Wang, Y.S. Hajimolana, C. Boigues-Muñoz, A. Agostini, S.J. McPhail, F. Maréchal, J. Van Herle, P. V. Aravind, Reversible solid oxide systems for energy and chemical applications – Review & perspectives, J. Energy Storage. 24 (2019). https://doi.org/10.1016/j.est.2019.100782.

[13] S.Y. Gómez, D. Hotza, Current developments in reversible solid oxide fuel cells, Renew. Sustain. Energy Rev. 61 (2016) 155–174. https://doi.org/10.1016/j.rser.2016.03.005.

[14] A. Perna, M. Minutillo, E. Jannelli, Designing and analyzing an electric energy storage system based on reversible solid oxide cells, Renew. Sustain. Energy Rev. 61 (2016) 155–174. https://doi.org/10.1016/j.rser.2016.03.005.

[15] LARED21, Experto internacional dijo que Uruguay está pronto para desarrollar tecnología de hidrógeno, (2018). http://www.lr21.com.uy/comunidad/1384563-tecnologia-energia-hidrogeno %0D%0A-combustible%0D%0A (accessed September 12, 2022).

[16] A. Niemczyk, K. Świerczek, Development of novel air electrode materials for the SOFC and SOEC technologies, E3S Web Conf. 108 (2019). https://doi.org/10.1051/e3sconf/201910801019.

[17] G. Jiang, H. Yu, J. Hao, J. Chi, Z. Fan, D. Yao, B. Qin, Z. Shao, An effective oxygen electrode based on Ir0.6Sn0.4O2 for PEM water electrolyzers, J. Energy Chem. 39 (2019) 23–28. https://doi.org/10.1016/j.jechem.2019.01.011.

[18] N. Wang, C. Tang, L. Du, Z.Q. Liu, W. Li, Z. Song, Y. Aoki, S. Ye, Single-phase La0.8Sr0.2Co1-xMnxO3-δ electrocatalyst as a triple H+/O2-/e- conductor enabling high-performance intermediate-temperature water electrolysis, J. Mater. (2022) 1–11. https://doi.org/10.1016/j.jmat.2022.02.012.

[19] Y. Choi, S. Byun, D.W. Seo, H.J. Hwang, T.W. Kim, S.D. Kim, New design and performance evaluation of 1 kW-class reversible solid oxide electrolysis-fuel cell stack using flat-tubular cells, J. Power Sources. 542 (2022) 231744. https://doi.org/10.1016/j.jpowsour.2022.231744.

[20] PTI-Mobility, PTI Mobility 2030, (2020). https://pti-mobility2030.csic.es/icp/ (accessed September 12, 2022).

[21] K. Shimura, H. Nishino, K. Kakinuma, M.E. Brito, H. Uchida, Effect of samaria-doped ceria (SDC) interlayer on the performance of La0.6Sr0.4Co0.2Fe0.8O3-δ/SDC composite oxygen electrode for reversible solid oxide fuel cells, Electrochim. Acta. 225 (2017) 114–120. https://doi.org/10.1016/j.electacta.2016.12.100.

[22] L. Bi, S. Boulfrad, E. Traversa, Reversible solid oxide fuel cells (R-SOFCs) with chemically stable proton-conducting oxides, Solid State Ionics. 275 (2015) 101–105. https://doi.org/10.1016/j.ssi.2015.03.006.

[23] M.B. Mogensen, M. Chen, H.L. Frandsen, C. Graves, J.B. Hansen, K. V. Hansen, A. Hauch, T. Jacobsen, S.H. Jensen, T.L. Skafte, X. Sun, Reversible solid-oxide cells for clean and sustainable energy, Clean Energy. 3 (2019) 175–201. https://doi.org/10.1093/ce/zkz023.

[24] J.T.S. Irvine, D. Neagu, M.C. Verbraeken, C. Chatzichristodoulou, C. Graves, M.B. Mogensen, Evolution of the electrochemical interface in high-temperature fuel cells and electrolysers, Nat. Energy. 1 (2016). https://doi.org/10.1038/nenergy.2015.14.

[25] A.L. Dicks, D.A.J. Rand, Fuel cell systems explained, Third, Wiley, Glasgow, 2018.

[26] J. Kunze-Liebhäuser, O. Paschos, S.S. Pethaiah, U. Stimming, Fuel Cell Comparison to Alternate Technologies, 2019. https://doi.org/10.1007/978-1-4939-7789-5_157.

[27] J.H. Zhu, D.A. Chesson, Y.T. Yu, Review—(Mn,Co) 3 O 4 -Based Spinels for SOFC Interconnect Coating Application , J. Electrochem. Soc. 168 (2021) 114519. https://doi.org/10.1149/1945-7111/ac3a29.

[28] B. Zhu, R. Raza, L. Fan, C. Sun, eds., Solid Oxide Fuel Cells: from Electrolyte-based to Electrolyte Free devices, First, Wiley-VCH, Weinheim, Germany, 2020.

[29] J.H. Zhang, F.Z. Han, C.X. Li, S.L. Zhang, A-site deficient Sr0.9Ti0.3Fe0.7O3−δ perovskite：A high stable cobalt-free oxygen electrode material for solid oxide electrochemical cells with excellent electrocatalytic activity and CO2 tolerance, J. Eur.

Ceram. Soc. 42 (2022) 5801–5812. https://doi.org/10.1016/j.jeurceramsoc.2022.06.047.

[30] L. Bernadet, G. Gousseau, A. Chatroux, J. Laurencin, F. Mauvy, M. Reytier, Influence of pressure on solid oxide electrolysis cells investigated by experimental and modeling approach, Int. J. Hydrogen Energy. 40 (2015) 12918–12928. https://doi.org/10.1016/j.ijhydene.2015.07.099.

[31] L. Bernadet, C. Moncasi, M. Torrell, A. Tarancón, High-performing electrolyte-supported symmetrical solid oxide electrolysis cells operating under steam electrolysis and co-electrolysis modes, Int. J. Hydrogen Energy. 45 (2020) 14208–14217. https://doi.org/10.1016/j.ijhydene.2020.03.144.

[32] R. O'Hayre, S.-W. Cha, W.G. Colella, F.B. Prinz, Fuel cell fundamentals, Third, John Wiley & Sons, Inc., Hoboken, NJ, USA, 2016.

[33] A. Leonide, SOFC Modelling and Parameter Identification by means of Impedance Spectroscopy, 2010.

[34] E.M. Hernández Rodríguez, Solid Oxide Electrolysis Cells electrodes based on mesoporous materials, Universidad de Barcelona, 2018.

[35] S. Anelli, Advanced strategies for Solid Oxide Electrolysis cells, Universidad Autónoma de Barcelona, 2021. https://widgets.ebscohost.com/prod/customerspecific/ns000545/customproxy.php?url=https://search.ebscohost.com/login.aspx?direct=true&db=edstdx&AN=edstdx.10803.671683&amp%0Alang=pt-pt&site=eds-live&scope=site.

[36] A. Leonide, Y. Apel, E. Ivers-Tiffee, SOFC Modeling and Parameter Identification by Means of Impedance Spectroscopy, 19 (2009) 81–109. https://doi.org/10.1149/1.3247567.

[37] E. Barsoukov, J.R. Macdonald, eds., Impedance Spectroscopy: Theory, Experiment and Applications, Third, John Wiley & Sons, Inc., Hoboken, NJ, USA, 2016.

[38] A. Nechache, M. Cassir, A. Ringuedé, Solid oxide electrolysis cell analysis by means of electrochemical impedance spectroscopy: A review, J. Power Sources. 258 (2014) 164–181. https://doi.org/10.1016/j.jpowsour.2014.01.110.

[39] W. Choi, H.C. Shin, J. Kim, J.Y. Choi, W.S. Yoon, Modeling and Applications of Electrochemical Impedance Spectroscopy (EIS) for Lithium-ion Batteries Woosung,

J. Electrochem. Sci. Technol. 11 (2020) 1–13. https://doi.org/10.33961/jecst.2019.00528.

[40] A. Leonide, V. Sonn, A. Weber, E. Ivers-Tiffée, Evaluation and Modeling of the Cell Resistance in Anode-Supported Solid Oxide Fuel Cells, J. Electrochem. Soc. 155 (2008) B36. https://doi.org/10.1149/1.2801372.

[41] K.C. Wincewicz, J.S. Cooper, Taxonomies of SOFC material and manufacturing alternatives, J. Power Sources. 140 (2005) 280–296. https://doi.org/10.1016/j.jpowsour.2004.08.032.

[42] P. Arunkumar, M. Meena, K.S. Babu, A review on cerium oxide-based electrolytes for ITSOFC, Nanomater. Energy. 1 (2012) 288–305. https://doi.org/10.1680/nme.12.00015.

[43] C. Neofytidis, E. Ioannidou, L. Sygellou, M. Kollia, D.K. Niakolas, Affecting the H2O electrolysis process in SOECs through modification of NiO/GDC; experimental case of Au-Mo-Ni synergy, J. Catal. 373 (2019) 260–275. https://doi.org/10.1016/j.jcat.2019.04.002.

[44] P. Kazempoor, R.J. Braun, Model validation and performance analysis of regenerative solid oxide cells: Electrolytic operation, Int. J. Hydrogen Energy. 39 (2014) 2669–2684. https://doi.org/10.1016/j.ijhydene.2013.12.010.

[45] M.A. Laguna-Bercero, Recent advances in high temperature electrolysis using solid oxide fuel cells: A review, J. Power Sources. 203 (2012) 4–16. https://doi.org/10.1016/j.jpowsour.2011.12.019.

[46] G. Kaur, A.P. Kulkarni, S. Giddey, CO2 reduction in a solid oxide electrolysis cell with a ceramic composite cathode: Effect of load and thermal cycling, Int. J. Hydrogen Energy. (2018) 21769–21776. https://doi.org/10.1016/j.ijhydene.2018.10.014.

[47] M. Kaur, K. Pal, Review on hydrogen storage materials and methods from an electrochemical viewpoint, J. Energy Storage. 23 (2019) 234–249. https://doi.org/10.1016/j.est.2019.03.020.

[48] Y. Zheng, J. Wang, B. Yu, W. Zhang, J. Chen, J. Qiao, J. Zhang, A review of high temperature co-electrolysis of H2O and CO2 to produce sustainable fuels using solid oxide electrolysis cells (SOECs): Advanced materials and technology, Chem. Soc. Rev. 46 (2017) 1427–1463. https://doi.org/10.1039/c6cs00403b.

[49] D. Xie, K. Li, J. Yang, D. Yan, L. Jia, B. Chi, J. Pu, J. Li, High-performance La0.5(Ba0.75Ca0.25)0.5Co0.8Fe0.2O3-δ cathode for proton-conducting solid oxide fuel cells, Int. J. Hydrogen Energy. 46 (2021) 10007–10014. https://doi.org/10.1016/j.ijhydene.2020.01.014.

[50] R.H. Mitchell, Perovskites: modern and ancient, Almaz Press Inc., Ontario, 2002.

[51] J.T.S. Irvine, P. Connor, Solid oxide fuels cells: Facts and figures: Past, present and future perspectives for SOFC Technologies, 2013. https://doi.org/10.1007/978-1-4471-4456-4.

[52] Z. Gao, L. V. Mogni, E.C. Miller, J.G. Railsback, S.A. Barnett, A perspective on low-temperature solid oxide fuel cells, Energy Environ. Sci. 9 (2016) 1602–1644. https://doi.org/10.1039/c5ee03858h.

[53] N. Di Benedetto, C. De los Santos, M. Del Pilar Yeste, J. Morais, M. Do Carmo Martins Alves, A. Amaya, L. Suescun, J.M. Gatica, H. Vidal, J. Castiglioni, Influence of the Thermal Processing and Doping on LaMnO3 and La0.8A0.2MnO3 (A = Ca, Sr, Ba) Perovskites Prepared by Auto-Combustion for Removal of VOCs, Catalysts. 12 (2022) 865. https://doi.org/10.3390/catal12080865.

[54] Q. Zeng, X. Liu, D. Xie, J. Ni, C. Ni, A strontium-free and iron-based oxygen electrode for solid-oxide electrochemical cells (SOCs), Int. J. Hydrogen Energy. 44 (2019) 15387–15399. https://doi.org/10.1016/j.ijhydene.2019.04.061.

[55] C. Berger, E. Bucher, C. Gspan, W. Sitte, Crystal structure, oxygen nonstoichiometry, and mass and charge transport properties of the Sr-free SOFC/SOEC air electrode material La 0.75 Ca 0.25 FeO 3-δ, J. Solid State Chem. 273 (2019) 92–100. https://doi.org/10.1016/j.jssc.2019.02.032.

[56] F. Zurlo, A. Iannaci, V.M. Sglavo, E. Di Bartolomeo, Copper-based electrodes for IT-SOFC, J. Eur. Ceram. Soc. 39 (2019) 17–20. https://doi.org/10.1016/j.jeurceramsoc.2018.02.029.

[57] K. Li, A. Niemczyk, K. Świerczek, A. Stępień, Y. Naumovich, J. Dąbrowa, M. Zajusz, K. Zheng, B. Dabrowski, Co-free triple perovskite La1.5Ba1.5Cu3O7±δ as a promising air electrode material for solid oxide fuel cells, J. Power Sources. 532 (2022) 1–11. https://doi.org/10.1016/j.jpowsour.2022.231371.

[58] M.A. Macias, M. V. Sandoval, N.G. Martinez, S. Vázquez-Cuadriello, L. Suescun, P.

Roussel, K. Świerczek, G.H. Gauthier, Synthesis and preliminary study of La4BaCu5O13 + δ and La6.4Sr1.6Cu8O20 ± δ ordered perovskites as SOFC/PCFC electrode materials, Solid State Ionics. 288 (2016) 68–75. https://doi.org/10.1016/j.ssi.2016.02.010.

[59] S. Duran, J. Tellez, M. V. Sandoval, M.A. Macias, E. Capoen, C. Pirovano, P. Roussel, A. Niemczyk, M. Barrera Castillo, L. Mogni, L. Suescun, G.H. Gauthier, Study of La4BaCu5−xCoxO13+δ series as potential cathode materials for intermediate-temperature solid oxide fuel cell, Solid State Ionics. 326 (2018) 116–123. https://doi.org/10.1016/j.ssi.2018.10.001.

[60] S. Durán, N. Rangel, C. Silva, M.A. Macias, E. Capoen, C. Pirovano, A. Niemczyk, L. Suescun, P. Roussel, G.H. Gauthier, Study of La4BaCu5-xMnxO13+δ materials as potential electrode for symmetrical-SOFC, Solid State Ionics. 341 (2019) 115031. https://doi.org/10.1016/j.ssi.2019.115031.

[61] S. Vázquez, L. Suescun, R. Faccio, Effect of Cu doping on Ba 0.5 Sr 0.5 Fe 1-x Cu x O 3-d perovskites for solid oxide fuel cells : A first-principles study, J. Power Sources. 311 (2016) 13–20. https://doi.org/10.1016/j.jpowsour.2016.02.028.

[62] S. Vázquez, S. Davyt, J.F. Basbus, A.L. Soldati, A. Amaya, A. Serquis, R. Faccio, L. Suescun, Synthesis and characterization of La0.6Sr0.4Fe0.8Cu0.2O3-δ oxide as cathode for Intermediate Temperature Solid Oxide Fuel Cells, J. Solid State Chem. 228 (2015) 208–213. https://doi.org/10.1016/j.jssc.2015.04.044.

[63] Q. Zhou, L. Xu, Y. Guo, D. Jia, Y. Li, W.C.J. Wei, La 0.6Sr 0.4Fe 0.8Cu 0.2O 3-δ perovskite oxide as cathode for IT-SOFC, Int. J. Hydrogen Energy. 37 (2012) 11963–11968. https://doi.org/10.1016/j.ijhydene.2012.05.114.

[64] J. Ascolani-Yael, A. Montenegro-Hernández, H. Troiani, L. Mogni, A. Caneiro, Study of the Rate Limiting Steps and Degradation of a GDC Impregnated La0.6Sr0.4Co0.8Fe0.2O3-δ Cathode J., ECS Trans. 78 (2017) 795–805.

[65] W. Zajac, L. Suescun, K. Świerczek, J. Molenda, Structural and electrical properties of grain boundaries in Ce0.85Gd0.15O1.925 solid electrolyte modified by addition of transition metal ions, J. Power Sources. 194 (2009) 2–9. https://doi.org/10.1016/j.jpowsour.2008.12.020.

[66] M. Reisert, A. Aphale, P. Singh, Solid oxide electrochemical systems: Material

degradation processes and novel mitigation approaches, Materials (Basel). 11 (2018). https://doi.org/10.3390/ma11112169.

[67] X. Yang, J. Chen, D. Panthi, B. Niu, L. Lei, Z. Yuan, Y. Du, Y. Li, F. Chen, T. He, Electron doping of Sr 2 FeMoO 6-: δ as high performance anode materials for solid oxide fuel cells, J. Mater. Chem. A. 7 (2019) 733–743. https://doi.org/10.1039/c8ta10061f.

[68] T. Fukumoto, N. Endo, K. Natsukoshi, Y. Tachikawa, G.F. Harrington, S.M. Lyth, J. Matsuda, K. Sasaki, Exchange current density of reversible solid oxide cell electrodes, Int. J. Hydrogen Energy. 47 (2022) 16626–16639. https://doi.org/10.1016/j.ijhydene.2022.03.164.

[69] P. Willmott, An Introduction to Synchrotron Radiation: Techniques and Applications, Second, John Wiley & Sons, Inc., Chichester, UK, 2019.

[70] B.D. Fahlman, Materials chemistry, Third, Springer Nature B.V., 2018. https://doi.org/10.1007/978-1-4020-6120-2.

[71] H.M. Rietveld, A profile refinement method for nuclear and magnetic structures, J. Appl. Crystallogr. 2 (1969) 65–71. https://doi.org/10.1107/s0021889869006558.

[72] Scanning electron microscopy (SEM), what is it for?, Atria Innov. (n.d.). https://www.atriainnovation.com/en/scanning-electron-microscopy-uses/ (accessed September 10, 2022).

[73] How Scanning Electron Microscopes Work, Azo Mater. (n.d.). https://www.azom.com/article.aspx?ArticleID=14791 (accessed September 10, 2022).

[74] SEM Technology Overview – Scanning Electron Microscopy, Nanoimages. (n.d.). https://www.nanoimages.com/sem-technology-overview/ (accessed September 10, 2022).

[75] H. Wang, M. Zhou, P. Choudhury, H. Luo, Perovskite oxides as bifunctional oxygen electrocatalysts for oxygen evolution/reduction reactions – A mini review, Appl. Mater. Today. 16 (2019) 56–71. https://doi.org/10.1016/j.apmt.2019.05.004.

[76] J. Grassi, M.A. Macias, J. Castiglioni, J.F. Basbus, G.H. Gauthier, A. Serquis, L. Suescun, Synthesis and Characterization of High Temperature Properties of YBa2Cu3O6+δ Superconductor as Potential Cathode for Intermediate Temperature

Solid Oxide Fuel Cells, J. Mater. Sci. Technol. Res. 8 (2021) 81–92. https://doi.org/10.15377/2410-4701.2021.08.10.

[77] M.P. Pechini, Method of Preparing Lead and Alkaline Earth Titanates and Niobates and Coating Method using the same to form a Capacitor, 1967.

[78] L. Bernadet, F. Baiutti, F. Martinelli, M. Torrell, A. Morata, D. Montinaro, A. Tarancón, Thin Film Barrier Layers with Increased Performance and Reduced Long-Term Degradation in SOFCs, ECS Meet. Abstr. MA2021-03 (2021) 80–80. https://doi.org/10.1149/ma2021-03180mtgabs.

[79] S. Anelli, L. Moreno-Sanabria, F. Baiutti, M. Torrell, A. Tarancón, Solid oxide cell electrode nanocomposites fabricated by inkjet printing infiltration of ceria scaffolds, Nanomaterials. 11 (2021). https://doi.org/10.3390/nano11123435.

[80] J. Laurencin, M. Hubert, D.F. Sanchez, S. Pylypko, M. Morales, A. Morata, B. Morel, D. Montinaro, F. Lefebvre-Joud, E. Siebert, Degradation mechanism of La0.6Sr0.4Co0.2Fe0.8O3-δ/Gd0.1Ce0.9O2-δ composite electrode operated under solid oxide electrolysis and fuel cell conditions, Electrochim. Acta. 241 (2017) 459–476. https://doi.org/10.1016/j.electacta.2017.05.011.

[81] Z. Pan, Q. Liu, Z. Yan, Z. Jiao, L. Bi, S.H. Chan, Z. Zhong, On the delamination of air electrodes of solid oxide electrolysis cells: A mini-review, Electrochem. Commun. 137 (2022) 107267. https://doi.org/10.1016/j.elecom.2022.107267.

[82] V. Miguel-Pérez, J.P. Ouweltjes, A. Tarancón, M. Torrell, V. Bongiorno, Z. Wuillemin, D. Montinaro, A. Morata, Degradation Studies and Sr Diffusion Behaviour in Anode Supported Cell after 3,000 h SOFC Short Stack Testing, ECS Meet. Abstr. MA2015-03 (2015) 24–24. https://doi.org/10.1149/ma2015-03/1/24.

[83] J. Matsuda, S. Kanae, T. Kawabata, J.-T. Chou, Y. Inoue, S. Taniguchi, K. Sasaki, TEM and ETEM Study on SrZrO 3 Formation at the LSCF/GDC/YSZ Interfaces , ECS Meet. Abstr. MA2017-03 (2017) 218–218. https://doi.org/10.1149/ma2017-03/1/218.

[84] S. Sameshima, M. Kawaminami, Y. Hirata, Thermal Expansion of Rare-Earth-Doped Ceria Ceramics, J. Ceram. Soc. Japan. 110 (2002) 597–600.

[85] T. Ishihara, J. Tabuchi, S. Ishikawa, J. Yan, M. Enoki, H. Matsumoto, Recent progress in LaGaO3 based solid electrolyte for intermediate temperature SOFCs, Solid State

Ionics. 177 (2006) 1949–1953. https://doi.org/10.1016/j.ssi.2006.01.044.

[86] D. Stöver, H.P. Buchkremer, S. Uhlenbruck, Processing and properties of the ceramic conductive multilayer device solid oxide fuel cell (SOFC), Ceram. Int. 30 (2004) 1107–1113. https://doi.org/10.1016/j.ceramint.2003.12.018.

[87] R. Eason, ed., Pulsed Layer Deposition of Thin Films, John Wiley & Sons, Inc., Hoboken, NJ, USA, 2006.

[88] ProboStat Specifications, NORECS AS. (n.d.). http://www.norecs.com/index.php?page=Brochures+and+leaflets (accessed September 10, 2022).

[89] B.H. Toby, R.B. Von Dreele, GSAS-II : the genesis of a modern open-source all purpose crystallography software package, Appl. Crystallogr. 46 (2013) 544–549. https://doi.org/10.1107/S0021889813003531.

[90] E. Suda, B. Pacaud, M. Mori, Sintering characteristics, electrical conductivity and thermal properties of La-doped ceria powders, J. Alloys Compd. 408–412 (2006) 1161–1164. https://doi.org/10.1016/j.jallcom.2004.12.135.

[91] S. Wang, T. Kobayashi, M. Dokiya, T. Hashimoto, Electrical and Ionic Conductivity of Gd-Doped Ceria, J. Electrochem. Soc. 147 (2000) 3606–3609. https://doi.org/10.1149/199919.0193pv.

[92] J. Li, N. Sun, X. Liu, Y. Shen, F. Wang, J. Li, K. Shi, F. Jin, Investigation on Nd1–xCaxBaCo2O5+δ double perovskite as new oxygen electrode materials for reversible solid oxide cells, J. Alloys Compd. 913 (2022) 165245. https://doi.org/10.1016/j.jallcom.2022.165245.

[93] Y. Tian, W. Wang, Y. Liu, L. Zhang, L. Jia, J. Yang, B. Chi, J. Pu, J. Li, Cobalt-Free Perovskite Oxide La0.6Sr0.4Fe0.8Ni0.2O3-Î as Active and Robust Oxygen Electrode for Reversible Solid Oxide Cells, ACS Appl. Energy Mater. 2 (2019) 3297–3305. https://doi.org/10.1021/acsaem.9b00115.